



HAL
open science

Analysis of turbulent transport in the central part of high-confinement tokamak plasmas

Neeraj Kumar

► **To cite this version:**

Neeraj Kumar. Analysis of turbulent transport in the central part of high-confinement tokamak plasmas. Plasma Physics [physics.plasm-ph]. Aix Marseille Université, 2021. English. NNT: . tel-03368780

HAL Id: tel-03368780

<https://amu.hal.science/tel-03368780v1>

Submitted on 7 Oct 2021

HAL is a multi-disciplinary open access archive for the deposit and dissemination of scientific research documents, whether they are published or not. The documents may come from teaching and research institutions in France or abroad, or from public or private research centers.

L'archive ouverte pluridisciplinaire **HAL**, est destinée au dépôt et à la diffusion de documents scientifiques de niveau recherche, publiés ou non, émanant des établissements d'enseignement et de recherche français ou étrangers, des laboratoires publics ou privés.

.....

THÈSE DE DOCTORAT

Soutenue à Aix-Marseille Université
le 02 février 2021 par

Neeraj KUMAR

ANALYSIS OF TURBULENT TRANSPORT IN THE CENTRAL PART OF HIGH-CONFINEMENT TOKAMAK PLASMAS

Discipline

Physique et Sciences de la Matière

Spécialité

Energie, Rayonnement et Plasma

École doctorale

ED 352

Laboratoire/Partenaires de recherche

Physique des Interactions Ioniques et Moléculaires (PIIM)—AMU—CNRS, UMR7345

IRFM - CEA Cadarache, Bât. 513, 13108 Saint-Paul-Lez-Durance, France

ITER Organization, Route de Vinon-sur-Verdon, 13067 St-Paul-Lez-Durance, France

Composition du jury

.....

Clemente ANGIONI Rapporteur
IPP-Garching

Paola MANTICA Rapporteur
CNR Milano

Jonathan CITRIN Examineur
DIFFER Eindhoven

Francis CASSON Examineur
UKAEA Oxfordshire

Alberto LOARTE Examineur
ITER Organization

Yann CAMENEN Examineur
CNRS, AMU

Clarisse BOURDELLE Co-Directeur de thèse
IRFM, CEA Cadarache

Sadruddin BENKADDA Directeur de thèse
CNRS, AMU

I, undersigned, Neeraj Kumar, hereby declare that the work presented in this manuscript is my own work, carried out under the scientific direction of Sadruddin Benkadda and Clarisse Bourdelle, in accordance with the principles of honesty, integrity and responsibility inherent to the research mission. The research work and the writing of this manuscript have been carried out in compliance with both the french national charter for Research Integrity and the Aix-Marseille University charter on the fight against plagiarism.

This work has not been submitted previously either in this country or in another country in the same or in a similar version to any other examination body.

Marseille, 07.12.2020

Neeraj



Cette œuvre est mise à disposition selon les termes de la [Licence Creative Commons Attribution - Pas d'Utilisation Commerciale - Pas de Modification 4.0 International](https://creativecommons.org/licenses/by-nc-nd/4.0/).

The present work has been carried out in collaboration with the doctoral school "École doctorale 352: Physique et Sciences de la Matière" at Aix-Marseille University and ITER Organization, France. Two thirds of this thesis were carried out at the PIIM laboratory (Physique des Interactions Ioniques et Moléculaires) and the remaining third was conducted at ITER Organization under the memorandum of understanding (LGA-2017-A-76). Disclaimer: ITER is the nuclear facility INB no. 174. The views and opinions expressed herein do not necessarily reflect those of the ITER Organization.

Résumé

Un des principaux objectifs du projet ITER est de démontrer qu'un tokamak peut générer une puissance de fusion supérieure à la puissance injectée. Dans ITER, les composants face au plasma sont métalliques (diverteur en tungstène, mur en béryllium) pour garantir une faible rétention du tritium et une haute résistance au flux d'énergie provenant du plasma. L'opération d'un tokamak en environnement métallique soulève cependant des difficultés. L'accumulation des impuretés lourdes telles que le tungstène ($Z=74$) dans le cœur du plasma provoque des pertes par rayonnement et une détérioration conséquente du confinement de l'énergie. Le transport du tungstène dans la partie centrale d'ITER est induit par les collisions (transport néoclassique) et la turbulence. Il dépend intrinsèquement des gradients de densité et de température des ions principaux. Une compréhension fine des mécanismes de transport actifs dans le centre du plasma est à cet égard cruciale pour pouvoir prédire précisément l'accumulation du tungstène. Les études précédentes se sont principalement focalisées sur la zone à mi-rayon et le bord du plasma ($\rho > 0.3$), la partie centrale restant, pour le moment, un territoire relativement inexploré.

Dans la région centrale, les gradients de température et densité sont plus faibles et la turbulence pourrait s'en trouver réduite. Une question clef est donc d'abord de savoir si le plasma est linéairement stable ou non dans cette région. Si oui, la diffusion turbulente est-elle suffisante pour compenser le terme de pincement néoclassique du W ? Jusqu'à quel rayon et avec quelle dépendance sur les gradients de température et densité ? Une autre question clef est de savoir si l'approximation quasi-linéaire est valide dans la région centrale et si des modèles réduits quasi-linéaires classiques tels que QuaLiKiz ou TGLF peuvent y être utilisés. La compréhension du transport turbulent dans la région centrale est critique pour prédire le piquage des profils au cœur du plasma qui, eux-mêmes, influencent les réactions de fusion et le transport néoclassique du W . L'objectif de cette thèse est d'étudier ces questions et de tester les modèles réduits disponibles dans la région centrale de tokamak existants avant de pouvoir les appliquer sur ITER. L'étude est focalisée sur des cas sans activité MHD significative. Bien entendu, cette dernière peut aussi affecter le comportement du plasma dans la région centrale dans certaines conditions.

Le transport turbulent dans la région centrale est exploré dans un plasma à haut β en mode H hybride du tokamak JET au moyen de simulations linéaires et non-linéaires effectuées avec le code gyrocinétique GKW dans la limite locale. Par rapport aux travaux précédents, l'analyse est étendue à la région $\rho < 0.3$ et révèle que les Kinetic Ballooning Modes (KBM) y sont linéairement instables, contrairement à

la région $\rho > 0.3$ où les modes Ion Temperature Gradient dominant. Des simulations spécifiques à $\rho = 0.15$ ont permis d'identifier le faible cisaillement magnétique et la haute pression normalisée du plasma, β , comme étant les deux principaux paramètres clés permettant la déstabilisation des KBM par le relativement faible gradient de pression des ions principaux. Les ions rapides ont un effet légèrement stabilisant lorsqu'ils sont inclus dans les simulations. L'étude est ensuite étendue au régime non-linéaire. La turbulence induite par les KBM génère un flux significatif d'énergie thermique ionique et électronique. De manière inattendue, des modes de micro-déchirement (MTM) linéairement stables sont excités non-linéairement et génèrent un flux non-négligeable d'énergie thermique électronique lié aux fluctuations du champ magnétique. Des modèles quasi-linéaires standards sont ensuite comparés aux résultats non-linéaires. Ces modèles reproduisent raisonnablement bien les flux $\mathbf{E} \times \mathbf{B}$, mais mésestiment le flux d'énergie thermique électronique résultant de l'excitation non-linéaire des MTMs. Une extension des modèles quasi-linéaire est proposée qui permet de mieux reproduire le flux d'énergie lié aux fluctuations du champ magnétique.

Keywords: plasma, fusion magnétique, transport de turbulence, quasi-linear, gyrokinetic, tokamak

Abstract

One of the major goals of the ITER project is to demonstrate high fusion power gain in a tokamak. In ITER, metallic plasma-facing components are chosen for their low tritium retention and ability to sustain high heat loads. However, tokamak operation with metallic plasma-facing components raises issues regarding the control of high-Z impurities since the accumulation of heavy impurities such as tungsten ($Z=74$) in the plasma core leads to significant radiation losses and deteriorates the energy confinement. Transport of tungsten (W) in the central part of ITER ($\rho < 0.3$), is expected to be determined by neoclassical and turbulent processes, which strongly depend on the main ion density, temperature, and rotation profiles. Thus, a reliable understanding of the dominant transport mechanisms in the central part is crucial to accurately predict W core accumulation. Previous studies mostly focused on the edge and core regions ($\rho > 0.3$) and the central part remains relatively unexplored so far.

In the central region, the gradients of density and temperature get smaller, and as a consequence, the level of turbulence may be reduced. In this region, a key question is therefore whether the plasma is linearly unstable. If yes, is turbulent diffusion sufficient to offset the neoclassical (inward) pinch of W, up to which radius and how sensitive is this to the background gradients? An auxiliary question is whether the quasi-linear approximation is valid in the inner core and up to which degree standard reduced quasi-linear models such as QuaLiKiz (QuasiLinear gyroKinetic) or TGLF (trapped gyro-Landau-fluid) can be used in the central zone. Understanding turbulent transport in the central region is crucial to predict core profile peaking that in turn will impact the fusion reactions and the tungsten neoclassical transport, in present devices as well as in ITER. The goal of this thesis is to address these questions and test the available turbulent transport models in the central region for existing tokamaks before applying them to evaluate turbulent transport in ITER. The study is focused on cases without MHD activity. Sawteeth, saturated kink modes or NTMs can also have a strong impact on the plasma behaviour in the central region and need to be considered in specific conditions.

Turbulent transport is investigated in the central region of the high- β JET hybrid H-mode discharge 75225 by means of linear and non-linear gyro-kinetic simulations using the gyro-kinetic code GKW in the local approximation limit. Compared to previous work, the analysis is extended towards the magnetic axis, $\rho < 0.3$, where the turbulence characteristics remain an open question. In contrast to the region $\rho > 0.3$ where Ion Temperature Gradient modes are the most unstable

modes, the linear stability analysis indicates that Kinetic Ballooning Modes (KBM) dominate in the central region. A dedicated analysis performed at $\rho = 0.15$ reveals that the main parameters responsible for the destabilisation of KBMs in these hybrid H-modes are the high β and low magnetic shear values. The KBMs are driven by the main ion pressure gradient with little influence of the electron temperature gradient. Including fast-ions as a kinetic species in the simulations has a slight stabilising effect. The study is then extended to the non-linear regime. It is found that the turbulence induced by these KBMs drives a significant ion and electron heat flux. Interestingly, linearly stable micro-tearing-modes (MTM) are excited non-linearly and drive a sizeable magnetic flutter electron heat flux. Standard quasi-linear models are compared to the non-linear results. The standard reduced quasi-linear models work reasonably well for the $\mathbf{E} \times \mathbf{B}$ fluxes, but fail to capture magnetic flutter contribution to the electron heat flux induced by the non-linear excitation of the MTMs. An extension of the quasi-linear models is proposed allowing better capturing the magnetic flutter flux.

Keywords: plasma, magnetic fusion, turbulence transport, quasi-linear, gyrokinetic, tokamak

Acknowledgement

First of all, I would like to thank all the people who helped me directly or indirectly and have been by my side during these three years of my PhD. I would like to express my deepest gratitude to all my thesis supervisors, Dr Yann Camenen, Dr Aberto Loarte, Dr Clarisse Bourdelle and Prof Sadruddin Benkadda. They have always supported me unconditionally over the past three years. I want to especially thank Dr Yann Camenen, who was so kind and supportive and always explained things with patience whenever I needed him. Further, I also like to acknowledge his unwavering support of the GKW code, which helped me to understand the code and get physically meaningful results. Similarly, Dr Alberto Loarte and Dr Clarisse Bourdelle have always found the time to assist and provide their valuable advice to me even in their busy schedule. Also, regular discussions and work follow up with them enhanced my knowledge and understanding of the various concepts involved in the thesis. I am also grateful to my thesis director Prof. Sadruddin Benkadda for providing his insights into the different physics aspects of the thesis work. All the administration work was smooth because of his support throughout the thesis. I consider myself so lucky to have all as my supervisors and deeply grateful for their advice and motivating scientific discussions.

My special thanks to Dr Clemente Angioni and Dr Paola Mantica for accepting the offer of being the reviewers of my manuscript. Detailed reports and suggestions from them have helped to enhance the quality of the manuscript. It also helped me think about some very important questions related to the work's theoretical and experimental aspects. My gratitude to Dr Jonathan Citrin and Dr Francis Casson for giving their time to read the manuscript and accepting the offer of being the jury members in PhD defense.

I would like to acknowledge the contributions of Dr Alexei Polevoi for his guidance on ASTRA code and for providing input plasma profiles from ASTRA simulations to perform simulations for ITER scenarios. I am also thankful to Aaron Ho for providing GPR fits. I am grateful to Dr Pierre Manas for performing neoclassical simulations. Many thanks to Dr Fabien Widmer, Dr David Zarzoso and Samuele Mazzi for useful work discussion and help. I am thankful to Dr M.J. Pueschel and Dr Xavier Garbet for fruitful discussions during article preparation. Thanks to Dr Simon Pinches in ITER for technical support whenever I needed it.

I am highly thankful to everyone in my research group DSC and TP, PIIM laboratory, the CEA, and the ITER science division for their useful advice and for providing me with a very conducive environment to work and progress in my thesis.

In the end, I am very grateful to my friends and colleagues Mun Jong Hern, Manuela Sisti, Myriam Hamed, Javier Artola, Sabine Nasr, Daniele Villa and many others that have always helped me during these challenging time and provided me with a pleasant company.

My Indian friends from the same University of Delhi have made this journey smooth and joyful by providing me with moral support and encouragement whenever I needed it. Thanks to Shambhavi Nandan, Vaishnavi Tiwari, Lokesh Verma, Savneet Kaur and Nitendra Singh.

Of course, this work was possible due to the administrative help that I got from different institutions. I would especially like to thank the doctoral school ED352 for their support, director of the PIIM laboratory Annette Calisti and secretary Eric Rostang, and the ITER secretaries and EUROfusion High-Performance Computer (Marconi-Fusion) EUROfusion, Centre de Calcul Intensif d'Aix-Marseille for granting access to its high-performance computing resources.

Finally, I am thankful to my family, especially my elder brother Pankaj Kumar, who always unconditionally helped my every decision. This journey could not have been possible without their moral support and encouragement throughout this PhD time.

Contents

Résumé	6
Abstract	7
Acknowledgement	9
List of Figures	15
List of Tables	21
Nomenclature	22
1 Introduction	25
1.1 Nuclear fusion as a potential energy source	25
1.2 Basis of thermonuclear Fusion	26
1.3 Plasma: the fourth state of matter	27
1.3.1 Reaction rate and fusion cross-section	27
1.3.2 Fusion reactions	28
1.3.3 Conditions for a fusion reaction: Lawson criteria	30
1.3.4 Brief historical review of nuclear fusion	31
1.4 Tokamaks and magnetic confinement	33
1.4.1 Introduction to tokamaks	33
1.4.2 Transport in plasma: constraint to tokamak performance . .	39
1.5 The choice of tungsten as a plasma-facing components	40
1.5.1 The W core accumulation issue: line radiation	41
1.5.2 Tungsten impurity transport	42
1.6 Thesis Motivation	44
1.7 Thesis Outline	44
2 Tokamak plasma instabilities	47
2.1 Overview of tokamak micro-turbulence	47
2.1.1 Particle motion and drift velocities in magnetised plasma . . .	47
2.1.2 Drift wave and interchange instability	49
2.1.3 Scale separation of instabilities	51
2.1.3.1 Kinetic ballooning modes (KBMs)	53
2.2 Models for tokamak micro-turbulence	55
2.3 Summary	57

3	Overview of the gyrokinetic code GKW	59
3.1	Gyrokinetic orderings	59
3.2	Gyrokinetic equation solved in GKW	60
3.3	Normalisations in GKW	63
3.4	Geometry	65
3.4.1	Miller parameterisation	65
3.5	Spectral representation in GKW	67
4	Linear stability analysis of a JET hybrid H-mode plasma	71
4.1	Input parameters of JET hybrid H-mode discharge 75225	71
4.1.1	Experimental profiles	71
4.1.2	Magnetic equilibrium reconstruction	74
4.1.3	Grid convergence	74
4.2	Linear unstable modes across the minor radius and impact of fast ions	77
4.3	Linear stability analysis at $\rho = 0.15$	82
4.3.1	Impact of magnetic shear and plasma beta	84
4.3.2	The role of the pressure gradient β'	86
4.3.3	Impact of T_e/T_i ratio and safety factor q	87
4.3.4	Additional parameter scans	88
4.3.5	Identification of unstable mode as KBM	90
4.4	Linear heat and particle fluxes at $\rho = 0.15$	91
4.5	Summary	92
5	Nonlinear gyrokinetic simulations and test of the quasi-linear approximation	95
5.1	Non-linear simulations at $\rho = 0.15$	95
5.2	Test of the quasilinear approximation in the inner core	100
5.2.1	Quasi-linear approximation	101
5.2.1.1	Mixing length model	101
5.2.1.2	QuaLiKiz model	102
5.2.2	Linear heat and particle fluxes	103
5.2.3	Comparison of nonlinear and quasi-linear spectra	103
5.2.4	Comparison of quasi-linear fluxes with non-linear simulations	104
5.2.4.1	Comparison of $\mathbf{E} \times \mathbf{B}$ fluxes	105
5.2.4.2	Comparison of magnetic flutter fluxes	107
5.3	Sensitivity of the quasilinear ion heat fluxes to input gradients	110
5.4	Summary	111
6	Conclusions and future perspective	113
	APPENDICES	116
A	Simplified dispersion relation for ITG instability	117
A.1	The δf gyrokinetic equation in the slab-like approximation	117
A.1.1	Reference gyro-kinetic equation	117
A.1.2	Coordinate system and magnetic geometry	118
A.1.3	Perturbed quantities and gyro-average	119

A.1.4	Linearized one-point gyro-kinetic equation	120
A.1.5	Quasi-neutrality and adiabatic electron approximation	121
A.1.6	Final set of equations	122
A.2	Fluid Model	122
A.2.1	Moments of distribution function	122
A.2.2	Toroidal ITG and SLAB ITG	125
A.2.2.1	Toroidal ITG	125
A.2.2.2	Slab ITG	128
A.3	Kinetic model	130
	Bibliography	133

List of Figures

1.1	Binding energy per nucleon versus mass number plots for various atomic elements. Fig. courtesy: Pearson Prentice Hall.	27
1.2	Reaction parameter $\langle\sigma v\rangle$ as a function of temperature. Courtesy [3].	28
1.3	Schematic of a D-T fusion reaction forming a helium nucleus.	29
1.4	Schematic diagram of JET (on left side) and ITER (on right side) tokamak. Source: https://www.iter.org/	32
1.5	Core ion temperature as a function of fusion triple product [10].	33
1.6	Illustration of a tokamak configuration (Courtesy: Eurofusion [11]).	34
1.7	Schematic of a circular concentric magnetic flux surfaces of a tokamak.	36
1.8	Schematic view of poloidal cross-section of a tokamak with limiter and divertor geometries.	37
1.9	Schematic diagram showing the formation of L and H modes plasma pressure with edge transport barrier [13].	38
1.10	Sputtering yield of various materials as function of incident energy of deuterium ions. Courtesy [25].	41
1.11	Ignition curves as function of temperature for different concentrations of W for the case that $\tau_{He} = 5\tau_E$ along with the curve for no He and no W. Figure from reference [26].	42
1.12	Neoclassical (NEO) and turbulent (GKW) diffusion (left) and convective (right) contribution to W transport at 10.42 s for JET-ILW discharge 83351 [32].	43
2.1	Simplified picture of drift waves in a slab geometry with $k_x \ll k_y$. (Courtesy: [41])	51
2.2	A typical characteristics length scale of the linear growth rates for the ITG, TEM and ETG tokamak plasma instabilities. (Courtesy: [54]).	52
2.3	A typical dependence of linear growth rates γ (a) and real frequency ω_r (b) on the plasma beta for a standard tokamak parameters: $k_\theta \rho_i = 0.4$, $\epsilon = 0.16$, $\hat{s} = 1.0$, $q = 2.0$, $R/L_{TD} = 9.0$, $R/L_{nD} = 3.0$, $R/L_{Te} = 0.0$, $R/L_{ne} = 3.0$, no collisions and no toroidal rotation.	53
2.4	Parallel mode structure of electrostatic potential ϕ and vector potential $A_{ }$ for ITG mode (a) and (b), and KBM modes (c) and (d) as a function of parallel coordinate s for standard tokamak parameters given in figure 2.3.	55
3.1	Miller flux surfaces centred on $R_0 = R_{mil} = 1.0$ and $Z = 0$ plane with a minor radius of $r = 0.5$	66

4.1	Plasma input profiles for the JET discharge #75225 at 6-6.5 s obtained from GPR fits of experimental measurements as a function of the normalized toroidal flux ρ for (a) electron density, (b) electron temperature, (c) ion temperature, (d) toroidal rotation frequency, (e) safety factor q and (f) fast ion pressure profile obtained from PENCIL. In figure (b), the measurements are from two diagnostics HRTS and LIDAR and three offset points are from ECE measurements.	73
4.2	The radial derivatives of the total pressure β' (a) and center flux surfaces R'_{mil} (b) as a function of radial location ρ . The blue curve represents the case when fast ion pressure is included in the magnetic equilibrium and red line is for the case when the fast ion pressure is neglected in the magnetic equilibrium.	75
4.3	The linear growth rate for the most unstable mode at $k_\theta \rho_i = 0.35$ for $\rho = 0.15$ as a function of the number of grid points for the magnetic moment N_μ (a), the parallel velocity N_{v_\parallel} (b) and the number of points in the parallel direction per poloidal turns N_s (c).	76
4.4	Linear growth rate (left) and real frequency (right) spectra as a function of $k_\theta \rho_i$, at different radial locations: (a) and (b) at $\rho = 0.15$, (c) and (d) at $\rho = 0.33$, (e) and (f) at $\rho = 0.60$. The green curve represents the case without kinetic fast ions and without fast ion pressure in the magnetic equilibrium. The blue line correspond to the case without kinetic fast ions but the magnetic equilibrium includes the fast ion pressure. The red curve indicates the case with kinetic fast ions and fast ion pressure in the magnetic equilibrium, with the nominal fast ion pressure for the kinetic species (full line) or reduced by 30% (dashed line).	78
4.5	Growth rate and frequency of the most unstable modes as a function of radial location ρ . Full symbols are used for KBM modes and open symbols for ITG modes. The (red) full star symbol at $\rho = 0.33$ corresponds to a hybrid BAE/KBM mode destabilised due to kinetic fast ions. Same color code as in figure 4.4.	79
4.6	Linear growth rate (left) and real frequency (right) spectra as a function of β_e , at different radial locations: (a) and (b) at $\rho = 0.15$, (c) and (d) at $\rho = 0.33$, (e) and (f) at $\rho = 0.60$. The vertical dotted arrow shows the experimental β_e value at the reference location. Same colour coding as in figure 4.4	80
4.7	β_e (a) and magnetic shear \hat{s} values (b) as a function of the radial location ρ . In figure (a), the blue curve corresponds to the critical beta β_e^{crit} threshold of KBM, the red (dotted) curve represents the MHD β_{MHD}^{crit} limit and the green curve experimental beta β_e^{exp} values.	81
4.8	Normalised linear ion and electron heat fluxes (a) and (b), and electron particle flux (c) as function of β_e for $k_\theta \rho_i = 0.35$ at $\rho = 0.33$. The blue curves corresponds to fluxes due to $\mathbf{E} \times \mathbf{B}$ contribution, red due to magnetic flutter (A_\parallel) and green due to magnetic compression (B_\parallel). The vertical dotted line represents the transition from ITG to KBM range and vertical dotted arrow shows the experimental β_e value.	82

4.9	Parallel mode structure of ϕ (a), A_{\parallel} (b) and B_{\parallel} (c), as a function of the parallel coordinate s for the most unstable mode $k_{\theta}\rho_i = 0.35$ at $\rho = 0.15$. The blue curve corresponds the real part and the red line indicates the imaginary part.	83
4.10	2D poloidal cut of real part of electrostatic potential (ϕ_r) on the R and Z plane for the most unstable mode $k_{\theta}\rho_i = 0.35$ at $\rho = 0.15$	84
4.11	Growth rate as a function of the main ion pressure gradient for the most unstable mode $k_{\theta}\rho_i = 0.35$. Blue (open circle) curve for the case when the main ion density gradient (R/L_{nD}) is constant and the main ion temperature gradient (R/L_{Ti}) is varied, (red square) represents the case when the main ion temperature gradient is constant and the main ion density gradient is varied. The vertical (dotted) line indicates the experimental pressure gradient.	85
4.12	Growth rate as a function of the normalized electron temperature gradient for the most unstable mode $k_{\theta}\rho_i = 0.35$ at $\rho = 0.15$	85
4.13	Linear growth rate (a), and mode frequencies (b) as a function of magnetic shear \hat{s} for the most unstable mode $k_{\theta}\rho_i = 0.35$ at $\rho = 0.15$	86
4.14	Parallel mode structure of ϕ as a function of parallel coordinate s for three different values of magnetic shear \hat{s} for the most unstable mode $k_{\theta}\rho_i = 0.35$ at $\rho = 0.15$	86
4.15	β_e scans for various values of \hat{s} , for the most unstable mode $k_{\theta}\rho_i = 0.35$. The left panel (a) shows the linear growth rates and the right panel (b) shows the corresponding frequencies for the most unstable mode. The blue curve is for experimental value of \hat{s} and vertical (dotted) line represents the corresponding nominal value of β_e (3.2%).	87
4.16	Growth rate as a function of $ \beta' $, for the most unstable mode at $\rho = 0.15$ and $k_{\theta}\rho_i = 0.35$. The vertical dotted line indicates the nominal value of $ \beta' $	87
4.17	Growth rate as a function of T_e/T_i , for $k_{\theta}\rho_i = 0.35$. The vertical dotted line indicates the nominal value of T_e/T_i	88
4.18	Growth rates (a), and frequencies as function of q -profile, for $k_{\theta}\rho_i = 0.35$. The vertical dotted line indicates the nominal value of q	88
4.19	Growth rates as function of the toroidal rotation velocity u for fixed values of the toroidal rotation gradient u' , for $k_{\theta}\rho_i = 0.35$. The blue curve shows the case with the nominal value of $u' = 0.59$ and the red curve corresponds to $u' = 0$. The vertical dotted line indicates the nominal value of u	89
4.20	Growth rates as function of the toroidal rotation gradient u' for fixed value of toroidal rotation velocity u , for $k_{\theta}\rho_i = 0.35$. The blue curve shows the case with the nominal value of $u = 0.32$ and the red curve corresponds to $u = 0$. The vertical dotted line indicates the nominal value of u'	89

4.21	Growth rate (a) and frequency (b) as function of $k_\theta \rho_i$. The blue curve represents the standard case, the red curve corresponds to the case where collisions are retained and Carbon impurity is neglected in the simulations and the green curve where both C impurity and collision are neglected in the simulations.	90
4.22	Normalised linear ion and electron heat flux (a) and (b), and electron particle flux (c) as function of β_e for $k_\theta \rho_i = 0.35$ at $\rho = 0.15$. The blue curves corresponds to fluxes due to $\mathbf{E} \times \mathbf{B}$ contribution, red due to magnetic flutter (A_\parallel) and green due to magnetic compression (B_\parallel).	91
4.23	Normalised linear ion and electron heat flux (a) and (b), and electron particle flux (c) as function of \hat{s} for $k_\theta \rho_i = 0.35$ at $\rho = 0.15$. Same colour coding as in figure 4.22.	92
5.1	Time trace of nonlinear ion (a) and electron (b) normalised heat fluxes for the JET 75225 discharge at $\rho = 0.15$ for the reference case. The blue curve represents the $\mathbf{E} \times \mathbf{B}$ contribution to the fluxes, the red curve the magnetic flutter contribution (A_\parallel) and the green curve the magnetic contribution (B_\parallel).	97
5.2	Time trace of flux-surface averaged zonal modes ($k_\theta = 0$ modes) for the three lowest radial modes (a) and the amplitudes of zonal modes as function of radial (k_r) modes (b) for the JET 75225 discharge at $\rho = 0.15$ for the reference case.	97
5.3	$ \phi ^2$ and $ A_\parallel ^2$ spectra as a function of poloidal wave vector $k_\theta \rho_i$ (a) and (b) and radial wave vector $k_r \rho_i$ (c) and (d) for the reference case at $\rho = 0.15$. The blue curve represents the nonlinear simulations results, the red and magenta curves are the k_θ^2 and k_θ^{-3} fit, and the green curve is $k_r^{-3.3}$ fit.	98
5.4	Nonlinear ion heat fluxes (a), electron heat fluxes (b), electron particle fluxes (c), ion momentum fluxes (d) and effective Prandtl number (Pr) (e) as a function of β_e , at $\rho = 0.15$. The solid black line represents the total fluxes. Other colour coding is same as in figure 5.1.	99
5.5	Nonlinear ion heat fluxes (a), electron heat fluxes (b) and electron particle fluxes (c) as a function of magnetic shear \hat{s} , at $\rho = 0.15$. Same colour coding as in fig. 5.1.	100
5.6	Linear growth rate as a function of radial wave vector ($k_r \rho_i$) for three different values of $k_\theta \rho_i$. The blue curve corresponds to $k_\theta \rho_i = 0.3$, the red curve for $k_\theta \rho_i = 0.4$ and the green represents $k_\theta \rho_i = 0.5$	102
5.7	Linear ion (a), electron heat fluxes (b), and particle fluxes (c) normalised with the mode amplitude as a function of $k_\theta \rho_i$, at $\rho = 0.15$. The blue (*) curve corresponds to flux contribution due to $\mathbf{E} \times \mathbf{B}$, the red (x) for magnetic flutter and green (+) for magnetic compression part.	104

- 5.8 Normalized quasilinear spectra and GKW non-linear saturated electric potential for different plasma beta $\beta_e = 2.4\%$ (a), $\beta_e = 3.2\%$ (b), $\beta_e = 3.8\%$ (c) with nominal magnetic shear ($\hat{s} = 0.05$), and for higher magnetic shear $\hat{s} = 0.1$ at nominal plasma beta ($\beta_e = 3.2\%$)(d) as function of $k_\theta \rho_i$, at $\rho = 0.15$. The quasi-linear spectra are normalized to the maximum of the nonlinear ones. The red curve (square) corresponds to nonlinear, the blue (+) to the quasi-linear model \mathcal{W}_1 , the green (\times) for \mathcal{W}_2 and the magenta (*) for \mathcal{W}_3 105
- 5.9 Normalized quasilinear spectra and GKW non-linear saturated vector potential for different plasma beta $\beta_e = 2.4\%$ (a), $\beta_e = 3.2\%$ (b), $\beta_e = 3.8\%$ (c) with nominal magnetic shear, and for higher magnetic shear $\hat{s} = 0.1$ at nominal plasma beta (d) as function of $k_\theta \rho_i$, at $\rho = 0.15$. The quasi-linear spectra are normalized to the maximum of the nonlinear ones. The red curve (square) corresponds to nonlinear, the blue (+) to the quasi-linear model \mathcal{W}_1 , the green (\times) for \mathcal{W}_2 and the magenta (*) for \mathcal{W}_3 106
- 5.10 $\mathbf{E} \times \mathbf{B}$ ion and electron heat fluxes (a) and particle and ion momentum flux (b) as a function of β_e , at $\rho = 0.15$. The solid lines are for the non-linear results and the dashed lines for the quasilinear models. The plus signs + corresponds to the QL model \mathcal{W}_1 , the crosses \times are for \mathcal{W}_2 and the star * are for \mathcal{W}_3 106
- 5.11 $\mathbf{E} \times \mathbf{B}$ ion and electron heat fluxes (a) and particle and ion momentum flux (b) as a function of the magnetic shear \hat{s} , at $\rho = 0.15$. The solid lines are for the non-linear results and the dashed lines for the quasilinear models. The plus signs + corresponds to the QL model \mathcal{W}_1 , the crosses \times are for \mathcal{W}_2 and the star * are for \mathcal{W}_3 107
- 5.12 Parity factor for the A_{\parallel} fluctuations and Φ fluctuations as a function of $k_\theta \rho_i$ in non-linear simulations, at $\rho = 0.15$ 108
- 5.13 Magnetic flutter electron heat flux as a function of β_e , at $\rho = 0.15$. The solid lines are the non-linear results and the dashed lines are for the quasilinear models. The plus signs + corresponds to QL weight \mathcal{W}_1 , the crosses \times are for \mathcal{W}_2 and the star * are for \mathcal{W}_3 108
- 5.14 Ratio of the A_{\parallel} fluctuations amplitude, $\mathcal{A}_{A_{\parallel}}^2$ to the total fluctuation amplitude \mathcal{A}^2 as a function of $k_\theta \rho_i$ in linear and non-linear simulations, at $\rho = 0.15$ 109
- 5.15 Magnetic flutter ion and electron heat fluxes as a function of β_e (a) and magnetic shear (b) at $\rho = 0.15$. The solid lines are the non-linear results and the dashed lines are for the quasi-linear models. The plus signs + corresponds to the model \mathcal{W}_1 , the crosses \times are for \mathcal{W}_2^* and the star * are for \mathcal{W}_3^* 110
- 5.16 Quasilinear ion heat heat fluxes for the QL model \mathcal{W}_3 as a function of R/L_{Ti} for the nominal value of R/L_{ne} (a) and R/L_{ne} with kinetic fast ions and $R/L_{Ti} = 3.2$ (b) at $\rho = 0.15$. The blue curve is for the case without kinetic fast ions and nominal value of $R/L_{ne} = 1.5$ and the red curve is for the case with kinetic fast ions. 111

A.1	Schematic of a poloidal cross section of a tokamak representing coordinates and notations.	118
A.2	Physical picture of toroidal ITG.	125
A.3	Growth rate (γ) as a function of density gradient scale length (R/L_N) for a fixed value of (R/L_T) (a) and temperature gradient scale length (R/L_T) for a fixed value of (R/L_N) (b) for toroidal ITG using fluid model.	127
A.4	Growth rate (γ) as a function of density gradient scale length (R/L_N) and temperature gradient scale length (R/L_T) for toroidal ITG using fluid model.	128
A.5	Growth rate (γ) as a function of density gradient scale length (R/L_n) and temperature gradient scale length (R/L_T) for $k_y\rho = 0.3$ (a) and $k_y\rho = 0.7$ (b), for slab ITG using fluid model and for a fixed value of $q=1.1$	129
A.6	Growth rate (γ) as a function of density gradient scale length (R/L_n) and temperature gradient scale length (R/L_T) for $q = 1.1$ (a) and $q = 5.5$ (b), for slab ITG using fluid model and for a fixed value of $k_y\rho = 0.3$	129
A.7	Growth rate (γ) as a function of density gradient scale length (R/L_N) for a fixed value of (R/L_T) (a) and temperature gradient scale length (R/L_T) for a fixed value of (R/L_N) (b) for slab ITG using the fluid model for $k_y\rho = 0.3$ and $q = 1.1$	130
A.8	Growth rate ($\hat{\gamma}$) as function of R/L_T for a fixed value of $R/L_n = 1$ (blue curve) and $R/L_n = 3$ (red curve) for the kinetic model. Other parameters are $k_y\rho = 0.3$, $k_z = 0$, $\omega_D = -k_y\rho$, $\omega_D = k_y\rho/2$	132
A.9	Comparison of growth rate ($\hat{\gamma}$) as function of R/L_T for a fixed value of $R/L_n = 3$, $k_y\rho = 0.3$, $k_z = 0$, $\omega_D = -k_y\rho$, and $\omega_D = k_y\rho/2$ for fluid model (blue curve) and kinetic model (red curve).	132

List of Tables

4.1	Normalized input parameters used in GKW simulations for the JET 75225 discharge selected in the time interval 6.0-6.5 s.	74
4.2	Miller parameters for the magnetic equilibrium including the fast ion pressure.	75
4.3	Miller parameters for the magnetic equilibrium without including the fast ion pressure.	75
4.4	Numerical grid parameters used for simulations of JET discharge 75225.	76
5.1	Normalized input parameters used in GKW simulations for the non-linear gyro-kinetic simulations at $\rho = 0.15$. For the detailed list see table 4.1.	96

Nomenclature

B_φ, B_θ	The toroidal and poloidal magnetic field
P_{fusion}	Fusion power released
P_h	Net external heating power
Pr	Prandtl number
Q	Fusion power gain or amplification factor
$R/L_n, R/L_T$	The normalized density and temperature gradient length scale
Λ	Plasma parameter
Ω_{tor}	Toroidal rotation frequency
α	The ballooning parameter
β	Kinetic parameter (ratio of plasma pressure to the magnetic pressure)
β_{crit}	The critical β limit for Kinetic Ballooning Modes (KBMs)
ϵ	The aspect ratio
η	Plasma resistivity
γ	Linear mode growth rate
\hat{s}	The magnetic shear
λ_D	Debye length
ν	Collisionality
ω_c	Cyclotron (angular) frequency
ω_r	Real frequency of the linear Fourier modes

ω_{*pi}	Plasma ion diamagnetic frequency
ϕ, A_{\parallel}	Perturbed electrostatic potential and vector potential
ρ	Toroidal flux coordinate
ρ_s	Larmor radius of considered species
σ	Fusion cross-section
τ_e	Energy confinement time
φ, θ	The toroidal and poloidal angle
a	The minor radius of the last closed flux surface (LCFS)
k_{θ}, k_r	The binormal and radial wave vector
n, T	Density and temperature
q	Safety factor
r, R_0	The minor and major radius of a tokamak
s	The parallel coordinate
u	Toroidal rotation velocity normalized in GKW coordinates
v_{\perp}, v_{\parallel}	Component of velocity perpendicular and parallel to the magnetic field
v_{ths}	The thermal velocity of the considered species
E, B	Electric and magnetic field
J	The current density

1

Introduction

1.1 Nuclear fusion as a potential energy source

During the last two centuries, the world population has been increasing rapidly due to the advancement of technology, scientific knowledge and various other factors. The resulting large population requires a vast amount of energy and electricity for its rapid economic growth. Presently, most of the world energy demand (about 80%) is still sustained by burning enormous amounts of fossil fuels which includes coal, oil, and natural gas [1]. However, the supply of fossil fuels is limited and rapidly exhausted by massive consumption. Also, the use of fossil fuels emits carbon dioxide and other deleterious gases. It causes climate change problems such as global warming and air pollution that could be very harmful not only to our environment but also for human health. A change to renewable sources of energy such as wind, solar, and hydroelectric energy is attractive from an environmental point of view. However, the limitations associated with the low energy density, storage and transport make them not sufficient for long term on a large scale.

Therefore, additional options for abundant, reliable and clean energy production are needed. One of the possible solutions to this problem is the use of renewable, nuclear energy sources for electricity production. Nuclear energy is either produced by fission or fusion reactions. In nuclear fission, a massive radioactive element such as Uranium-235 is split into two lighter parts and releases a large amount of energy. The nuclear fission power plants are free from greenhouse gases emission and are already present in many countries for electricity production. However, the safe handling and storage of long-lived radioactive waste materials, health hazards problems in case of nuclear accidents, nuclear proliferation for illegal activities, limited uranium supplies and a considerable amount of capital cost to build these plants are still a big concern. Nuclear fusion energy, which consists in fusing two light nuclei into a heavier nucleus,

is considered as a viable option for a clean, vast, dense and safe source of energy and could play a decisive role in the long-term solution. However, scientific and technological challenges are hindering the experimental realisation of this technology for more than half a century. Consequently, a large portion of research in this field is mainly devoted to overcoming these scientific and technological challenges to build an experimental fusion device that can be used to demonstrate the scientific feasibility of nuclear fusion for electricity production. This thesis addresses some critical issues related to the understanding of turbulent transport, which limits the performance in the present as well as in future fusion devices. The fundamental concepts related to the fusion which are necessary to understand this thesis are introduced in the remainder of this chapter. The emphasis is placed on physical descriptions over detailed mathematical formalism (which is described in later chapters).

1.2 Basis of thermonuclear Fusion

One of the crucial applications of plasma physics is in controlled thermonuclear fusion to produce energy. Nuclear fusion is also the source of energy production in stars, including the Sun. It is a process where two light nuclei fuse together to form a heavier nucleus and subatomic particles (neutron or proton). The resulting heavier nuclei have slightly less mass than the fusing elements and this mass difference (Δm) also called mass defect in the process appears as energy (ΔE) according to famous Einstein's relation

$$\Delta E = \Delta mc^2, \quad (1.1)$$

where c is the speed of light. The strong nuclear interaction gives the physical energy source of nuclear fusion and the released energy is directly related to the nuclear binding energy. The binding energy is the amount of energy that would be released when individual protons and neutrons combine into a single nucleus or the minimum amount of energy that is required to break up its nucleus into individual constituents. Dividing the binding energy by its mass number $A = Z + N$, where Z and N being the atomic and neutrons number in the nucleus, binding energy per nucleon is obtained, which is shown in figure 1.1 for different atomic elements. Heavy atom, such as Uranium release energy through nuclear fission by splitting into lighter nuclei, whereas lighter nuclei release energy by fusing together. As illustrated in figure 1.1, the binding energy per nucleon for Helium-4 (${}^4\text{He}$) fusion is 7.07 MeV/nucleon and for nuclear fission of Uranium-235 is 7.59 MeV/nucleon. A fusion process generating ${}^4\text{He}$ nuclei yields one of the most abundant energy gains possible via fusion.

To induce a fusion reaction, the two light nuclei need to be brought within the range of the short attractive nuclear force. In order to reach this distance, the fusing nuclei must have sufficiently high kinetic energy to overcome the electrostatic Coulomb repulsion between the two positively charged nuclei. This is achieved by heating the particles to a very high temperature (of the order of 100 million-degree Celsius), such that the thermal velocities of the particles are high enough. At these large temperatures, charged particles are fully ionised and form a new state of matter called the plasma state. Plasmas exhibit a wide variety of physical phenomena involving electromagnetic fluid and kinetic effects.

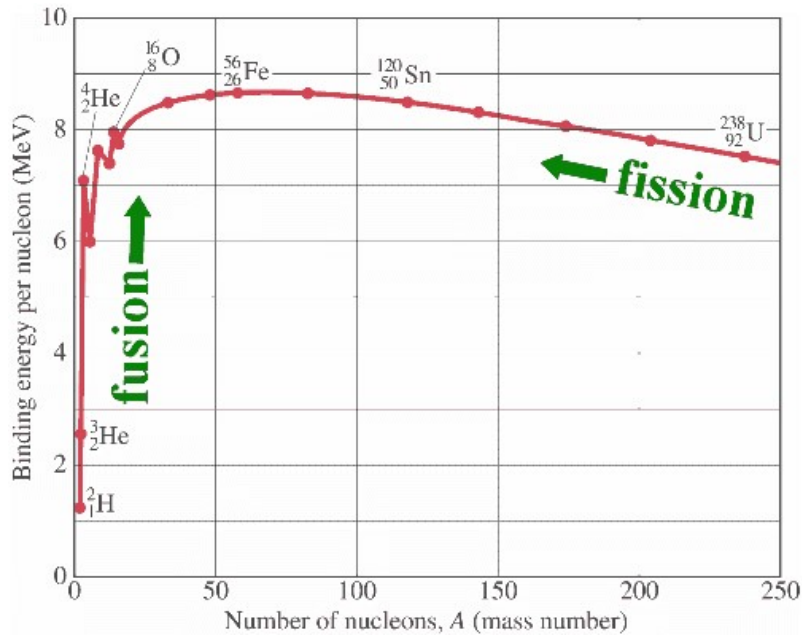


Figure 1.1 – Binding energy per nucleon versus mass number plots for various atomic elements. Fig. courtesy: Pearson Prentice Hall.

1.3 Plasma: the fourth state of matter

The basic description of plasmas can be found in any standard textbook. In [2], a plasma is defined as "a quasi-neutral gas of charged and neutral particles which exhibit collective behaviours". Here quasi-neutral refers to a condition in which plasma is considered neutral enough that $n_e \simeq n_i$ approximately holds but not neutral enough that all electromagnetic forces vanish. In a plasma, the potential energy of a particle due to its nearest neighbours is much smaller than its kinetic energy. The plasma state is also known as the fourth state of matter. However, not every ionised gas can be called as plasma. For a gas to qualify as a plasma requires that the number of particles inside a sphere (called Debye sphere) with radius λ_D must be sufficiently larger than one, i.e.

$$\Lambda \equiv n_0 \lambda_D^3 \gg 1, \quad (1.2)$$

where $\lambda_D = \sqrt{(T/4\pi n_0 e^2)}$ is called Debye length, which measures the shielding distance or thickness of the sheath. Here n_0 is the density of each species, T is the temperature in eV units, and e is the charge of an electron. Λ is called the plasma parameter.

1.3.1 Reaction rate and fusion cross-section

The fusion cross-section (σ), is the probability of obtaining a fusion reaction as a function of the relative velocity of the reactant nuclei. The reaction rate is the number of fusion reactions between two species of density n_1 and n_2 , taking place in

the plasma per unit volume per unit time. Thus,

$$R = n_1 n_2 \sigma v, \quad (1.3)$$

with v is the relative velocity of the colliding particles. In a plasma, all particles do not have the same velocity and it is relevant to integrate the reaction rate over the velocity distribution to obtain the average number of reactions per unit volume and time

$$\mathcal{R} = n_1 n_2 \langle \sigma v \rangle. \quad (1.4)$$

Here, $\langle \sigma v \rangle$ is the reaction parameter and $\langle \rangle$ represents an average over a Maxwellian velocity distribution function. For a given total density, the reaction rate is maximum when $n_1 = n_2$.

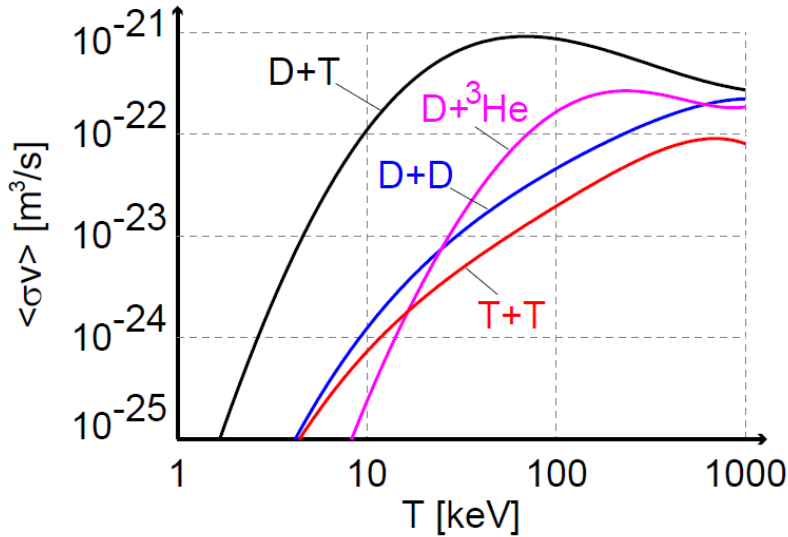


Figure 1.2 – Reaction parameter $\langle \sigma v \rangle$ as a function of temperature. Courtesy [3].

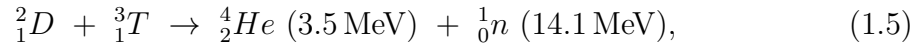
The reaction parameter $\langle \sigma v \rangle$ for various fusion reactions as function of temperature is shown in figure 1.2. As seen, the DT –reaction has the highest reaction parameter as compared to other fusion reactions at low temperature with a broad maximum for ion temperatures T_i between 20 keV¹ and 100 keV. Below an ion temperature of 10 keV, there is a steep decrease in the reaction parameter, and the fusion plasma therefore needs to have a minimum temperature of 10 keV.

1.3.2 Fusion reactions

The most feasible thermonuclear reaction on Earth is the fusion of two hydrogen isotopes deuterium (2_1D) and tritium (3_1T), into Helium (4_2He) and a neutron, see figure 1.3, because it has a high fusion cross-section at comparatively lower temperatures, 10-20 keV, as compared to other reactions of interest. The broad fusion cross-section of the D-T reaction arises due to the existence of a resonance

¹Here temperature T is expressed in energy units, i.e. kT , where k is the Boltzmann's constant

between the kinetic energy and excited state of the ${}^5_2\text{He}$ nucleus.



where n represents a neutron that carries 14.1 MeV (80%) of the released energy and helium nucleus that gets 3.5 MeV (20%) of the released energy. The released energy is available as the kinetic energy of the products. The cross-section of this reaction reaches a maximum value of $\sigma_{DT,max} = 4.9 \times 10^{-28} \text{ m}^2$ at a collision energy of 64 keV. Nuclear fusion can be achieved by confining a sufficiently hot D-T plasma and heating the mixture until the thermal velocity of the particles is sufficiently high to overcome the electrostatic repulsion. This process is referred to as thermonuclear fusion. The reactions come mainly from the tail of the Maxwellian velocity distribution. Thus, the actual temperature needed for the D-T thermonuclear fusion reaction is lower than the temperature corresponding to the maximum cross-section for the D-T reaction.

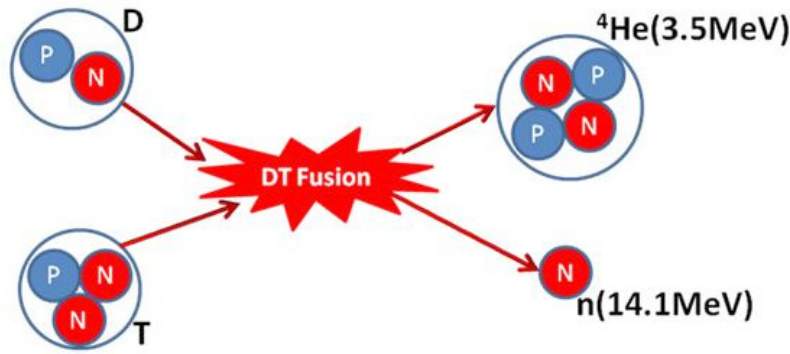
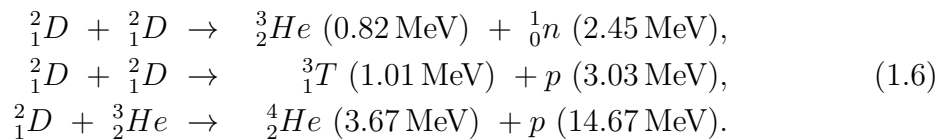


Figure 1.3 – Schematic of a D-T fusion reaction forming a helium nucleus.

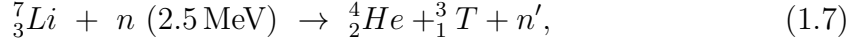
Some other thermonuclear fusion reactions of interest are based on the deuterium. These are:



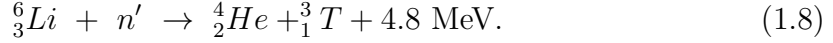
The optimum energy required to initiate D-D reactions is higher than the optimum for D-T results. The second and third equations of 1.6 do not produce neutrons but charged particles. Therefore, the activation of the reactor wall is reduced, a neutron moderator is not required and the fusion products can be confined with the magnetic field. However, the second equation above produces tritium, so the D-D reaction will not be ultimately tritium free and D-T reactions will also occur.

The deuterium is very abundant, cheaply available and can be extracted naturally from ocean water. The available quantity of deuterium in seawater can provide 10^{11} times more electrical energy than the annual world energy consumption. The tritium has a short half-life of 12 years and is practically non-existent in nature.

Tritium, however, can be bred from Lithium by using the neutrons released in the fusion reaction. The Lithium is present naturally with two isotopes with a natural abundance of 7.4% for ${}^6_3\text{Li}$ and 92.6% for ${}^7_3\text{Li}$. To capture a fast neutron (14.07 MeV) produced by the $D - T$ reaction, the ${}^7_3\text{Li}$ can be used



and this slow neutron n' is again captured with the reaction



1.3.3 Conditions for a fusion reaction: Lawson criteria

As discussed above, very high temperatures are required in order to initiate fusion reactions, but to maintain these high temperatures, the various energy losses present in the system need to be compensated by external heating. Therefore, for a net energy gain, large temperature and fusion reaction rate alone are not sufficient, the energy losses need to be sufficiently small so that external input power supplied to maintain the plasma at the desired temperature remains less than the fusion output power. This is usually expressed by the energy confinement time (τ_e), which characterises the time required for the stored energy to leave the plasma, once all the external heating systems are switched off. It describes the ratio of total plasma energy to power losses:

$$\tau_e = \frac{W_p}{P_h - dW_p/dt}, \quad (1.9)$$

where W_p is the total internal energy of plasma and P_h is the net external heating power. The fusion power gain or the Q factor defined as the ratio of the fusion power output to the auxiliary input heating supplied from the outside to sustain the reaction in steady-state: $Q = P_{\text{output}}/P_{\text{input}} = P_{\text{fusion}}/P_{\text{th}}$. Thus, the minimum criterion for a successful fusion reactor is $Q = 1$. The condition $Q = 1$ is called the break-even condition, which implies output fusion power equals to the auxiliary input power. On the other hand, a self-sustaining fusion reaction to achieve ignition condition is possible when $P_h \rightarrow 0$ or $Q \rightarrow \infty$, which means all energy losses of the plasma are balanced by the α -particles² produced in a D-T reaction and no external heating power is required. This criterion is known as the famous Lawson's triple product [4]. For a 50%-50% mix of deuterium and tritium, this condition reads

$$nT\tau_e \geq 3.0 \times 10^{21} \text{ m}^{-2} \text{ keV s}. \quad (1.10)$$

where n is the electron density of a pure D-T 50/50 mix.

This condition brings out the minimum requirements for the plasma density, energy confinement time and temperature to achieve ignition. For example, the ignition condition would be reached for $n = 10^{20} \text{ m}^{-3}$, $T = 10 \text{ keV}$ and $\tau_E = 3 \text{ s}$. Therefore, great efforts have been devoted by the scientific community to maximise this product.

²Helium nuclei with +2 charge (${}^4_2\text{He}^{+2}$) are called α particles.

There are two main plasma confinement approaches subject to present-day research to achieve ignition condition on Earth. The first one consists of maximising the ion density (of the order of 10^{31} m^{-3}) with a decrease of energy confinement time ($\tau_E \sim 10^{-11} \text{ s}$) and is referred to as inertial confinement fusion (ICF). In this scheme, a solid DT pellet with a small diameter of about 1 mm is compressed and heated using a laser or a beam of heavy ions. The two largest experimental facilities based on ICF are the National Ignition Facility (NIF) [5] in the US and the Laser Megajoule [6] in France. The other scheme is the magnetic confinement fusion in which magnetic fields confine the plasma. In this case, the ion density is much smaller (of the order of 10^{20} m^{-3}), but the energy confinement time is considerably larger (of the order of a s). In this thesis, interest has been focused on the magnetic confinement fusion scheme.

1.3.4 Brief historical review of nuclear fusion

Daniel Clery has well described the past 70 years of nuclear fusion history in his book "A piece of the Sun" [7]. The concept of nuclear fusion was proposed for the first time in the 1920's when the British astrophysicist Arthur Eddington suggested that the fusion of hydrogen nuclei into Helium could be the origin of energy production in stars. A significant breakthrough in this direction came in the 1930's when Hans Bethe discovered that nuclear fusion is possible and is the source of energy in the Sun. In the beginning of 1940's, researchers started looking at possibilities to control thermonuclear reactions to produce energy on the Earth. The race of nuclear weapons during the Second World War increased the interest in the nuclear fusion manifold. The first thermonuclear weapon, called H-bomb, was tested in 1952. The use of nuclear fusion to produce energy is a more demanding task because it has to be controlled a plasma reaching temperatures of hundreds of millions of degrees contained in a reactor. A significant breakthrough in this direction came in 1950 when soviet scientists Andrei Sakharov and Igor Tamm suggested a way to contain the hot plasma away from the chamber walls by the use of magnetic fields. They proposed a promising design of a magnetic confinement fusion device in the Kurchatov Institute in Moscow; this doughnut-shaped device was called a tokamak. The idea of this device was to confine the plasma in a toroidal chamber with the help of a toroidal magnetic field created by external field coils and to induce a toroidal current within the plasma to have a resulting helical magnetic field. Following the concept of a tokamak, Lyman Spitzer proposed a new magnetic confinement concept in 1951 for the confinement of plasma by the pinch effect, and later device called a Stellarator. By the mid-50s, several magnetic confinement devices were operating in the USA, United Kingdom, USSR, France and Japan. The development of fusion science was strongly impacted by the cold war and lack of knowledge sharing between the world countries until 1958 when the international IAEA meeting was held in Geneva. The idea of Stellarator dominated the fusion research throughout the 1950 and 1960 until Soviet scientist Lev Artsimovich ousted it by the more efficient tokamak concept. In 1969, he made an incredible announcement that experimental research on tokamak systems had reached a temperature of 1 keV (more than 10 million degrees Celsius) for the first time. This claim was later verified by UK scientists who visited their Soviets counterparts in Moscow.

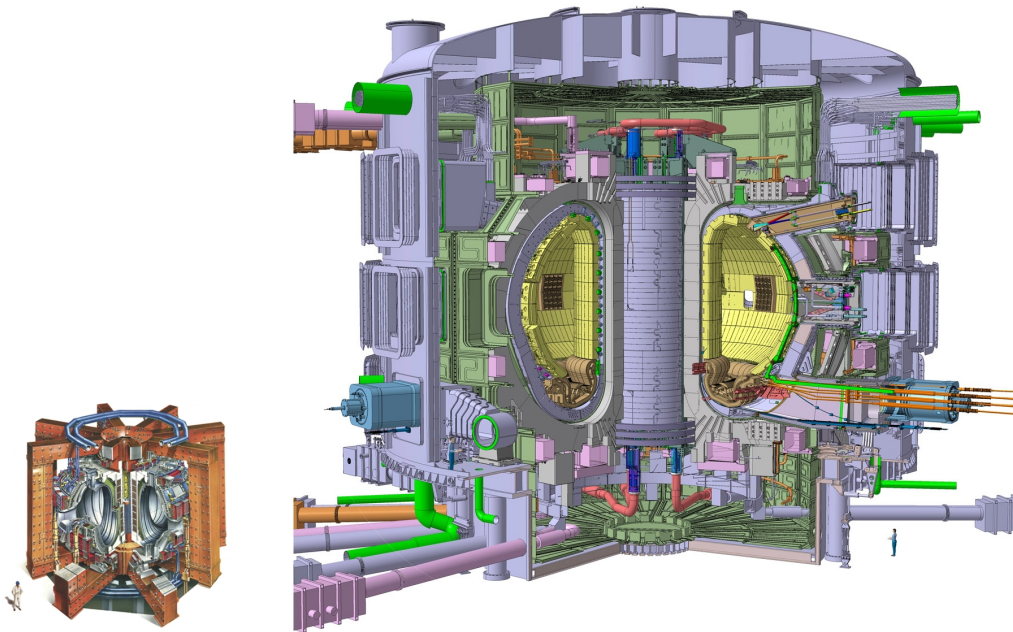


Figure 1.4 – Schematic diagram of JET (on left side) and ITER (on right side) tokamak. Source: <https://www.iter.org/>

By the 1970s, the scientific community realised that attaining fusion energy would be one of science’s greatest challenge and would require collaboration with other people. In this direction, European countries came together and proposed design work on the Joint European Torus (JET), in 1973. The JET tokamak (shown in the left of figure 1.4), built-in Culham in Oxford, UK, is currently the world’s biggest tokamak, and is an example of international collaboration. In 1997, JET set the current world record for fusion output of 16 MW from an input of 25 MW of heating power and with a 50 – 50 mix fuel of deuterium and tritium [8]. The obtained fusion gain factor was $Q = 0.63$.

The next milestone is to achieve a break-even condition, where the produced energy is equal to the external heating supplied. To demonstrate the scientific and technical viability of nuclear fusion energy for peaceful use, the US president Ronald Reagan and General Secretary Mikhail Gorbachev of the former Soviet Union signed an agreement in November 1985 to construct a large-scale tokamak capable of producing net fusion power. This project, known as ITER³, was approved in 2006 and is currently under construction in the south of France. It will be the world’s largest tokamak with a plasma volume 8 times larger than JET (shown on the right of figure 1.4). With the goal to demonstrate the feasibility of fusion as an energy source on the scale needed for a commercial power plant, ITER is designed to achieve $Q = 10$. It aims for the time, to produce more sustained fusion power than the input power, i.e., it will produce 500MW of fusion power for an injected power of 50MW during 400 to 600s [9].

³ITER was also known as International Thermonuclear Experimental Reactor before, but now replaced by the acronym "The way" in Latin

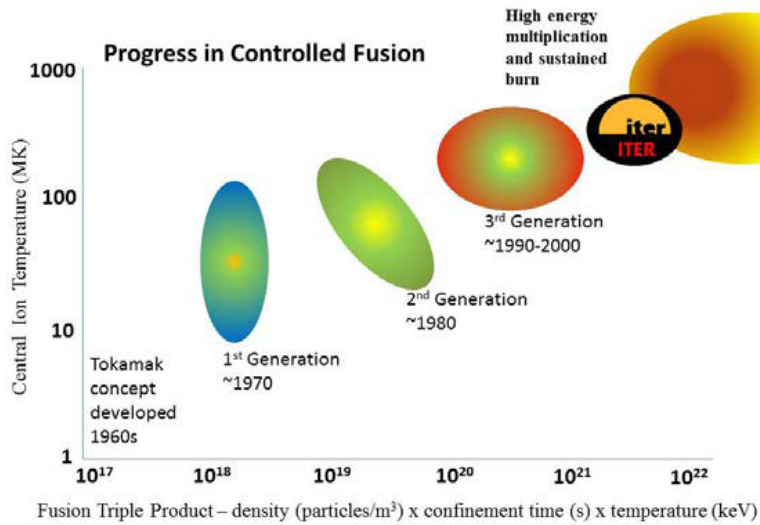


Figure 1.5 – Core ion temperature as a function of fusion triple product [10].

Over the past 70 years, significant research on magnetic confinement lead to various tokamaks designs with different geometries, magnetic properties and heating and diagnostic systems. Considerable progress has been made during this period in the achievement of high fusion triple products, as shown in figure 1.5, in controlling the main plasma instabilities and in increasing the heating efficiency. However, in the presence of these extreme temperature conditions, strong gradients inevitably lead to the development of various instabilities which drive turbulent transport in the plasma and limit confinement. Understanding of the plasma instabilities that can give rise to turbulence in the central part, $r/a < 0.3$, of ITER plasmas is one of the motivations of this work.

1.4 Tokamaks and magnetic confinement

1.4.1 Introduction to tokamaks

In the last section, it has been seen that the plasma needs to be confined for a sufficiently long time to achieve ignition. The main difficulty lies in insulating the plasma from the external walls and maintain it at a high temperature. Since the external electromagnetic force influences the dynamics of charged particles, the present magnetic confinement experiments rely on strong magnetic fields to achieve this goal. Such a strong magnetic field confines the plasma by keeping the charged particle moving in a helical trajectory around the field lines as a result of the Lorentz force, $\mathbf{F} = q(\mathbf{E} + \mathbf{v} \times \mathbf{B})$, where q is the charge of the particle, \mathbf{v} is its velocity and \mathbf{E} , \mathbf{B} are the electric and magnetic fields respectively. The extent of the particle trajectory in the direction perpendicular to the magnetic field is called the Larmor radius, and defined as $\rho_s = mv_{\perp}/qB$, where v_{\perp} is the component of velocity perpendicular to the magnetic field B and s represents the considered species of mass m and charge q .

The two main classes of magnetic confinement configurations are:

- ◇ linear configurations: where the magnetic field lines are open and the plasma can leave the confinement zone at either end of the system (for example magnetic mirror system);
- ◇ toroidal systems: where the magnetic field lines are endless, i.e., completely contained within a toroidal confinement region (for example tokamak).

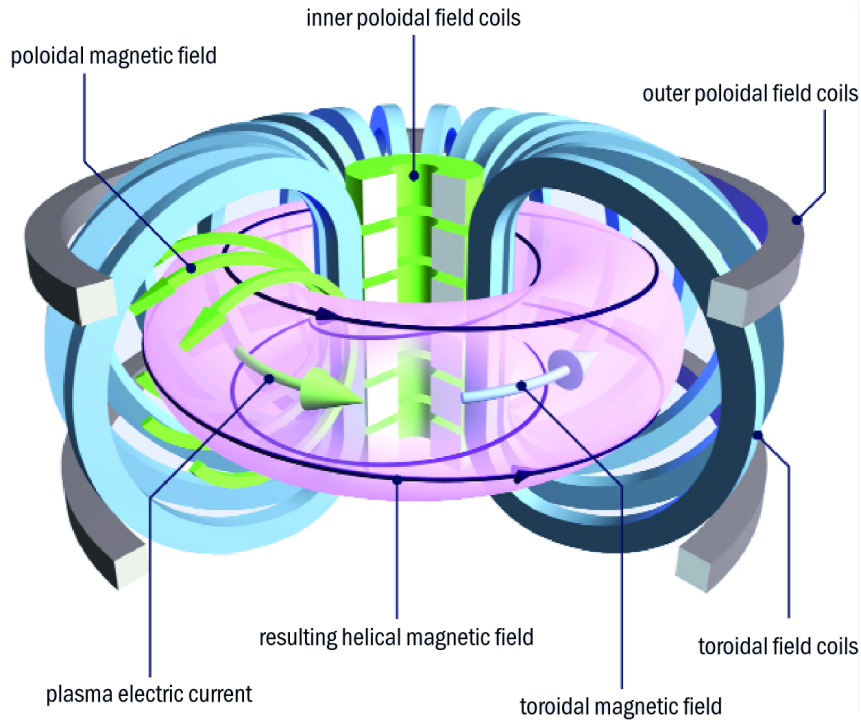


Figure 1.6 – Illustration of a tokamak configuration (Courtesy: Eurofusion [11]).

In open magnetic field configurations, plasma is lost at both ends due to very large parallel transport in the magnetic field line direction. These end losses can be avoided by closing the magnetic field lines into circles as in a torus. However, since $\nabla \times \mathbf{B} = \mu_0 j_c \Rightarrow 2\pi R B = \mu_0 I_c \Rightarrow B = \mu_0 I_c / 2\pi R$, where j_c and I_c are the current density and current flowing in the toroidal field coils. A purely toroidal field varies as $B \sim 1/R$ (with R being the major radial coordinate of the torus). This implies a radial gradient in the magnetic field with increasing field strength towards the axis of the torus. Magnetic field gradients and the curvature of the field lines lead to an extra drift velocity of ions and electrons in opposite vertical directions (curvature and $\nabla \mathbf{B}$ -drift). These drifts in turn lead to a separation of charges and to the build-up of an electric field. The resulting electric field is transverse to the toroidal magnetic field and causes a loss of the plasma due to a radial $\mathbf{E} \times \mathbf{B}$ drift. This outward drift motion can be avoided by making the field lines wind up over a toroidal surface, which is called a magnetic surface. This is produced by an additional poloidal field \mathbf{B}_p . The particles which follow the magnetic field lines drift alternatively inward and outward depending on the position of the field line with respect to the midplane. It leads to a cancellation of the vertical drifts on average. Therefore, a combination

of toroidal and poloidal field can confine the plasma. The poloidal magnetic field can be produced either by external coils such as in Stellarator or by driving plasma current in toroidal direction, as in the tokamak.

Figure 1.6 shows a schematic of a tokamak configuration with its main elements. The tokamak is the acronym for the Russian word "**T**oroidalnaya **K**amera **M**agnitnymi **K**atushkami", meaning toroidal chamber with magnetic coils. It is a toroidal plasma confinement system in which toroidal field coils generate a strong toroidal magnetic field (B_φ). A poloidal field (B_θ) is produced by a plasma current (I_p) flowing in the toroidal direction. In most tokamaks, the toroidal plasma current is driven inductively by a transformer, where the central solenoid acts as the primary winding while the plasma acts as the secondary winding of the transformer. This inductive drive inherently imposes a pulsed mode operation: the current cannot be maintained indefinitely. To achieve a steady-state operation, the plasma current must be driven non-inductively. The self-generated bootstrap current and auxiliary current drive system can provide non-inductive currents. The combined effect of toroidal and poloidal magnetic fields results in helical field lines spanning the closed nested toroidal surfaces. These nested surfaces of constant magnetic flux are called magnetic surfaces or flux surfaces as described in figure 1.7. Such a toroidal geometry under consideration along with the plasma pressure results in a hoop force trying to expand the plasma torus radially outward. To balance this force in order to achieve radial equilibrium, a vertical magnetic field is applied (B_v), which gives an inward radial force through interaction with toroidal plasma current. Moreover, to control the plasma shape as well as plasma position, tokamaks are equipped with additional poloidal field (PF) coils.

The helical magnetic field in an axi-symmetric tokamak is usually expressed as:

$$\mathbf{B} = I(\psi)\nabla\varphi + \nabla\psi \times \nabla\varphi, \quad (1.11)$$

where ψ is the poloidal magnetic flux normalised to 2π , φ is the toroidal angle and $I(\psi) = RB_\varphi$ is a flux function, i.e. a quantity constant on a flux surface. In equation 1.11, the first term on the right-hand side represents the toroidal magnetic field component B_φ , and the second term corresponds to the poloidal magnetic field B_θ .

In equilibrium, the plasma pressure ∇p and the Lorentz ($\mathbf{J} \times \mathbf{B}$) forces balance each other:

$$\nabla p = \mathbf{J} \times \mathbf{B}, \quad (1.12)$$

where p is the pressure and \mathbf{J} is the current density. From the above equation 1.12

$$\mathbf{J} \cdot \nabla p = 0, \quad \text{and} \quad \mathbf{B} \cdot \nabla p = 0, \quad (1.13)$$

which shows that the \mathbf{J} and \mathbf{B} are perpendicular to the pressure gradient ∇p and must lie on surfaces of constant pressure. Flux surfaces are commonly labelled with the poloidal or toroidal magnetic flux. In the limit of large aspect ratio, $\epsilon = a/R \ll 1$, and of circular and concentric flux surfaces, using the cylindrical coordinates (r, θ, φ)

as represented in the figure 1.7, the toroidal magnetic field can be simply written as:

$$B_\varphi = \frac{B_0 R_0}{R_0 + r \cos\theta} \sim B_0 \left(1 - \frac{r}{R_0} \cos\theta\right), \quad (1.14)$$

with $\mathbf{B} = B_\varphi \mathbf{e}_\varphi + B_\theta \mathbf{e}_\theta$ and r is the minor radius of flux surface, B_0 is the reference magnetic field on the magnetic axis and R_0 is the major radius of the plasma.

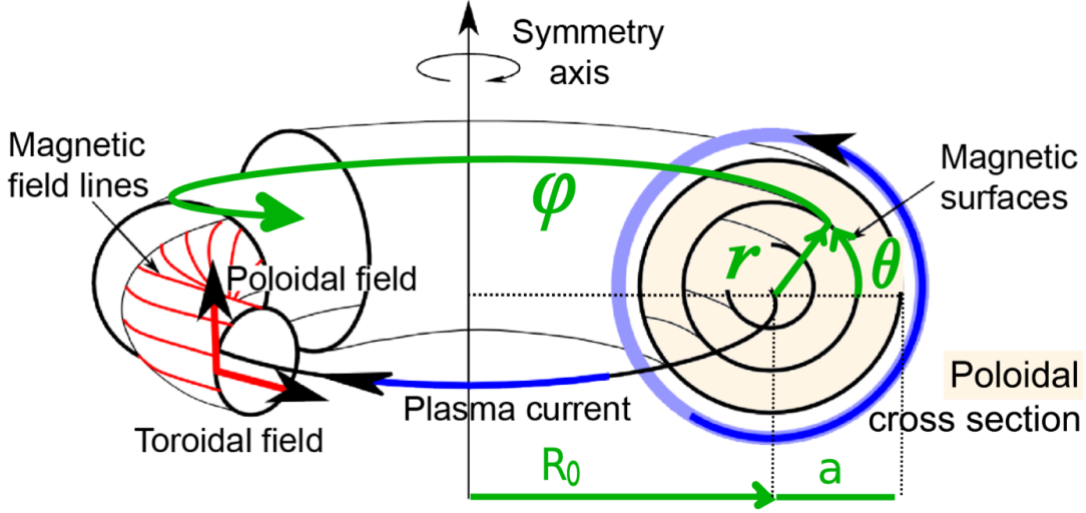


Figure 1.7 – Schematic of a circular concentric magnetic flux surfaces of a tokamak.

The helicity of magnetic field lines on a given flux surface is described by the so called *safety factor* $q(\psi)$, which gives the number of toroidal turns for each poloidal turn [12] and is defined as:

$$q(\psi) = \frac{1}{2\pi} \int_0^{2\pi} \frac{\mathbf{B} \cdot \nabla \varphi}{\mathbf{B} \cdot \nabla \theta} d\theta \quad (1.15)$$

where θ is the poloidal angle. The safety factor profile is closely related to the current profile which determines $B_\theta(\psi)$. For a large aspect-ratio tokamak of circular and concentric flux surfaces, the safety factor can be expressed as:

$$q(r) = \frac{r B_\varphi}{R_0 B_\theta} \quad (1.16)$$

For a rational value of the safety factor, $q = m/n$, with m and n being integers, the field lines are closed, and they return to their initial position after m toroidal and n poloidal rotations around the torus. These particular surfaces are called resonant or rational magnetic surfaces and play an essential role in determining the stability of the plasma. The radial derivative of the safety factor is described by the *magnetic shear* $\hat{s}(r) = (r/q)dq/dr$. For a typical plasma parameters $\hat{s} > 0$, with $q \sim 1$ in the plasma core and increases to $q \sim 3 - 5$ at the last closed flux surface.

Another important parameter that characterises the stability of magnetically confined plasmas is the β factor, defined as the ratio of the total kinetic (plasma) pressure to the magnetic pressure

$$\beta = \frac{\langle p \rangle}{B_0^2/2\mu_0}, \quad (1.17)$$

where $\langle p \rangle = \langle nT \rangle$ is the volume average plasma pressure, n and T being the plasma density and temperature, and B_0 is the toroidal magnetic field at the plasma centre. The typical values of plasma beta in a tokamak is only a few percent $\beta \sim 1 - 5\%$, though in spherical tokamaks it can exceed 30%. The maximum achievable beta in plasma is limited due to various MHD instabilities and technological constraints.

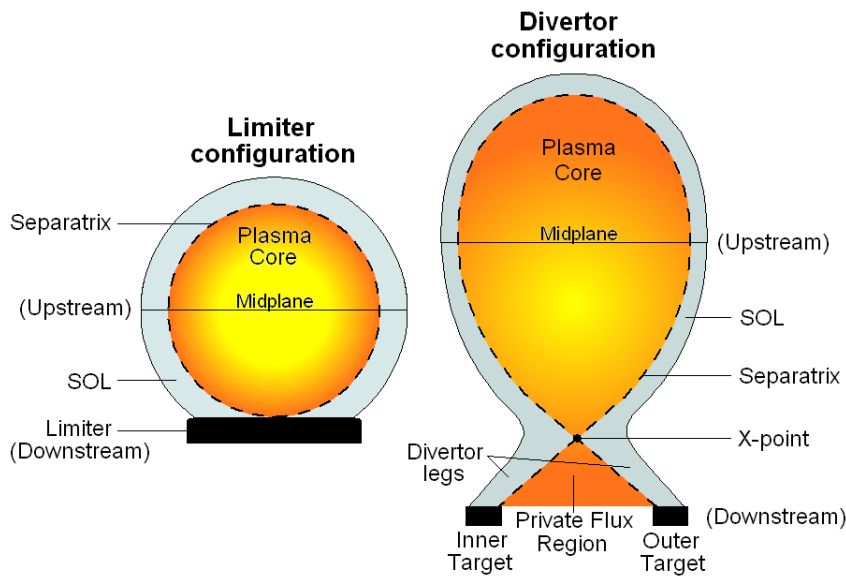


Figure 1.8 – Schematic view of poloidal cross-section of a tokamak with limiter and divertor geometries.

Two main types of flux surfaces geometries are used to separate the confined inner plasma region from the vacuum vessel wall of the tokamak: the limiter configuration and the divertor configuration as illustrated by figure 1.8. The separatrix separates the inner confined region from the region of open field lines. The plasma region outside the Last Closed Flux Surface (LCFS) and before the vessel wall is known as the Scrape-Off-Layer (SOL). In the limiter plasma configuration, the LCFS connects to the wall and therefore the plasma core is in direct exposure to the first wall. This leads to particle fluxes on the first wall that can damage the wall and generate impurities. These impurities can enter directly into the core and affect the fusion performance by fuel dilution and radiative cooling. This issue can be partially alleviated by the divertor configuration that allows the separation of the confined plasma from the main wall. In this configuration, the magnetic field structure is modified to form a null (or X -point) of the poloidal field in the plasma,

that improves the screening of the confined plasma from the vessel wall. The central region of fusion plasma reaches temperatures of several keV while the divertor plasma has lower temperatures (1–100eV). Thanks to the divertor configuration, the high core impurity contamination was reduced significantly, which allowed the tokamak operation to come back to metallic plasma-facing components. Existing fusion reactor designs are based on the divertor concept. The divertors of many operating tokamaks such as JET, ASDEX-Upgrade and WEST have replaced their carbon plasma-facing components by tungsten (W). W is chosen due to its high melting temperature, low erosion and low tritium retention.

As discussed earlier, a very high temperature is required for a fusion reaction to occur. Due to the finite plasma resistivity (η), the plasma current already provides Ohmic heating, $P_{OH} \propto \eta J^2$. However, the Ohmic heating is limited at a higher temperature because the plasma resistivity scales as $\eta \propto T_e^{-3/2}$, with T_e is the electron temperature. Therefore, several other auxiliary heating systems such as neutral beam injection (NBI) heating, electron cyclotron resonance heating (ECRH), ion cyclotron resonance heating (ICRH) and lower hybrid heating (LH) are employed to heat the plasma and achieve the desired fusion temperatures. NBI, LH, and ECRH can also be used to inject additional current.

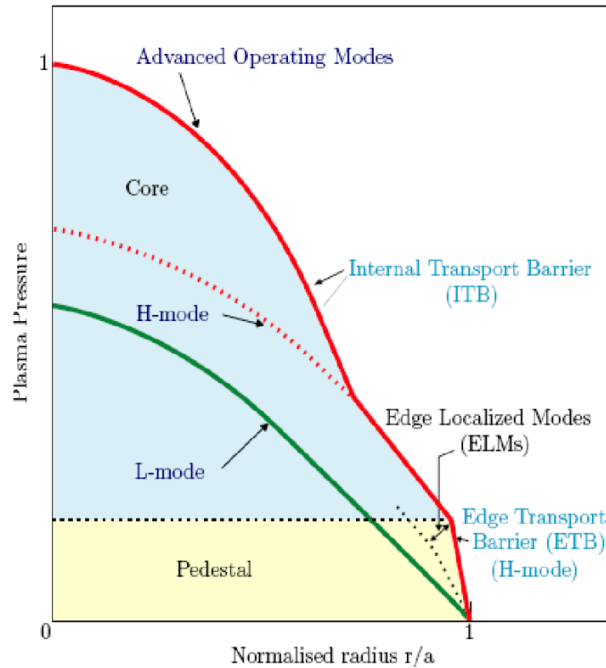


Figure 1.9 – Schematic diagram showing the formation of L and H modes plasma pressure with edge transport barrier [13].

The use of these auxiliary heating systems has made it possible to reach new plasma regimes. Above a certain threshold in the heating power, a transition to a high confinement configuration is reached, called the H-mode [14]. An edge transport barrier (ETB) is created due to a reduction in the turbulence level, decreasing the loss of particles and energy from the core, and thus steepening the gradients of density

and temperatures as seen in figure 1.9, called a pedestal [15]. The plasma pressure and energy confinement time are much higher in H-mode than in L-mode (L and H stand for low and high confinement regime, respectively). However, the formation of H-modes also leads to magnetohydrodynamics (MHD) instabilities called Edge Localised Modes (ELMs) [16]) that can release a significant amount of plasma energy in short bursts.

1.4.2 Transport in plasma: constraint to tokamak performance

The achievement of fusion requires good confinement, which is mainly limited by the cross-field transport of heat and particles from the system, as well as radiation. When there is no instability present in the system, the transport is described by neoclassical transport due to Coulomb collisions. However, experimentally the energy transport is higher than predicted by neoclassical theory. The excess of transport (also called anomalous) is due to turbulence caused by various instabilities present in the plasma.

In the plasma core, the energy, density and momentum follow local transport equations. The transport equation for particles and heat [17] are:

$$\frac{\partial n}{\partial t} + \nabla \cdot \mathbf{\Gamma} = S_{\Gamma}, \quad (1.18)$$

$$\frac{3nk_B}{2} \frac{\partial T}{\partial t} + \nabla \cdot \mathbf{Q} = S_Q, \quad (1.19)$$

where n is the particle density (m^{-3}), Γ the particle flux ($particles/m^2s$) and the particle source is S_{Γ} ($m^{-3}s^{-1}$), Q the heat flux ($W m^{-2}$) and S_Q is the heat source ($W m^{-3}$).

In equation 1.18, the particle flux is often decomposed as a sum of two contributions, one proportional to the density gradients and one proportional to the density itself:

$$\mathbf{\Gamma} = -D\nabla n + Vn \quad (1.20)$$

The diffusion and convection coefficients, $D = D_{neo} + D_{turb}$ and $V = V_{neo} + V_{turb}$, are composed of a neoclassical and turbulent parts. A brief overview of neoclassical and turbulent transport is provided below.

Neoclassical transport

Classical transport describes the collisional transport in cylindrical geometry. This description is not appropriate for describing particle trajectories in a toroidal geometry where some particles are trapped on the outboard due to the non-uniform magnetic field. The collisional transport in a toroidal geometry is known as neoclassical transport [17]. The neoclassical theory describes how energy, particle and momentum move within and across the flux surfaces due to Coulomb collisions and drifts between plasma species in a toroidal magnetic configuration.

To model neoclassical transport, there are several codes available such as NCLASS [18], NEO [19] with different level of complexity. NCLASS [18] is a multi-

species fluid code with a simplified collision operator and does not account for the effects of toroidal rotation. The Hirschman-Sigmar collision operator used in this code is based on pitch angle scattering. NEO [19] is a first-principle calculation based model, which solves the drift kinetic equation. More details about neoclassical transport can be found in Helander's book [20].

Turbulent transport

Turbulent transport results from small-scale fluctuations induced by various micro-instabilities in a tokamak. Instabilities are primarily driven by different free energy sources such as the gradient of density or temperature present in any confinement device [21]. When the phase difference between density and potential perturbations is finite, it leads to radial particle transport. The main plasma instabilities causing the turbulence transport in tokamaks are briefly reviewed in chapter 2. Understanding turbulence transport is considered as one of the most crucial issues in current devices as well as future fusion reactors such as in ITER. The understanding of turbulent transport in the central part of ITER plasmas close to the magnetic axis, $\rho < 0.3$ (where ρ is the normalised toroidal flux coordinate), is one of the main motivations of this thesis.

1.5 The choice of tungsten as a plasma-facing components

As discussed briefly in section 1.4, the first wall of magnetic confinement devices were initially made of high-Z materials in the limiter configuration. However, the significant radiation losses in the core induced by the impurity influx caused severe restrictions to plasma operation, and low-Z materials such as Carbon (C) replaced the metallic plasma-facing components. The use of these low-Z materials lead to an improved plasma performance by reducing central radiative losses. However, the use of low-Z materials has other serious issues such as large erosion rates due to low sputtering thresholds (figure 1.10), which limits the lifetime of the first wall materials. Carbon also has high tritium retention which is a problem for a tokamak operating with D-T, since tritium is radioactive and the amount of tritium circulating in a reactor is subject to strict regulations. The divertor configuration discussed earlier limits the erosion rate by allowing the plasma to be cooled down before reaching the target. Therefore, metallic materials became again a promising candidate for the walls. W is presently used as plasma-facing components in various tokamak devices such as JET (Joint European Torus) ITER-like wall [22], ASDEX Upgrade (AUG) [23] and in the ITER-like divertor of WEST [24]. The future fusion devices such as ITER will also use W as plasma-facing components for the divertor. In contrast, Beryllium will be used for the first wall because the heat fluxes on these areas are lower. W is considered as a promising material for ITER divertor because it has high melting temperatures ($\sim 3400^\circ\text{C}$) hence a capacity to sustain large heat loads, high sputtering threshold (see figure 1.10), low erosion rate and low tritium retention. The price to pay for these properties is that the issue of radiation power losses in the plasma core becomes crucial.

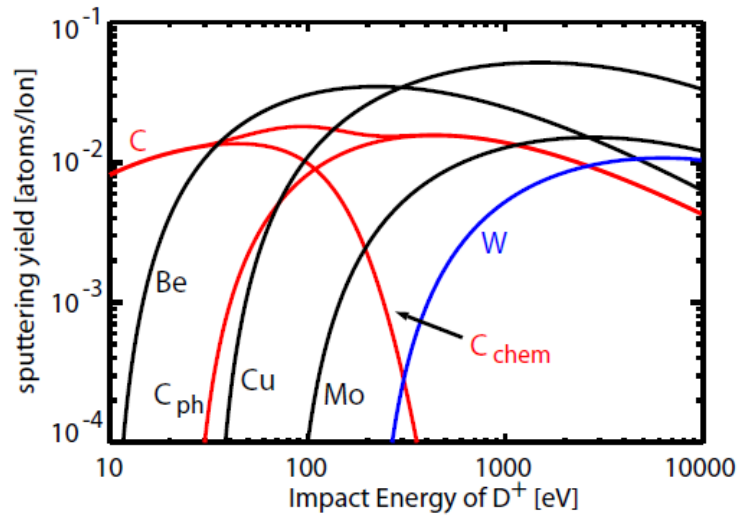


Figure 1.10 – Sputtering yield of various materials as function of incident energy of deuterium ions. Courtesy [25].

1.5.1 The W core accumulation issue: line radiation

Tungsten (W) is a heavy element with an atomic charge of $Z = 74$ and mass $A = 183.84$. W atoms are not fully ionised even at ITER fusion relevant temperatures. Partially ionised W radiates mainly through line emission and recombination, which depends on the electron and W density and is characterised by a cooling factor that is a function of the W charge state and electron temperature. The calculation of the cooling factor is based on the atomic data and the contribution of various radiative and collisional processes [26].

When the concentration of W exceeds a certain limit in the core of the plasma, radiative power losses cool down the plasma and the central plasma temperature drops, which limits the plasma operation and strongly reduces fusion performance. Figure 1.11 shows the impact of the W impurity concentration on the ignition conditions $n_e T \tau_E$ [26]. A black line shows the ideal burn condition with no fuel dilution and radiation due to impurities. The operation domain significantly reduces when the W concentration increases. It has been found that W develops very peaked core density profiles in some conditions in JET [27, 28] and ASDEX-Upgrade [29]. Luckily, it has been demonstrated that W accumulation in the central region can be controlled by large gas injection which decreases the temperature in the SOL and lowers W sputtering at the divertor and other methods such as core auxiliary heating with ICRH or ECRH [30]. In ITER, the accumulation of W has to be avoided to keep concentrations in the plasma core less than $n_W \sim 10^{-5} n_e$ and sustain high Q plasmas [30, 31]. The prediction and understanding of tungsten transport in the core of ITER plasmas is crucial and is the motivation of this thesis.

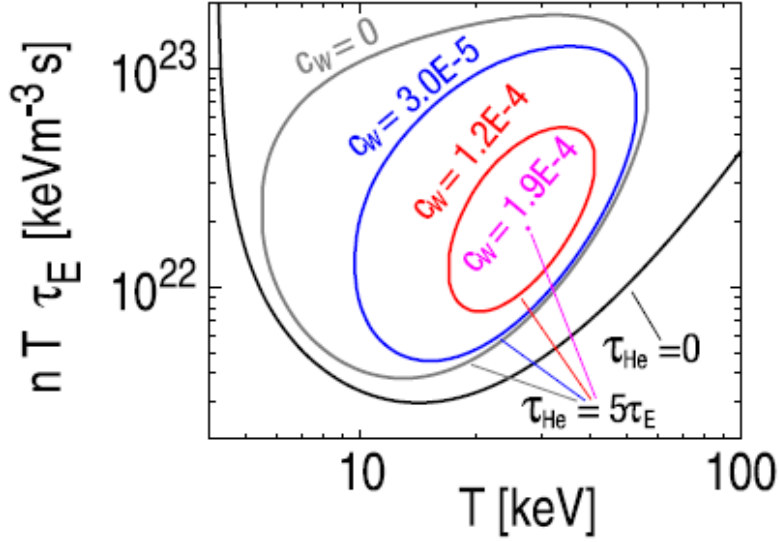


Figure 1.11 – Ignition curves as function of temperature for different concentrations of W for the case that $\tau_{He} = 5\tau_E$ along with the curve for no *He* and no *W*. Figure from reference [26].

1.5.2 Tungsten impurity transport

This section introduces the main characteristic of W transport. The transport of W impurity can be described by the continuity equation, Eq. 1.18. The particle flux in this equation can be computed by using fluid, drift-kinetic or gyrokinetic models describing neoclassical and turbulent transport.

Taking the volume integral of the continuity equation 1.18, the radial transport of impurity is described as:

$$\frac{\partial}{\partial t} \int n_W dV + V' \langle \Gamma \cdot \nabla \rho \rangle = \int S_W dV, \quad (1.21)$$

where $V' = \frac{\partial V}{\partial \rho}$, $\langle \cdot \rangle$ is the flux surface average defined as $\langle A \rangle = \frac{1}{V'} \int AdS \frac{dr}{|\nabla r|}$ (with dS the surface element) and V is the plasma volume enclosed by the flux surface at radial location ρ . The total impurity flux in equation 1.21 at a position ρ is the sum of neoclassical and turbulent contributions:

$$\Gamma_W^\rho = \langle \Gamma \cdot \nabla \rho \rangle = \Gamma_W^{neo} + \Gamma_W^{turb}, \quad (1.22)$$

From equation 1.20, these fluxes can be decomposed into diffusive and convective part:

$$\Gamma_W^\rho = -(D_{neo} + D_{turb}) \nabla n_W + (V_{neo} + V_{tur}) n_W, \quad (1.23)$$

with D the diffusion coefficient and V the pinch (convective) velocity. When W is in the Pfirsch-Schlüter regime and main ions are in the banana regime, one has

$$V_{neo} = Z D_{neo} \left[\left(-\frac{R}{L_{ni}} + 0.5 \frac{R}{L_{Ti}} \right) P_A^{model} - 0.33 P_B^{model} f_c \frac{R}{L_{Ti}} \right], \quad (1.24)$$

where two geometrical coefficients P_A^{model} and P_B^{model} are defined as

$$P_A^{model} = \frac{1}{2\varepsilon^2} \frac{\langle B^2 \rangle}{\langle n_W \rangle} \left[\frac{\langle n_W \rangle}{\langle B^2 \rangle} - \left\langle \frac{B^2}{n_W} \right\rangle^{-1} \right]$$

$$P_B^{model} = \frac{1}{2\varepsilon^2} \frac{\langle B^2 \rangle}{\langle n_W \rangle} \left[\frac{\langle n_W \rangle}{\langle B^2 \rangle} - \left\langle \frac{B^2}{n_W} \right\rangle^{-1} \right],$$

and other symbols have their usual meaning as defined in reference [32]. In the limit of no poloidal asymmetry, $P_A = 1$ and $P_B = 0$. A large diffusion tends to flatten the profile, while the pinch velocity tends to peak (if directed inward $V < 0$) or flatten the W profiles (if directed outward $V > 0$).

Several theoretical and experimental studies have been carried out to characterise the diffusive and convective parts of the impurity flux whether it is neoclassical or turbulent

The magnitude of neoclassical and turbulent W impurity transport is illustrated for a JET-ILW plasma in figure 1.12 taken from reference [32]. Here, the red curve shows the turbulent and blue the neoclassical contributions simulated using the GWK and NEO codes for a JET-ILW hybrid pulse. The full and open symbols show the curves respectively with and without poloidal asymmetry effects.

For the diffusive part, neoclassical transport dominates in the central region, whereas turbulent transport dominates in the outer half. The neoclassical transport dominates the convective part of the W transport. In addition, neoclassical convection changes sign in the inner core and at the edge (negative), which leads to inward convection of W. Therefore, to predict W transport, both turbulent and neoclassical transport need to be modelled.

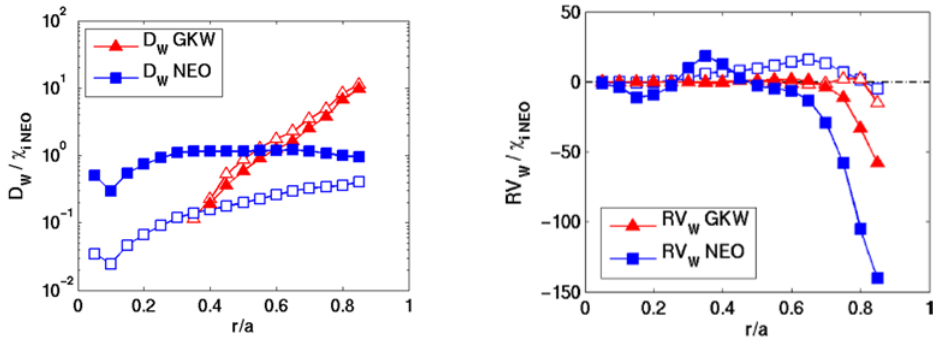


Figure 1.12 – Neoclassical (NEO) and turbulent (GWK) diffusion (left) and convective (right) contribution to W transport at 10.42 s for JET-ILW discharge 83351 [32].

1.6 Thesis Motivation

As discussed earlier, the understanding of impurity transport is crucial for the control of high-Z accumulation such as W in the inner core of present as well as future devices such as ITER. Present studies indicate that the transport of W in the central part of ITER is expected to be determined by neoclassical and turbulent processes, which strongly depend on the gradients of main ion density and temperature, as well as on rotation profiles (as discussed above in section 1.5.2). Therefore, the prediction of the transport processes that determine the density and temperature gradients of the main ions in the central core region of ITER plasmas is of crucial importance to determine the core behaviour of W in this region. Understanding of turbulent transport in the central part, $\rho < 0.3$, is crucial to this respect because this is the region where neoclassical transport becomes dominant and could lead to central W accumulation. Predicting core transport in the region $\rho < 0.3$ is also very important for the fusion reaction rate. It has, however, not been explored extensively so far, and previous studies mostly focused on the edge and core regions, $\rho > 0.3$.

In the very central region close to the magnetic axis, $\rho < 0.3$, gradients of density and temperature gets smaller and the level of turbulence may be reduced. In this region, some key questions are, is the plasma linearly unstable? If yes, is turbulent diffusion sufficient to offset the neoclassical pinch of W, up to which radius and how sensitive this is to the background gradients? An auxiliary question is whether the quasilinear (QL) approximation is valid in the inner core and up to which degree standard reduced quasilinear models such as QuaLiKiz (QuasiLinear gyroKinetic) [33] or TGLF (trapped gyro-Landau-fluid) [34] can be used in the central zone.

This thesis aims to answer these questions and to advance our understandings of the dominant transport mechanism in the very central region close to the magnetic axis by first validating the available transport models that are applied to ITER with measurements in existing tokamak plasmas and then apply these models to evaluate turbulent transport in ITER. The existing experimental JET high- β MHD-free hybrid H-mode discharge #75225 has been selected for the first objective to investigate the characteristics of core micro-instabilities and to test the quasilinear approximation in the inner core. These results are compared with the radial region, $\rho \sim 0.3$, where much of work has already been done previously [35, 36]. The MHD effects are not present in the selected hybrid (no sawteeth, $q_0 > 1$) discharge, though they can also be very important in this plasma region, particularly in normal (baseline) scenarios. MHD activity (sawteeth, saturated kink modes deforming the magnetic flux surfaces, or NTM) can also have a significant impact on the plasma behaviour in the central region [37, 38, 39].

1.7 Thesis Outline

The rest of the thesis is organised as follow. In chapter 2, various plasma instabilities, which are responsible for turbulent transport of energy and particles in a tokamak are introduced. The two main plasma approaches to describe these instabilities, the fluid and the kinetic ones are briefly described. An overview of the gyrokinetic

code GWK used to perform numerical simulations is presented in chapter 3. Here, the basic gyrokinetic equations solved by the code and normalisations of various parameters given as an input in the code are introduced.

Chapter 4 presents the linear simulation results of the JET hybrid H-mode plasma discharge 75225 inside $\rho = 0.3$. Dependencies of instabilities to various plasma parameters are investigated in the inner core of this selected discharge.

The non-linear simulation results are given in chapter 5. Here, a test of quasilinear approximation in the inner core region at $\rho = 0.15$ is presented. Various standard quasilinear models are tested against the non-linear results.

Finally, the conclusions and future perspectives of this thesis work are discussed in chapter 6.

2

Tokamak plasma instabilities

This chapter briefly describes the main plasma instabilities that can give rise to anomalous transport in a magnetically confined plasma. It focuses on the two main classes of instabilities: interchange and drift-waves, which include most of the instabilities found in tokamaks.

2.1 Overview of tokamak micro-turbulence

2.1.1 Particle motion and drift velocities in magnetised plasma

Cyclotron motion and guiding centre

The equation of motion of a charged particle "s" moving in an electric \mathbf{E} and magnetic \mathbf{B} field is:

$$m_s \frac{d\mathbf{v}_s}{dt} = e_s (\mathbf{E} + \mathbf{v}_s \times \mathbf{B}). \quad (2.1)$$

where m_s and e_s are respectively the mass and the charge of the particle "s", and v_s is its velocity.

For a homogeneous magnetic field directed in the z -direction and with zero electric field, the equation of motion becomes

$$\frac{d\mathbf{v}_s}{dt} = \frac{e_s B}{m_s} (\mathbf{v}_s \times \mathbf{b}), \quad (2.2)$$

with $\mathbf{b} = \mathbf{B}/B$.

The projection of equation 2.2 on (x,y,z) coordinates leads to:

$$\frac{dv_x}{dt} = \omega_{c,s} v_y, \quad \frac{dv_y}{dt} = -\omega_{c,s} v_x, \quad \frac{dv_z}{dt} = 0. \quad (2.3)$$

The solution of the above equations describes a circular orbital motion around the magnetic field lines with angular frequency ω_c . This motion is called Larmor motion. The angular frequency $\omega_{c,s} = e_s B / m_s$ is called cyclotron (angular) frequency. The typical cyclotron frequency for a Deuterium in a magnetic field of $B = 5$ T is about 7.5 MHz.

Solving further above equations 2.3 by simple substitutions and separation of variable and using $v_x = dx/dt$ and $v_y = dy/dt$, the solution in x and y directions becomes:

$$x = -\rho_s \cos(\omega_{c,s}t), \quad y = \rho_s \sin(\omega_{c,s}t) \quad (2.4)$$

where $\rho_s = \frac{m_s v_{\perp s}}{e_s B}$ is called the Larmor radius, and the center of gyration of the particle (Larmor motion) is called the guiding-center. For a Deuterium with $B = 5$ T and $v_{\perp} = 7 \times 10^5$ m/s, the Larmor radius is around 2.5 mm.

Drift of guiding centre

The dynamics of charged particles in a non-uniform magnetic field lead to drifts of the guiding centre. Details about particle trajectories and these drifts can be found in any standard plasma textbook such as [2, 12, 40], so it will not be discussed here. We simply remind the evolution of the guiding center given by:

$$\frac{d\mathbf{v}_G}{dt} = e(\mathbf{E} + \mathbf{v}_G \times \mathbf{B}) - \mu \nabla B. \quad (2.5)$$

with \mathbf{v}_G the drift velocity of guiding centre.

Solving equation 2.5 in the parallel and transverse directions gives the drift velocities of the guiding center:

- ◇ The $\mathbf{E} \times \mathbf{B}$ drift velocity due to the presence of an electric field

$$\mathbf{v}_{\mathbf{E} \times \mathbf{B}} = \frac{\mathbf{E} \times \mathbf{B}}{B^2} \quad (2.6)$$

- ◇ The ∇B drift due to gradients of the magnetic field

$$\mathbf{v}_{\nabla B} = \frac{\mu}{e} \frac{\mathbf{b} \times \nabla B}{B} \quad (2.7)$$

- ◇ The curvature drift due to the bending of magnetic field lines, which causes a centrifugal acceleration on individual particles as they follow the field lines

$$\mathbf{v}_c = \frac{mv_{\parallel}^2}{eB} \mathbf{b} \times (\mathbf{b} \cdot \nabla) \mathbf{b} \quad (2.8)$$

- ◇ The polarisation drift which is due to a time-varying electric field

$$\mathbf{v}_p = \frac{m}{eB^2} \frac{d\mathbf{E}_{\perp}}{dt} \quad (2.9)$$

These drifts govern the evolution of charged particles in an inhomogeneous electric and magnetic field.

In magnetised plasmas, the magnetic field generated by the gyro-motion of each charged particle is in the opposite direction to the external applied magnetic

field; therefore, the plasma is diamagnetic in nature. For each species, a collective fluid velocity results due to the presence of pressure gradients. It is called the diamagnetic velocity and defined as

$$\mathbf{v}_{dia} = \frac{\mathbf{B} \times \nabla p}{ZenB^2}. \quad (2.10)$$

The fluid motion in equilibrium for single plasma species plus stationary fields can be written as

$$\mathbf{v}_{fluid} = \mathbf{v}_{dia} + \mathbf{v}_E. \quad (2.11)$$

2.1.2 Drift wave and interchange instability

Drift waves become unstable in tokamaks due to the various guiding centre drifts discussed above. These waves propagate perpendicular to temperature and density gradients in the plasma. Only some fundamental properties of drift waves are introduced here; for a complete discussion see the reference [21].

Drift waves are the result of collective plasma oscillations that arise in magnetised plasmas when considering the dynamics of electron and ion motion separately. These independent dynamics are coupled through the electrostatic force, conspiring to ensure that plasma is always quasi-neutral. The frequencies of drift-waves are much smaller than the ion gyro-frequency. These modes are unstable at wavelengths of the order of the ion gyroradius. Finite gyroradius effects tend to stabilise the shorter wavelength.

The simplest picture of drift wave is obtained by assuming the ion fluid limit with an adiabatic electron response to the electrostatic potential fluctuations. Let's consider a homogeneous magnetic field in the Z -direction $\mathbf{B} = B\mathbf{e}_Z$, a wave vector of perturbation $\mathbf{k} = k\mathbf{e}_y$ and a radial density gradient with length scale L_n such that $\nabla n_0/n_0 = (-1/L_n)\mathbf{e}_x$. The electron and ion temperature are assumed to be equal and uniform $T_e \approx T_i$. The diamagnetic ion velocity is given by $\mathbf{v}_{dia,i} = (T_e/eBL_n)\mathbf{e}_y$. The continuity equation for ions is

$$\frac{\partial n_i}{\partial t} + \nabla \cdot (n_i \mathbf{v}_{fluid}) = 0, \quad (2.12)$$

with $\mathbf{v}_{fluid} = \mathbf{v}_{dia} + \mathbf{v}_E$ and $\nabla \cdot (n_i \mathbf{v}_{dia}) = 0$. Assuming a small density perturbation $n_i = n_0 + \delta n_i$ with $|\delta n_i| \ll n_0$, where n_0 is the equilibrium density and δn_i is a time dependent perturbed density written in the form

$$\delta n_i(\mathbf{x}, t) = n_{i0} \exp(i[\mathbf{k} \cdot \mathbf{x} - \bar{\omega}t]), \quad (2.13)$$

where $\bar{\omega}$ is the complex frequency $\bar{\omega} = \omega + i\gamma$. The $\mathbf{E} \times \mathbf{B}$ drift induced by the perturbed electrostatic potential $\delta\phi$ is written as

$$\delta \mathbf{v}_E = \frac{\mathbf{b} \times \nabla \delta\phi}{B} = -\frac{ik\delta\phi}{B} \mathbf{e}_x. \quad (2.14)$$

Linearizing the continuity equation ($\delta n_i \ll n_0$) gives

$$\frac{\partial \delta n_i}{\partial t} = \delta \mathbf{v}_E \cdot \nabla n_0. \quad (2.15)$$

where $\nabla \cdot \mathbf{v}_E = 0$ has been used.

Substituting Eq. 2.13 and 2.14, in Eq. 2.15 yields

$$-i\bar{\omega} \delta n_i = -\frac{ik\delta\phi}{B} \frac{n_0}{L_n}. \quad (2.16)$$

The parallel electron fluid force balance equation in the collisionless limit is

$$m_e n_e \frac{dv_{||,e}}{dt} = -\nabla_{||} p_e + en_e \nabla_{||} \delta\phi. \quad (2.17)$$

Here the dominant terms are the electric field $E_{||} = -\nabla_{||} \delta\phi$ and the pressure gradient $\nabla_{||} p_e = T_e \nabla_{||} n_e$. The thermal velocity of electrons is much higher than the ions and it can be assumed in the first approximation that the electrons respond to the potential fluctuations instantaneously. Neglecting the temperature fluctuations, the parallel force balance can be written as

$$\nabla_{||} p_e = en_e \nabla_{||} \delta\phi \quad \Rightarrow \quad T_e \nabla n_e = en_e \nabla \delta\phi, \quad (2.18)$$

which upon integration gives a linear Boltzmann relation for the electron response

$$n_e = n_0 \exp(e\delta\phi/T_e) \Rightarrow \delta n_e = n_0 [\exp(e\delta\phi/T_e) - 1], \quad (2.19)$$

where the condition $n_e = n_0$ when $\phi = 0$ was used. The adiabatic electron response follows as

$$\frac{\delta n_e}{n_0} = \frac{e\delta\phi}{T_e}. \quad (2.20)$$

Finally, imposing the quasineutrality condition $\delta n_i = \delta n_e$ and from equation (2.13), the frequency of the drift wave is

$$\bar{\omega} = \frac{kT_e}{eBL_n} = \omega^*. \quad (2.21)$$

This drift wave has a phase velocity $v_{ph} = v_{dia} = \omega^*/k$, which is equal to the diamagnetic velocity.

When the electron response is adiabatic (eq. 2.20), the electrostatic potential and the electron density fluctuations are in phase and perturbations propagate in phase. A simple description of this mechanism is presented in figure 2.1. An initial perturbation in density is associated with an initial perturbation in potential (adiabatic electron response). This generates a vertical electric field and causes a radial $\mathbf{E} \times \mathbf{B}$ drift of ions and electrons. The radial drift causes a denser plasma to move into the region of lower density and rarer plasma to higher density region. The

perturbation thus propagates upwards, in the electron magnetic direction. However, if there is a certain phase difference between the potential and density fluctuations, the electron response to potential perturbations can be written as $\delta n_e/n = (1 - i\delta)e\delta\phi/T_e$. The non-zero phase shift $i\delta$ causes the density to follow the potential maxima with a delay. When the phase shift is unfavourable, the radial component of the $\mathbf{E} \times \mathbf{B}$ drift results in a feedback loop which will bring higher density plasma into already denser plasma leading to an exponential growth $e^{\gamma t}$ of the initial perturbations driven by the free energy present in the density gradient. For a favourable phase shift, the initial perturbations will decay. Such a phase shift can occur in tokamak plasmas due to the non-adiabatic electron response and wave-particle kinetic resonances.

A coupling between density and temperature perturbations due to the magnetic drifts leads to another class of instabilities even if the potential and density perturbations are in phase. These instabilities are the pressure-driven interchange modes present in the core of tokamak plasmas. This kind of plasma instability is also called Rayleigh-Taylor instability, whose origin is analogous to hydrodynamics where a low-density fluid supports a dense fluid against gravity. These interchange instabilities tend to dominate the dissipative instabilities in the tokamak core, due to the low collisionality at hot temperatures. The origin of interchange instability in a tokamak is a combination of the inhomogeneity of the magnetic field (analogy with the gravity) and on departure from the thermodynamical equilibrium through the presence of large pressure gradients (analogy with the temperature gradient). An interchange mode is unstable only when the magnetic field inhomogeneity is unfavourable, i.e. ∇B , is aligned with the pressure gradient ∇p which is satisfied on the low-field side of the torus. The interchange modes are stable on the high-field side. The stability condition can be written as $\nabla p \cdot \nabla B > 0$.

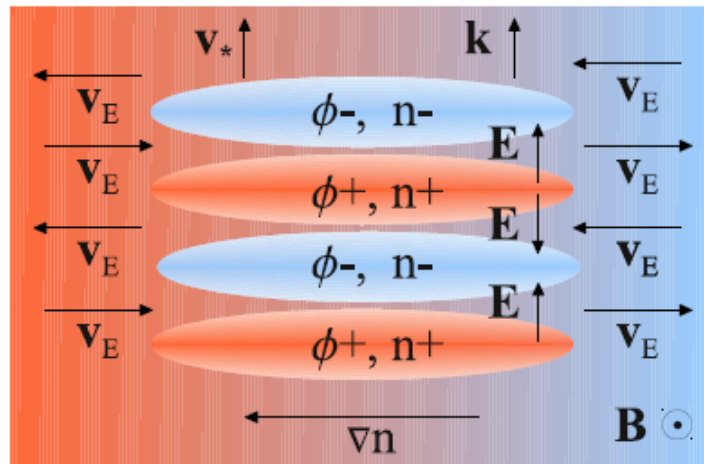


Figure 2.1 – Simplified picture of drift waves in a slab geometry with $k_x \ll k_y$. (Courtesy: [41])

2.1.3 Scale separation of instabilities

The main instabilities found in the core of tokamak plasmas, which are assumed to be responsible for the anomalous particles and energy transport, are now introduced.

The drift-wave and the interchange mechanism can describe most of these instabilities. The characteristics scale length of different tokamak instabilities in the order of increasing wave vector are given as trapped ion modes (TIM), ion temperature gradient (ITG), trapped electron modes (TEM) and electron temperature gradient (ETG) as illustrated in figure 2.2.

- ◇ ITG: ITG is an electrostatic instability destabilised due to finite ion temperature gradients in the system. ITG modes include two branches namely (1) slab branch [42, 43], when there is a resonance between the wave and parallel motion, and (2) toroidal branch [44, 45], when there is a resonance between the wave and the perpendicular magnetic drift. The characteristic wavelength of these modes is larger or comparable to the ion Larmor radius, such that $k_\theta \rho_i \leq 1.0$.
- ◇ TEM: an electrostatic mode driven by the resonance between the wave and the toroidal precession of trapped electrons. They can be excited by finite electron temperature gradients (∇T_e) and electron density gradients (∇n_e). Their characteristic wavelength limit is approximately $k_\theta \delta_{b,e} \leq 1.0$ [46, 47, 48]. Here $\delta_{b,e}$ is the typical banana orbit width of the trapped electrons and can be calculated from the conservation of the toroidal kinetic momentum and is given as $\delta_{b,s} \approx 2m_s R v_\varphi / (e_s R B_\theta)$, with v_φ the toroidal velocity. Using the definition of the safety factor from equation 1.16 and the Larmor radius $\rho_s = \frac{m_s v_\perp}{e_s B_\varphi}$ from equation 2.3, we get $\delta_{b,s} \approx \frac{2q}{\sqrt{r/R}} \rho_s$. The banana width is larger than the Larmor radius of the considered species.
- ◇ ETG: electrostatic electron modes similar to ion ones. These are again excited due to (∇T_e), however they have typical wavelengths of the order of electron scale rather than ions scale, i.e., $k_\theta \rho_e \leq 1.0$ [49, 50, 51].
- ◇ KBM: Kinetic Ballooning Mode is an electromagnetic interchange instability driven by the kinetic resonance between the wave and magnetic drift. The pressure gradient destabilises these modes in high- β plasmas [52, 53].

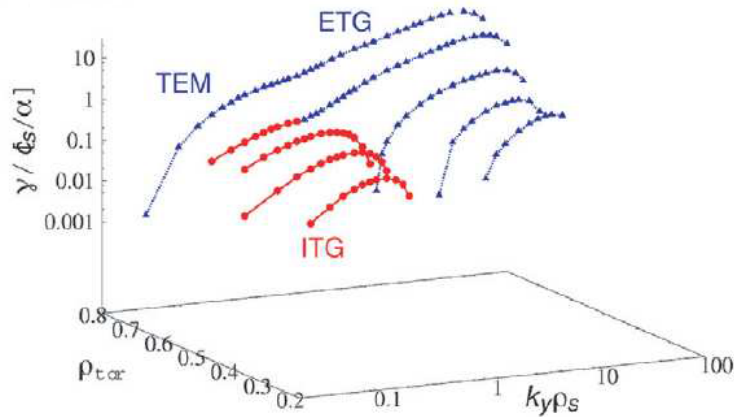


Figure 2.2 – A typical characteristics length scale of the linear growth rates for the ITG, TEM and ETG tokamak plasma instabilities. (Courtesy: [54]).

As seen in figure 2.2 several branches may coexist. In this thesis, the focus is on two dominant instabilities that are known to be crucial for determining transport in typical tokamak conditions: the ion temperature gradient (ITG) driven mode, and the kinetic ballooning modes (KBM). The ITG modes are the most widely known unstable modes found in typical tokamak conditions at low plasma β (figure 2.3), and their linear drive mechanisms are given in appendix A. However, the plasma core is characterised by a high plasma pressure hence higher β , which is favourable for the excitation of electromagnetic modes such as the kinetic ballooning modes (figure 2.3) which is discussed here. It should be noted that KBM is also destabilised in the pedestal and spherical tokamaks.

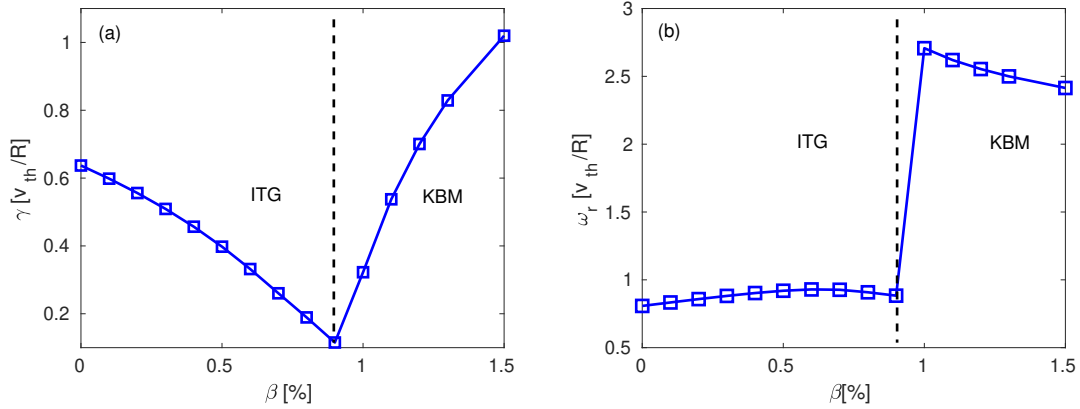


Figure 2.3 – A typical dependence of linear growth rates γ (a) and real frequency ω_r (b) on the plasma beta for a standard tokamak parameters: $k_{\theta}\rho_i = 0.4$, $\epsilon = 0.16$, $\hat{s} = 1.0$, $q = 2.0$, $R/L_{TD} = 9.0$, $R/L_{nD} = 3.0$, $R/L_{Te} = 0.0$, $R/L_{ne} = 3.0$, no collisions and no toroidal rotation.

2.1.3.1 Kinetic ballooning modes (KBMs)

The ballooning mode [55] is an electromagnetic instability driven primarily by the interaction of the plasma pressure gradient with local regions of unfavorable magnetic curvature making the plasma bulge out in these regions. The kinetic ballooning mode is considered as one of the most important instabilities present in the high confinement mode (H-mode) plasma discharges, which limits the maximum plasma pressure that can be sustained in a magnetic fusion device. Since it leads to a bending of the field lines, magnetic tension is stabilising and a minimum pressure gradient is required before the instability develops. Ballooning modes are high toroidal mode number perturbations in toroidal systems characterised by short-wavelength perpendicular to the magnetic field and long wavelengths parallel to field lines. The ballooning mode driving force is approximately given by the ballooning parameter, $\alpha = -2\mu_0(Rq^2/B^2)p'(r) = \beta q^2(R/L_p)$, with R , q , B , β , $p'(r)$ and R/L_p represent the major radius, safety factor, toroidal magnetic field, plasma beta, pressure gradient and its radial scale length, respectively. From this relation, it appears that the ballooning mode threshold in the pressure gradient can become very small when the q -value or the plasma β are high. The critical value of α can be calculated from ideal magnetohydrodynamics equations which are based on the assumptions that the

parallel electric field perturbations E_{\parallel} vanish. However, when kinetic effects such as magnetic drift, finite Larmor radius, wave-particle resonances, collisional effects and trapped particles are included, E_{\parallel} may become finite. In the presence of these kinetic effects, ballooning modes are known as Kinetic Ballooning Mode (KBM) [52, 53, 56]. KBM mode plays an important role in the stability and confinement of fusion plasmas and can cause cross-field transport of plasma. These modes are localised on the outboard side of the torus and rotate in the ion diamagnetic direction.

It should be noted that in the literature KBMs are also referred to as shear-Alfvénic ion temperature gradient modes (AITG) [57, 58] excited due to wave-particle interactions with thermal ions. Though, later considered as unstable branch connecting KBM [52, 53] and the Beta-induced Alfvén Eigenmode (BAE) [59, 60], both belong to the shear Alfvén branch. However, the general fish-bone-like dispersion relation (GFLDR-E) reveals that the most unstable AITG mode can be destabilized when the BAE and KBM branches are strongly coupled [59], this occurs when the condition $\Omega_{*pi} \equiv (\omega_{*pi}/\omega_{ti}) \sim \sqrt{(7/4 + \tau)q}$ is satisfied, where $\omega_{*pi} = (T_i/eB)k_{\theta}(\nabla \ln n_i)(1 + \eta_i)$ core plasma ion diamagnetic frequency, $\eta_i = \nabla \ln T_i / \nabla \ln n_i$, ω_{ti} is the thermal ion transit frequency defined as $\omega_{ti} = \sqrt{2T_i/m_i}/qR_0$ (T_i is the ion temperature in units of energy and m_i the ion mass) and $\tau = T_e/T_i$ [59]. Therefore KBM is unstable when the diamagnetic effects are dominant $\Omega_{*pi} \gg \sqrt{(7/4 + \tau)q}$ and BAE when ion compression effects are dominant $\Omega_{*pi} \ll \sqrt{(7/4 + \tau)q}$. These modes are destabilised by the thermal ion temperature gradient when the plasma β is above a certain threshold. The source of KBM instability is in the interchange drive term due to the combination of unfavorable magnetic curvature and pressure gradient. The threshold in β comes from the fact that at higher β the Alfvén speed $V_A = \omega_A q R$, with ω_A the Alfvén frequency and $V_A = \sqrt{B^2/\mu_0\rho_m}$ the Alfvén velocity where ρ_m is the mass density, decreases and the stabilising magnetic tension is reduced. The β threshold of KBM is generally smaller than the ideal MHD limit, $\beta_{crit} < \beta_{crit}^{MHD}$ [53, 61]. It has been shown that at higher β values, $\beta_{crit} > \beta_{crit}^{MHD}$, KBM can be driven unstable [62]. Here β_{crit} is the critical β limit for which Kinetic Ballooning Modes (KBM) are unstable and β_{crit}^{MHD} is the ideal MHD β limit.

The normalized parallel structure of the perturbed electrostatic potential (ϕ) and vector potential (A_{\parallel}) for ITG and KBM unstable modes and for standard tokamak parameters: $k_{\theta}\rho_i = 0.4$, $\epsilon = 0.16$, $\hat{s} = 1.0$, $q = 2.0$, $R/L_{TD} = 9.0$, $R/L_{nD} = 3.0$, $R/L_{Te} = 0.0$, $R/L_{ne} = 3.0$, no collisions and no toroidal rotation nor toroidal rotation gradient are given in figure 2.4 as a function of the parallel coordinate s . The perturbed fields $\delta\phi$ and δA_{\parallel} are normalised as follows: $\phi = \alpha_L \frac{e\delta\phi}{\rho_* T_i}$ and $A_{\parallel} = \alpha_L \frac{\delta A_{\parallel}}{\rho_*^2 B_{ref} R_0}$, with $\rho_* = \rho_i/R_0$ and α_L an additional normalising factor used in linear simulations to have $\text{Re}[\phi] = 1$ and $\text{Im}[\phi] = 0$ at the s position where $|\phi|$ is maximum. One poloidal turn corresponds to $\Delta s = 1$.

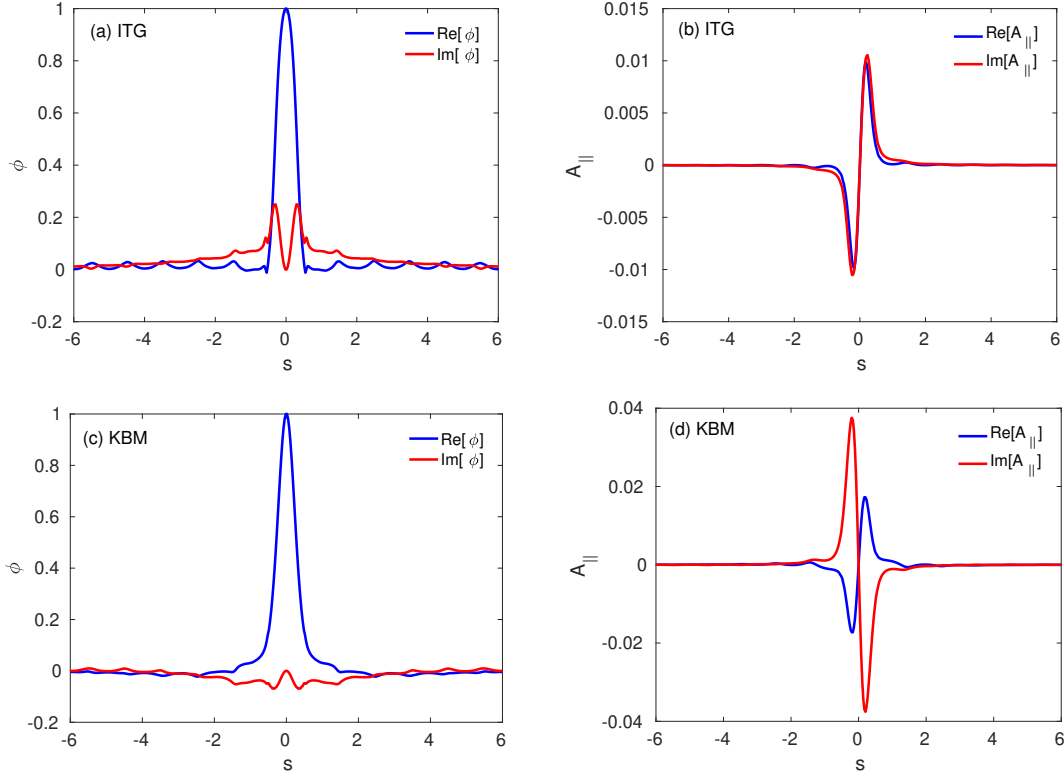


Figure 2.4 – Parallel mode structure of electrostatic potential ϕ and vector potential A_{\parallel} for ITG mode (a) and (b), and KBM modes (c) and (d) as a function of parallel coordinate s for standard tokamak parameters given in figure 2.3.

As illustrated in figure 2.3, when the β value increases, ion temperature gradient (ITG) modes are stabilised and above a threshold in beta KBMs become dominant. The frequency of KBMs is much higher than their ITG counterpart (Fig. 2.3 (b)). Both KBM and ITG modes are characterised by an even parity of electrostatic potential perturbation ϕ and odd parity of parallel vector potential perturbation A_{\parallel} along the magnetic field lines [63] as illustrated in figure 2.4 for a standard tokamak case.

2.2 Models for tokamak micro-turbulence

In the last section, basic mechanisms of various instabilities, which can give rise to anomalous transport of heat and particle in the tokamak core are presented. To formulate a transport model able to predict the turbulence level in plasmas, the dynamics of waves and particles need to be solved self-consistently. The generation of electromagnetic fields by charge and current particle densities is described by Maxwell equations. The dynamics of the plasma response to the fluctuations of electromagnetic potentials ϕ and A_{\parallel} can be described by a fluid or a kinetic description. Three approaches in the order of decreasing complexity can be distinguished as:

- ◊ **Particle description:** A direct approach where trajectory of each j single particle is governed by the equation of dynamics $m_j d\mathbf{v}_j/dt = q_j(\mathbf{E}_j + \mathbf{v}_j \times \mathbf{B}_j)$.

These equations are coupled through the field equations (Maxwell). The treatment of this kind of problem which is the origin of the Klimontovich and Liouville equation requires tracking the trajectories of $\sim 10^{23}$ particles, which appears far from being solvable for practical purposes and unnecessary.

- ◇ **Kinetic description:** A more reasonable way of describing the dynamics of this large number of charged particles consists in adopting a statistical approach where the time evolution of particles is described by a single distribution function (for each plasma species). The evolution of the distribution function is obtained by solving the Boltzmann's equation (or the Vlasov equation [64] if collisions are not retained) given as:

$$\frac{\partial f_s}{\partial t} + \mathbf{v} \cdot \frac{\partial f_s}{\partial \mathbf{x}} + \frac{q_s}{m_s} (\mathbf{E} + \mathbf{v} \times \mathbf{B}) \cdot \frac{\partial f_s}{\partial \mathbf{v}} = \mathcal{C}_s(f_s), \quad (2.22)$$

where $\mathcal{C}_s(f_s)$ is the collision operator, \mathbf{x} and \mathbf{v} are the position and the velocity respectively of the particles. Depending upon the choice of collision operator, the equation 2.22 is also referred to as the Fokker-Planck equation.

Here, the number of degree of freedom is 6: 3 in real space and 3 in velocity space per plasma species, namely electrons, main ions and impurities. Therefore, a full kinetic description of plasma is still numerically expensive. When the evolution of the magnetic field is smooth in space and time with respect to the fast cyclotron motion, the fast cyclotron timescale is removed by averaging over the gyro-motion. The phase space is reduced from 6 dimensions to 5 dimensions. This approach is called the gyro-kinetic theory [65, 66, 67, 68]. More details about the gyro-kinetic theory and the gyro-kinetic code used in this work is presented in chapter 3.

- ◇ **Fluid description:** The kinetic and in particular the gyrokinetic approximation have been quite successful in explaining the various experimental phenomenon in magnetic fusion plasmas and will be used extensively in this work. However, this approach is still cumbersome from the analytical as well as from the numerical point of view. This complexity has led to another major step in the simplification process by defining a fluid approach. In this approach, only the hierarchy of moments of the distribution function is considered, obtained by taking the different velocity integrals of f on the velocity basis $(1, v, v^2, \dots, v^n)$. This route is even more tractable from both the analytical and numerical point of view than the gyro-kinetic approach since the reduction of dimensional space is from $6D$ to $3D$ per species due to integration over velocity space dv^3 . Nonetheless, the fluid approach suffers from two critical drawbacks. It can hardly account for the interactions between waves and particles, as long as they are resonant in the velocity space due to velocity space integration. The linear Landau mechanism is the most relevant example of this issue. This is especially true for the hot thermonuclear plasmas, where collisions are infrequent. For the same reason, fluid equations have difficulties in differentiating between various classes of particles, namely passing, trapped and supra-thermal particles and to account for the finite Larmor radius effects. Furthermore, the infinite hierarchy

of fluid equations obtained by higher-order moments on the kinetic equations requires some closure assumption to truncate this. The closure of fluid problem remains an open issue in nearly collisionless plasmas, characterised by the larger mean free path and is still a subject of active research nowadays.

Despite these drawbacks, the fluid description remains of beneficial interest, especially near the colder tokamak edge which is more collisional.

2.3 Summary

Various class of instabilities found in tokamaks and their properties are introduced in this chapter with a focus on the ITG mode, unstable at low beta and the KBM mode which dominates at high beta. KBMs are electromagnetic instabilities driven by the pressure gradients that can drive a significant part of turbulent transport and can limit the maximum achievable plasma pressure in a tokamak.

3

Overview of the gyrokinetic code GKW

This chapter gives an overview of the gyro-kinetic code GKW used to perform numerical simulations in the present thesis. The basic gyrokinetic equations solved by the code and their ordering is presented. A description of the coordinate system and the definition of various input parameters and their normalisation are given. Additional details about the code can be found in the original paper [69] as well as in the GKW manual [70]. All the material presented in this chapter is summarised from ref. [69], and discussed here to introduce the input parameters used later in chapter 4.

3.1 Gyrokinetic orderings

Gyro-Kinetic Workshop (GKW) [69] is a nonlinear gyro-kinetic flux tube code used to study micro-instabilities and turbulent transport in tokamak plasmas. It solves the gyro-kinetic (GK) Boltzmann equation coupled to Maxwell's equations (Poisson's and Ampere's equations) in the 5-dimensional space. It uses a combination of finite difference and pseudo-spectral methods with explicit time integration to solve the equations.

The gyrokinetic theory in magnetised plasma exploits the temporal scale separation between the fast gyromotion and the slow drift frequency, $\omega \sim \omega_d \sim \omega^*$ (see equation 2.21) of the wave destabilized in the plasma:

$$\frac{\omega}{\omega_c} \sim \epsilon \ll 1. \quad (3.1)$$

where $\omega_c = eB/m$ is the cyclotron frequency (equation 2.3).

The typical length scale over which the solution varies in the direction perpendicular to the magnetic field is assumed to be of the order of the small parameter $\rho^* = \rho_i/R$ ($\rho_i = m_i v_{thi}/(eB)$ being the ion Larmor radius and R the major radius of the device, see figure 1.7). Along the magnetic field, the solution is assumed to have a length scale of the order of the machine size due to the fast streaming motion of particles, giving the following relations:

$$R\nabla_{\parallel} \approx 1, \quad (3.2)$$

$$R\nabla_{\perp} \approx 1/\rho^*. \quad (3.3)$$

These basic orderings (ω/ω_c and ρ^*) are the origin of the formulation of gyrokinetic theory in ref. [65, 67, 68].

Finally, a δf approximation is employed in GKW, which assumes that the fluctuation of the perturbed distribution function (f) is small in comparison to the equilibrium distribution function F .

$$\frac{f}{F} \sim \rho^*. \quad (3.4)$$

The background quantities are also assumed to have slow spatial variations. As a result, the turbulence can be considered as homogeneous in the perpendicular plane. This approximation is known as the local approximation and has a particular interest since it allows a Fourier decomposition to apply and the simulation domain to be restricted to a flux-tube aligned with magnetic field lines. GKW uses this local limit in which only a small region is simulated, and the background quantities and their gradients are constant across this domain. Unless otherwise stated, the local version of GKW has been used in all the simulations presented in this thesis; however, a global GKW version is also available [69, 70].

3.2 Gyrokinetic equation solved in GKW

In GKW, the evolution of the perturbed gyrocenter distribution function f is solved in the gyro-centre coordinates $(\mathbf{X}, \mu, v_{\parallel})$ along with the perturbed electrostatic potential ϕ and perturbed vector potential A . Here \mathbf{X} is the gyro-centre position, v_{\parallel} the parallel velocity along the magnetic field, and μ the magnetic moment $\mu = mv_{\perp}^2/2B$. The equations are formulated in the co-moving frame by assuming rigid body rotation in the toroidal direction and includes inertial effects (centrifugal and Coriolis forces).

The time evolution of the total gyro-centre distribution function $f_{tot} = F + f$ in the gyro-centre coordinates is written as:

$$\frac{\partial f_{tot}}{\partial t} + \frac{d\mathbf{X}}{dt} \cdot \frac{\partial f_{tot}}{\partial \mathbf{X}} - \frac{dv_{\parallel}}{dt} \frac{\partial f_{tot}}{\partial v_{\parallel}} = 0. \quad (3.5)$$

The evolution equations for the gyro-centre position \mathbf{X} and for the parallel velocity are:

$$\frac{\partial \mathbf{X}}{\partial t} = v_{\parallel} \mathbf{b} + \mathbf{v}_D + \mathbf{v}_{\chi}, \quad (3.6)$$

$$mv_{\parallel} \frac{dv_{\parallel}}{dt} = \frac{\partial \mathbf{X}}{\partial t} \cdot [Ze\mathbf{E} - \mu \nabla B - m\Omega^2 R \nabla R], \quad (3.7)$$

where Ω is the toroidal rotation frequency of the moving frame in which equations are formulated, and \mathbf{b} is the unit vector in the parallel magnetic field direction. \mathbf{E} is the gyro-averaged perturbed electric field given as:

$$\mathbf{E} = \nabla \langle \phi \rangle_{gy} - \frac{\partial \langle A_{\parallel} \rangle_{gy}}{\partial t} \mathbf{b} - \nabla \Phi, \quad (3.8)$$

where Φ is the equilibrium (background) electrostatic potential and brackets $\langle \dots \rangle_{gy}$ represent the gyro-average.

The velocities defined in equation 3.6 are as follows: $v_{\parallel} \mathbf{b}$ the parallel motion along the unperturbed magnetic field, \mathbf{v}_D the drifts due to inhomogeneous magnetic field (curvature (see equation 2.8), ∇B (equation 2.7), centrifugal and Coriolis drifts):

$$\mathbf{v}_D = \frac{1}{Ze} \left[\frac{mv_{\parallel}^2}{B} + \mu \right] \frac{\mathbf{B} \times \nabla B}{B^2} + \frac{mv_{\parallel}^2}{2ZeB} \beta' \mathbf{b} \times \nabla \varepsilon + \frac{2mv_{\parallel}}{ZeB} \Omega_{\perp} + \frac{1}{ZeB} \mathbf{b} \times \nabla \xi. \quad (3.9)$$

Where the centrifugal energy ξ is defined from the background electrostatic potential and the centrifugal drift as:

$$\xi = Ze\Phi - \frac{1}{2} m\Omega^2 (R^2 - R_0^2). \quad (3.10)$$

Here $\varepsilon = r/R_0$ is the normalized radial coordinate (flux label), $\Omega_{\perp} = \Omega - (\Omega \cdot \mathbf{b}) \mathbf{b}$ is the angular (toroidal) rotation vector perpendicular to the magnetic field, and $\beta' = \frac{2\mu_0}{B^2} \frac{\partial p}{\partial \varepsilon}$. In equation 3.9, the first term on the right-hand side corresponds to the combination of ∇B and curvature drifts, the second term is the correction to the curvature drift due to modification of the equilibrium associated with the pressure gradient. The last two terms are the Coriolis drift [71] and the combination of the background potential and the centrifugal drift [72, 41].

The drift \mathbf{v}_{χ} is a sum of the $\mathbf{E} \times \mathbf{B}$ drift ($\mathbf{v}_E = \mathbf{b} \times \nabla \langle \phi \rangle_{gy} / B$) and of the parallel motion along the perturbed field lines ($\mathbf{v}_{\delta B} = -\mathbf{b} \times \nabla v_{\parallel} \langle A_{\parallel} \rangle_{gy} / B$), i.e. :

$$\mathbf{v}_{\chi} = \frac{\mathbf{b} \times \nabla \chi}{B} \quad \text{with} \quad \chi = \langle \phi \rangle_{gy} - v_{\parallel} \langle A_{\parallel} \rangle_{gy} + \frac{\mu}{Ze} \langle B_{\parallel} \rangle_{gy}. \quad (3.11)$$

The total distribution function f_{tot} is split into a slowly varying (in time and space) background part F and fast varying perturbed part f , $f_{tot} = F + f$. Employing the δf approximation and using equations 3.6 and 3.2, the general evolution equation

for f solved in GKW from 3.5 is written as:

$$\frac{\partial f}{\partial t} + (v_{\parallel} \mathbf{b} + \mathbf{v}_D + \mathbf{v}_\chi) \cdot \nabla f - \frac{\mathbf{b}}{m} \cdot (\mu \nabla B + \nabla \xi_\Omega) \frac{\partial f}{\partial v_{\parallel}} = S, \quad (3.12)$$

where S is described by the background distribution function F :

$$S = -(\mathbf{v}_\chi + \mathbf{v}_D) \cdot \nabla F - \frac{Ze}{T} [v_{\parallel} \mathbf{b} + \mathbf{v}_D] \cdot \nabla \langle \phi \rangle_{gy} F, \quad (3.13)$$

where R_0 is the reference major radius of the flux surface at which the densities of the background Maxwellian is defined.

The background Maxwellian distribution function (F_M) is defined as:

$$F = F_M = \frac{n_0}{\pi^{3/2} v_{th}^3} \exp \left[-\frac{(v_{\parallel} - (RB_t/B)\omega_\phi)^2 + 2\mu B/m}{v_{th}^2} - \xi/T \right], \quad (3.14)$$

with $v_{th} = \sqrt{2T/m}$ being the thermal velocity of the considered species, ω_ϕ is the plasma toroidal rotation frequency in the rotating frame. The plasma rotation ω_ϕ by definition zero in the rotating frame, but it has a radial gradient.

Finally, to form a closed set of equations, the gyrokinetic equations need to be combined with the field equations. The fields ϕ , A_{\parallel} and B_{\parallel} are obtained by solving the Poisson equation and the Ampere's law. In GKW units the gyrokinetic Poisson equation is written as:

$$\sum_{sp} Z_{sp} n_{R_0, sp} \left[2\pi B \int dv_{\parallel} d\mu J_0(k_{\perp} \rho_{sp}) \hat{g}_{sp} + \frac{Z_{sp}}{T_{R, sp}} [\Gamma(b_{sp}) - 1] \hat{\phi} \right] = 0, \quad (3.15)$$

where

$$b = \frac{1}{2} m_R T_R (k_{\perp} \rho^* R_{ref} / Z B^2)^2 = \frac{\overbrace{1 k_{\perp}^2 m^2 v_{th}^2}^{\text{in original units}}}{2 e^2 B^2}. \quad (3.16)$$

On the left-hand side of the above equation, the sum is over the plasma species and the integral over velocity space. Here a $\hat{\cdot}$ represents the Fourier representation of a quantity.

The vector potential is calculated from the Ampere's law as:

$$\left(k_{\perp}^2 + \beta \sum_{sp} \frac{Z_{sp}^2 n_{R_0, sp}}{m_{R, sp}} \Gamma(b_{sp}) \right) = \beta \sum_{sp} Z_{sp} v_{R, sp} n_{R_0, sp} \times 2\pi B \int dv_{\parallel} \int d\mu v_{\parallel} J_0 \hat{g}_{sp}. \quad (3.17)$$

Here g is a new distribution function defined as

$$g = f + \frac{Ze}{T} v_{\parallel} \langle A_{\parallel} \rangle_{gy} F_M \quad (3.18)$$

By solving for this new distribution function, the time derivative of the vector potential appearing in the parallel acceleration and presenting a numerical difficulty is avoided.

3.3 Normalisations in GWK

All quantities used in GWK are normalised using a reference quantity. The important parameters used in this thesis and their respective normalisations are presented in this section. First, the reference values are defined such as a reference mass m_{ref} , a reference density n_{ref} , a reference temperature T_{ref} , a reference thermal velocity v_{thref} , a reference major radius R_{ref} , a reference vacuum magnetic field B_{ref} and a reference gyroradius ρ_{ref} . The reference magnetic field is defined as $B_{ref} = B_t(R_{ref})$ on the considered flux surface when the Miller parametrisation is used.

The reference quantities are related to each other:

$$T_{ref} = \frac{1}{2} m_{ref} v_{thref}^2, \quad (3.19)$$

$$\rho_{ref} = \frac{m_{ref} v_{thref}}{e B_{ref}}. \quad (3.20)$$

These reference values are used to define dimensionless quantities such as mass m_N , density n_N , temperature T_N , magnetic field B_N , major radius R_N , and time t_N as:

$$m_N = \frac{m}{m_{ref}}, \quad n_N = \frac{n_{R_{ref}}}{n_{ref}}, \quad (3.21)$$

$$T_N = \frac{T}{T_{ref}}, \quad B_N = \frac{B}{B_{ref}}, \quad (3.22)$$

$$R_N = \frac{R}{R_{ref}}, \quad t_N = \frac{t v_{thref}}{R_{ref}}. \quad (3.23)$$

where the subscript N denotes a normalised quantity. The velocity space coordinates are normalised using the thermal velocity of each species independently

$$v_{||} = v_{||N} v_{th}, \quad \mu = \frac{m v_{th}^2}{B_{ref}} \mu_N. \quad (3.24)$$

The normalised Larmor radius ρ^* and toroidal rotation velocity (indicated by u in the following chapters) are given as:

$$\rho^* = \rho_{ref} / R_{ref} \quad (3.25)$$

$$u = R_{ref} \Omega / v_{thref} \quad (3.26)$$

with $u > 0$ for a plasma flowing in the direction of \mathbf{B} . The normalised gradients for density, temperature and toroidal rotation are defined in the following ways:

$$\frac{1}{L_{n,N}} = \frac{R_{ref}}{L_n} = -\frac{R_{ref}}{n} \frac{\partial n}{\partial r}, \quad (3.27)$$

$$\frac{1}{L_{T,N}} = \frac{R_{ref}}{L_T} = -\frac{R_{ref}}{T} \frac{\partial T}{\partial r}, \quad (3.28)$$

$$u'_N = \frac{R_{ref}^2}{v_{thref}} \frac{\partial \omega_\phi}{\partial r}. \quad (3.29)$$

It should be noted that these normalized gradients lengths are denoted by R/L_n , R/L_T and u' in the thesis and they are normalized with R_{ref} . The normalized radial coordinate ε is also normalized with R_{ref} :

$$\varepsilon = \frac{R_{max} - R_{min}}{2R_{ref}}, \quad (3.30)$$

where R_{max} and R_{min} are the maximum and minimum major radius of each flux surface, respectively.

The fields are normalised with the reference values

$$\phi = \rho^* \frac{T_{ref}}{e} \phi_N, \quad A_{||} = B_{ref} R_{ref} \rho_*^2 A_{||N}, \quad \chi = \rho_* \frac{T_{ref}}{e} \chi_N, \quad \Phi = \frac{T_{ref}}{e} \Phi_N. \quad (3.31)$$

It should be noted that a factor of ρ^* has been added in the above definitions of the normalised perturbed fields such that these normalised quantities are of order 1. The mode growth rates (γ) and real frequencies (ω_r) are normalized with v_{thref} and R_{ref} :

$$\gamma = \gamma_N v_{thref} / R_{ref}, \quad \omega_r = \omega_{rN} v_{thref} / R_{ref}. \quad (3.32)$$

Finally, the heat (Q_s), particle (Γ_s) and momentum (Π_s) fluxes in GWK are normalized as:

$$\Gamma_{N,s} = \frac{\Gamma_s R_{ref}}{n_{R_0,s} \rho_*^2 v_{thref}} \quad (3.33)$$

$$Q_{N,s} = \frac{Q_s R_{ref}}{n_{R_0,s} T_s \rho_*^2 v_{thref}} \quad (3.34)$$

$$\Pi_{N,s} = \frac{\Pi_s}{m_s n_{R_0,s} v_{th,s} \rho_*^2 v_{thref}} \quad (3.35)$$

These fluxes are the radial contravariant components of the flux.

In the rest of the thesis, parameters are presented in their normalised form and subscript N is dropped for simplicity. In the thesis, the deuterium ion mass is chosen as reference m_{ref} , the equilibrium electron density on the flux surface as n_{ref} , the ion temperature as T_{ref} , and reference major radius R_{ref} will be used as R_0 and is defined as $R_0 = 1/2(R_{max} + R_{min})$. $B_{ref} = B_t(R_0)$.

3.4 Geometry

Following the introduction of the basic equations solved in GKW and their normalisations, the geometry employed to solve these equations is described briefly in this section. A field-aligned coordinates system which follows the magnetic field lines is used to take advantage of the scale separation of the turbulent structures in the parallel and perpendicular directions ($k_{\parallel} < k_{\perp}$).

The main results are summarised as:

The coordinate system (ε, ζ, s) is used in GKW. Where ε is the radial coordinate, ζ the bi-normal coordinate and s is the parallel coordinate aligned with the magnetic field. The domain $[-1/2, 1/2]$ in s corresponds to one poloidal turn. The main properties and sign conventions in this coordinates system are:

- ◇ $\mathbf{B} \cdot \nabla \varepsilon = 0$ (flux surface definition)
- ◇ To make coordinates field aligned, $B^{\zeta} = 0$ and $B^{\varepsilon} = 0$
- ◇ The mode frequency is positive for a perturbation flowing in the direction opposite to $\nabla \zeta$, which corresponds to the ion ∇B drift direction if $s_j = 1$ and to the electron ∇B drift direction if $s_j = -1$.
- ◇ ε is always increasing from the plasma center to the plasma edge.
- ◇ s is increasing upwards from the low field side midplane.
- ◇ The toroidal rotation is assumed positive for a plasma flowing the direction of \mathbf{B}

3.4.1 Miller parameterisation

The calculation of the various drifts and metric terms in the gyrokinetic equation requires the magnetic field geometry to be specified. Different geometry models are implemented in GKW such as a simplified ' $s-\alpha'$ equilibrium [55], an improved circular equilibrium [73], Miller geometry [74] and coupling to a MHD equilibrium solver code CHEASE [75]. In the present thesis, the Miller flux surface parametrisation is used.

The Miller parameters used to describe a magnetic flux surface in the (R,Z) plane are: κ the elongation, δ the triangularity, ζ the squareness, R_{mil} and Z_{mil} the flux surface center and their radial derivatives s_{κ} , s_{δ} , s_{ζ} , R'_{mil} and Z'_{mil} [74].

The flux surfaces are defined as:

$$R = R_{mil} + r \cos(\theta + \arcsin \delta \sin \theta), \quad (3.36)$$

$$Z = Z_{mil} + r \kappa \sin(\theta + \zeta \sin 2\theta), \quad (3.37)$$

and

$$s_{\kappa} = \frac{r}{\kappa} \frac{d\kappa}{dr}, \quad s_{\delta} = \frac{r}{\sqrt{1-\delta^2}} \frac{d\delta}{dr}, \quad s_{\zeta} = r \frac{d\zeta}{dr}. \quad (3.38)$$

The radial derivative of the flux surface center major radius (R_{mil}) and elevation (Z_{mil}) are given as:

$$R'_{mil} = \frac{R_{mil}}{dr}, \quad Z'_{mil} = \frac{dZ_{mil}}{dr}. \quad (3.39)$$

The impact of these Miller parameters on the flux surfaces can be seen in figure 3.1.

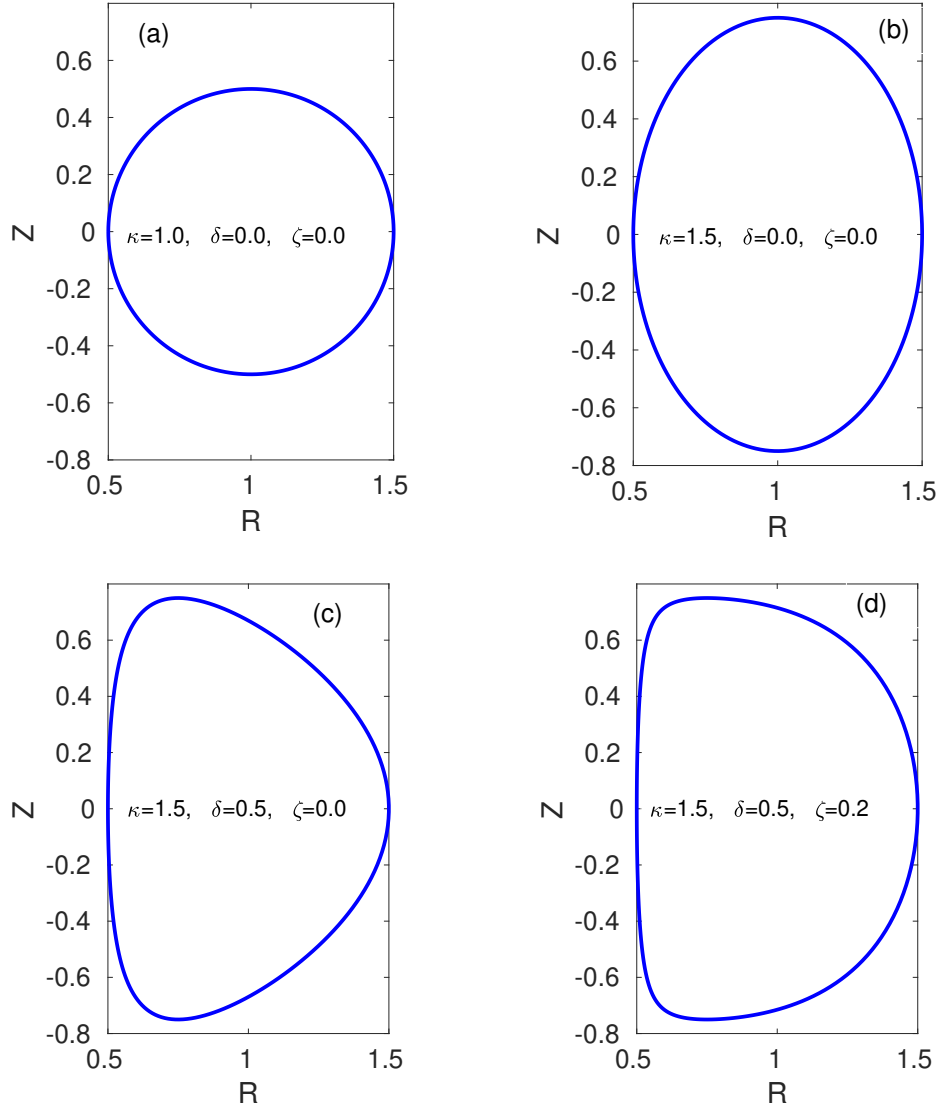


Figure 3.1 – Miller flux surfaces centred on $R_0 = R_{mil} = 1.0$ and $Z = 0$ plane with a minor radius of $r = 0.5$.

Additional parameters such as $\frac{dp}{d\varepsilon}$ (the pressure gradient), q (safety factor), \hat{s} (magnetic shear) and $\epsilon = \frac{r}{R_{mil}}$ (inverse aspect ratio) are also required to get a complete description of the equilibrium.

The radial derivative of the plasma pressure entering the Miller parametrisation is given by

$$\beta' = (2\mu_0 R_0 / B_{ref}^2)(dp/dr), \quad (3.40)$$

and the magnetic shear is defined as

$$\hat{s} = (r/q)dq/dr. \quad (3.41)$$

3.5 Spectral representation in GKW

A combination of finite difference techniques and pseudo-spectral methods is used in GKW to solve the equations. The turbulence is assumed homogeneous in the direction perpendicular to the magnetic field in the local limit, this allows periodic boundary conditions to be employed, and a sum over discrete Fourier modes can represent all perturbed quantities.

The Fourier decomposition in the perpendicular plane (ε, ζ) is written as:

$$f(\varepsilon, \zeta, s) = \sum_{k_\zeta, k_\varepsilon} \hat{f}(k_\varepsilon, k_\zeta, s) \exp[ik_\zeta \zeta / \rho_* + ik_\varepsilon \varepsilon / \rho_*]. \quad (3.42)$$

where a factor of ρ^* (normalised Larmor radius) has been added such that

$$\mathcal{T} \left(\rho_* \frac{\partial f}{\partial x_\alpha} \right) = ik_\alpha \hat{f}, \quad (3.43)$$

and is consistent with the normalisation discussed earlier.

Here a $\hat{\cdot}$ represents the Fourier representation of a quantity and \mathcal{T} indicate the respective forward discrete Fourier transform operations.

Another advantage of the Fourier representation is that gyro-average becomes an algebraic operation in Fourier space:

$$\langle \hat{\phi} \rangle_{gy} = J_0(k_\perp \rho) \hat{\phi} \quad (3.44)$$

with J_0 being the Bessel function.

The condition of toroidal periodicity implies

$$f(\varepsilon, \zeta + 1, s) = f(\varepsilon, \zeta, s) \quad \Rightarrow \quad \frac{k_\zeta}{2\pi\rho^*} = N, \quad (3.45)$$

with N an integer. Because ρ^* is small, the above condition is satisfied for a minimal change to k_ζ or ρ^* , which is equivalent to the condition that the toroidal mode number is large enough. In the local limit, the final equations obtained are independent of ρ^* , and it is considered that the above relation is satisfied. The poloidal periodicity implies:

$$f(\varepsilon, \zeta + q/2, 1/2) = f(\varepsilon, \zeta - q/2, -1/2), \quad (3.46)$$

which translates to Fourier spaces as

$$\sum_k \hat{f}(k_\varepsilon, k_\zeta, 1/2) \exp \left[\frac{ik_\zeta}{\rho^*} + \frac{ik_\varepsilon \varepsilon}{\rho^*} + \frac{iqk_\zeta}{2\rho^*} \right] \quad (3.47)$$

$$= \sum_k \hat{f}(k_\varepsilon, k_\zeta, -1/2) \exp \left[\frac{ik_\zeta}{\rho^*} + \frac{ik_\varepsilon \varepsilon}{\rho^*} - \frac{iqk_\zeta}{2\rho^*} \right]. \quad (3.48)$$

Expanding the safety factor around a reference value q_R (the value at the centre of the radial domain)

$$\frac{qk_\zeta}{\rho^*} = \frac{q_R k_\zeta}{\rho^*} + k_\zeta \frac{\partial q}{\partial \varepsilon} \frac{\varepsilon}{\rho^*} + \frac{1}{2} k_\zeta \rho^* \frac{\partial^2 q}{\partial \varepsilon^2} \left(\frac{\varepsilon}{\rho^*} \right)^2, \quad (3.49)$$

and neglecting the second derivative correction, this condition is satisfied when $q_R k_\zeta / 2\pi \rho^*$ is an integer, and if

$$\hat{f} \left(k_\varepsilon, k_\zeta, \frac{1}{2} \right) = \hat{f} \left(k_\varepsilon + k_\zeta \frac{\partial q}{\partial \varepsilon}, k_\zeta, -\frac{1}{2} \right), \quad (3.50)$$

which connects a mode to the appropriate higher k_ε mode at the boundary of the s domain. Thus, increasing the length of the field line simulated is equivalent to increasing the number of k_ε modes. This formulation is close to the ballooning representation [76].

This boundary condition for the Fourier amplitudes implies that a convenient option for the spacing of the k_ε modes in the discrete Fourier representation is

$$\Delta k_\varepsilon = k_{\zeta, \min} \frac{\partial q}{\partial \varepsilon} \frac{1}{i_k}, \quad (3.51)$$

with i_k some integer. The i_k allows control over the radial resolution by changing the spacing between the radial modes.

The normalised wave number $k_{\theta \rho_{ref}}$ is given as an input in the simulations performed throughout this thesis, whereas k_ζ is effectively used in the code. The link between the two wave numbers is given by:

$$(k_{\theta \rho_{ref}})^2 = g^{\zeta \zeta} k_\zeta^2, \quad (3.52)$$

with $g^{\zeta \zeta}$ is a contravariant metric tensor element evaluated at the low field side midplane ($s = 0$) to determine k_ζ from the value of $k_{\theta \rho_i}$ provided in input. The two-poloidal wave numbers are related to the toroidal mode number n by:

$$n = \frac{k_{\theta \rho_{ref}}}{2\pi \rho^* \sqrt{g^{\zeta \zeta}|_{s=0}}} = \frac{k_\zeta}{2\pi \rho^*}. \quad (3.53)$$

The complete perpendicular wave vector which will be used later in chapter 5 for the quasilinear approximation is given by

$$k_{\perp}^2 = g^{\varepsilon\varepsilon} k_{\varepsilon}^2 + 2g^{\varepsilon\zeta} k_{\varepsilon} k_{\zeta} + g^{\zeta\zeta} k_{\zeta}^2. \quad (3.54)$$

The flux surface average particle, heat and angular momentum fluxes are given by the equations:

$$\langle \Gamma \cdot \nabla \varepsilon \rangle_s = \left\langle \int \mathbf{v}_E \cdot \nabla \varepsilon f d^3 v \right\rangle_s + \left\langle \int \mathbf{v}_{A_{\parallel}} \cdot \nabla \varepsilon f d^3 v \right\rangle_s + \left\langle \int \mathbf{v}_{B_{\parallel}} \cdot \nabla \varepsilon f d^3 v \right\rangle_s, \quad (3.55)$$

$$\langle Q \cdot \nabla \varepsilon \rangle_s = \left\langle \int \frac{v^2}{2} \mathbf{v}_E \cdot \nabla \varepsilon f d^3 v \right\rangle_s + \left\langle \int \frac{v^2}{2} \mathbf{v}_{A_{\parallel}} \cdot \nabla \varepsilon f d^3 v \right\rangle_s + \left\langle \int \frac{v^2}{2} \mathbf{v}_{B_{\parallel}} \cdot \nabla \varepsilon f d^3 v \right\rangle_s, \quad (3.56)$$

$$\langle \Pi \cdot \nabla \varepsilon \rangle_s = \left\langle \int m v_{\parallel} \mathbf{v}_E \cdot \nabla \varepsilon f d^3 v \right\rangle_s + \left\langle \int m v_{\parallel} \mathbf{v}_{A_{\parallel}} \cdot \nabla \varepsilon f d^3 v \right\rangle_s + \left\langle \int m v_{\parallel} \mathbf{v}_{B_{\parallel}} \cdot \nabla \varepsilon f d^3 v \right\rangle_s. \quad (3.57)$$

These fluxes are the sums of the flux contributions due to the electrostatic ($\mathbf{E} \times \mathbf{B}$ velocity \mathbf{v}_E), the magnetic flutter ($\mathbf{v}_{A_{\parallel}}$) and the magnetic compression ($\mathbf{v}_{B_{\parallel}}$) parts. Here $\mathbf{v}_{B_{\parallel}}$ is drift velocity due to perturbations of magnetic field in the parallel direction, $\mathbf{v}_{B_{\parallel}} = \mathbf{b} \times \nabla \mu \langle B_{\parallel} \rangle_{gy} / B_0$.

The total mode growth rate and real frequencies of the linear Fourier modes are obtained as:

$$\gamma(t) = \ln \left[\frac{\sqrt{\int |\hat{\phi}(t)|^2 + |\hat{A}_{\parallel}(t)|^2 + |\hat{B}_{\parallel}(t)|^2 ds}}{\sqrt{\int |\hat{\phi}(t - \Delta t)|^2 + |\hat{A}_{\parallel}(t - \Delta t)|^2 + |\hat{B}_{\parallel}(t - \Delta t)|^2 ds}} \right] / \Delta t \quad (3.58)$$

$$\omega(t) = \left[\text{Arg} \left(\int |\hat{\phi}(t)|^2 ds \right) - \text{Arg} \left(\int |\hat{\phi}(t - \Delta t)|^2 ds \right) \right] / \Delta t \quad (3.59)$$

where, in the frequency equation, the magnetic flutter and magnetic contributions are dropped in the definition for simplicity. $\gamma(t)$ is the growth rate defined for one linear mode only.

For the normalisation of these fluxes, growth rates and frequencies, see section 3.3.

4

Linear stability analysis of a JET hybrid H-mode plasma

This chapter presents the linear stability analysis of the JET hybrid H-mode discharge #75225. Linear gyrokinetic simulations are performed using the gyrokinetic code GKW [69] in the local approximation limit. The dominant instability in the central region $\rho < 0.3$ is identified and its parametric dependencies are investigated. Comparisons with the radial region, $\rho > 0.3$, where previous work has already been done [35, 36, 77] are also presented.

4.1 Input parameters of JET hybrid H-mode discharge 75225

An experimental JET hybrid H-mode discharge #75225 has been selected for the purpose of investigating turbulent transport and validating available transport models in the plasma central region. A hybrid or improved H-mode plasma is halfway between a baseline H-mode plasma and an Advanced Tokamak plasma [78, 79, 80]. In these plasmas, an enhanced normalized confinement time can be achieved by optimizing the current density profile. The resulting safety factor profile in the central region is flat but above unity, which prevents the destabilization of large MHD instabilities [80]. In addition, the plasma current is driven by inductive and non-inductive drive with a high fraction of bootstrap current that allows a longer pulse duration.

4.1.1 Experimental profiles

The selected JET pulse corresponds to the 2008-2009 JET experimental campaign with Carbon plasma-facing components (CFC). The profiles for electron density and temperature are obtained by measurements from High-Resolution Thomson

Scattering (HRTS) while Charge Exchange Recombination Spectroscopy (CXRS) is used to measure the carbon density, temperature and toroidal rotation. This hybrid discharge of the Carbon wall era was analyzed for $\rho > 0.33$ in details in [81, 82, 35, 36, 77] and has been selected for the following reasons: it has high-quality core profile measurements for electron and of carbon (CXRS), no sawteeth (q on axis > 1) and no other significant core MHD activity in the selected time interval, $t = 6.0 - 6.5$ s. Even though the ultimate goal of this thesis is to understand the W transport, however, we have selected these specific well-diagnosed discharges of the carbon wall era first. Because turbulent transport in the central region remains largely unexplored so far, so it is important to understand the physical mechanism first. That is why we are using carbon discharges first which have better diagnostic measurements and well documented. In practice, the tolerable concentration of W in a tokamak plasma is very low $n_W/n_e \sim 10^{-5}$ due to radiation losses. At such low concentration, the impurity behaves as a trace and does not impact turbulent transport or linear stability. Actually, even for carbon whose concentration is $n_C/n_e = 0.01$ at $\rho = 0.15$, we have verified that removing the carbon impurity (red curve) has only a moderate impact on the linear stability as seen in the figure 4.21.

Numerical simulations are performed using the δf (the perturbed distribution function) gyro-kinetic (the kinetic Vlasov equation averaged over the fast gyromotion) code GKW [69] in the local approximation limit. The input parameters for the simulation are calculated using plasma profiles obtained from Gaussian process regression (GPR) of experimental measurements [83].

The experimental input plasma profiles with GPR fits for the electron density n_e , electron temperature T_e (the data combines measurements from HRTS and LIDAR which is an older Thomson scattering system in JET), ion temperature T_i (assuming $T_D = T_C$), toroidal rotation frequency Ω_{tor} and safety factor (q) are illustrated in figure 4.1. Here, the blue points represent the experimental measured data points with error bars and the red (solid) lines show the GPR fit. The shaded area represents the error bars for the GPR fits, and all errors are depicted as $\pm 2\sigma$. The magnetic equilibrium is computed with the EFIT (Equilibrium FITing) [84] based on magnetic measurements and constrained with MSE measurements and the total kinetic pressure, including fast ions (table 4.2). Simulations are performed for three species (deuterium, electron, and Carbon), including parallel magnetic vector potential (δA_{\parallel}) and parallel magnetic field (δB_{\parallel}) fluctuations, rotation (drive from parallel velocity gradient and inertial effects) and collisions. In some cases, the fast ion population from the Neutral Beam Injection (NBI) is added as a fourth species, with a Maxwellian distribution function. The impact of approximating the fast ion population as a Maxwellian was shown to be of the order of 10% on the growth rate of ITG modes [85]. The magnetic equilibrium for the plasma shape is specified using the Miller parametrization [74]. A linearised Fokker-Planck collision operator is used to model collisions including the pitch-angle scattering, energy scattering and collisional friction terms. The centrifugal and Coriolis drifts are taken into account and all species collisions are retained in the simulations. The corresponding local plasma input parameters normalized in GKW units are listed in table 4.1 and the Miller parameterisation is given in table 4.2.

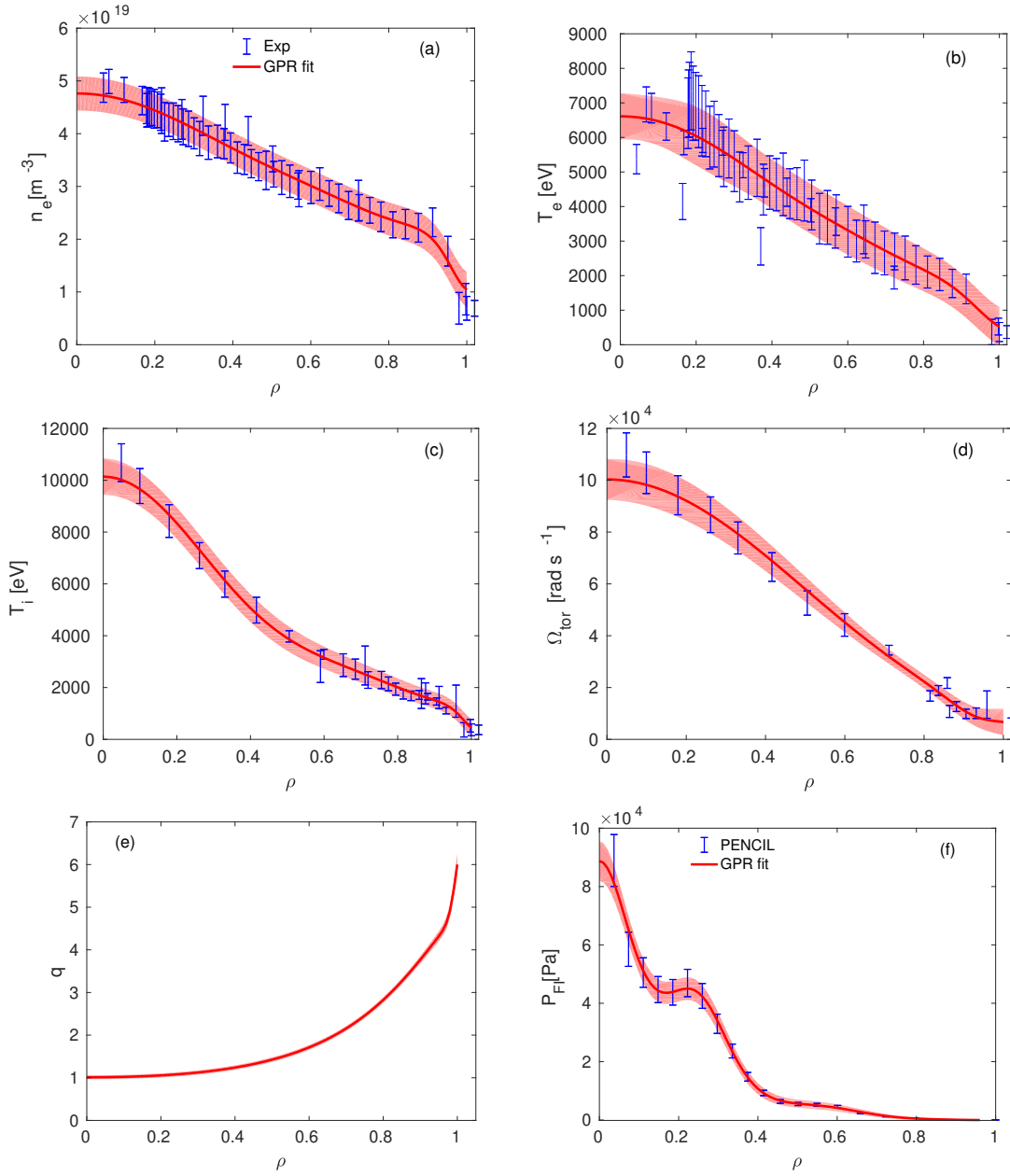


Figure 4.1 – Plasma input profiles for the JET discharge #75225 at 6-6.5 s obtained from GPR fits of experimental measurements as a function of the normalized toroidal flux ρ for (a) electron density, (b) electron temperature, (c) ion temperature, (d) toroidal rotation frequency, (e) safety factor q and (f) fast ion pressure profile obtained from PENCIL. In figure (b), the measurements are from two diagnostics HRTS and LIDAR and three offset points are from ECE measurements.

In table 4.1, ν is the reference normalized collisionality from which inter-species collisionalities are computed: $\nu = \frac{n_i e^4 \ln \Lambda^{e/i} R_0}{4\pi \epsilon_0^2 m_e^2 v_{the}^3 v_{thref}}$, with $\ln \Lambda^{e/i}$ the Coulomb logarithm. The actual electron to ion collisionality used in the code is enhanced to take into account the impact of impurities not included as a kinetic species (the Z_{eff} value

obtained with the C impurity alone is lower than the actual Z_{eff} value measured from Bremsstrahlung emission). The electron plasma β is defined as $\beta_e = 2\mu_0 n_e T_e / B_{ref}^2$. In the simulations, the ion mass (m_i) is taken as the reference mass, the electron density (n_e) as the reference density and the ion temperature (T_i) as the reference temperature, therefore the beta value given as input in GKW is $2\mu_0 n_e T_i / B_{ref}^2$, which differs from the electron β by a factor T_i / T_e . The other normalized parameters and their definitions are given in chapter 3.

Table 4.1 – Normalized input parameters used in GKW simulations for the JET 75225 discharge selected in the time interval 6.0-6.5 s.

ρ	$\frac{R}{L_{Ti}}$	$\frac{R}{L_{Te}}$	$\frac{R}{L_{Tf}}$	$\frac{T_e}{T_i}$	$\frac{T_f}{T_i}$	$\frac{R}{L_{nC}}$	$\frac{R}{L_{ne}}$	$\frac{R}{L_{nf}}$	$\frac{n_C}{n_e}$	$\frac{n_f}{n_e}$	$\beta_e[\%]$	u	u'	Z_{eff}	ν
0.15	4.23	1.99	1.80	0.69	5.6	-0.70	1.5	0.80	0.01	0.12	3.19	0.32	0.59	1.7	0.015
0.20	5.57	2.70	-0.58	0.72	6.0	-1.13	1.9	-0.88	0.01	0.12	2.96	0.32	0.80	1.7	0.016
0.25	6.60	3.31	2.41	0.76	6.6	-1.45	2.3	1.84	0.01	0.13	2.69	0.32	0.99	1.7	0.017
0.33	7.70	4.09	9.64	0.84	6.0	-1.51	2.7	8.97	0.01	0.10	2.23	0.32	1.31	1.7	0.020
0.40	7.85	4.51	10.71	0.91	7.8	-0.87	2.9	10.24	0.02	0.07	1.85	0.31	1.57	1.7	0.022
0.50	6.30	5.15	4.44	1.04	4.6	2.70	3.1	3.41	0.02	0.06	1.39	0.29	1.88	1.7	0.027
0.60	5.90	5.50	9.61	1.05	4.6	4.41	3.3	7.96	0.02	0.06	1.03	0.24	0.24	1.7	0.035

4.1.2 Magnetic equilibrium reconstruction

The Miller parameterization is used for the magnetic equilibrium description, see table 4.2. A separate magnetic equilibrium without the fast ion pressure has been calculated with the CHEASE code [75] and the corresponding Miller parametrization for this case is listed in table 4.3. As seen in figure 4.2, the main difference between the two equilibria is a larger radial derivative of the total pressure, β' , and of the center flux surfaces R'_{mil} for $\rho > 0.3$ when the fast ion pressure is included in the magnetic equilibrium, see figure 4.1 (f). The fast ion characteristics from NBI is modelled using the PENCIL code [86] which solves a simplified version of the Fokker-Planck equation and includes ionization by charge exchange, ionization by plasma electrons and ions. It should be noted that for the fast ion profile calculations, Monte-Carlo NEMO-SPOT [87] simulation within CRONOS [88] is also available for the selected JET discharge. Since the focus of the present analysis is not on the impact of fast ions, we chose to use the default "chain2" analysis performed with PENCIL [86].

4.1.3 Grid convergence

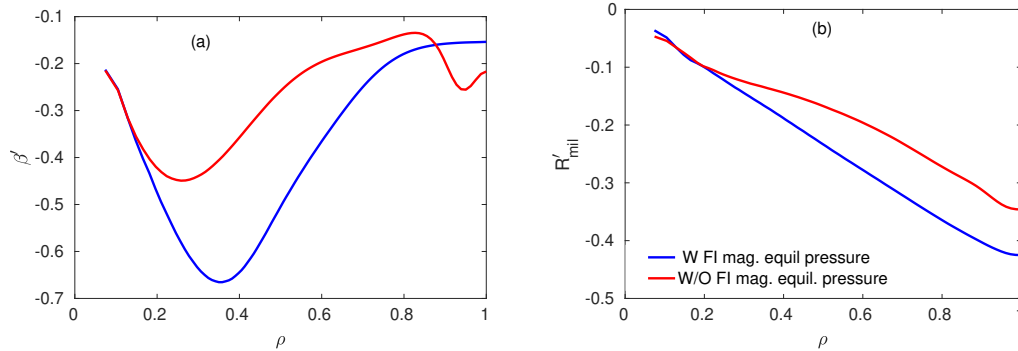
Grid convergence tests have been carried out to determine the required grid as illustrated in figure 4.3. In this figure, the linear growth rate is plotted for the most unstable mode at $k_\theta \rho_i = 0.35$ for $\rho = 0.15$ as a function of the number of grid points for the magnetic moment N_μ (a), the parallel velocity N_{v_\parallel} (b) and the number of points in the parallel direction per poloidal turns N_s (c). The reference values for the scans were: $N_\mu = 16$, $N_{v_\parallel} = 64$, $N_s = 32$. After linear grid convergence tests, the numerical grid parameters chosen are presented in table 4.4. The number of poloidal turns is varied from 5 to 50 depending on the value of the magnetic shear and $k_\theta \rho_i$ (more extended mode structure at low magnetic shear and low $k_\theta \rho_i$). The

Table 4.2 – Miller parameters for the magnetic equilibrium including the fast ion pressure.

ρ	ϵ	q	\hat{s}	β'	κ	δ	ζ	s_κ	s_δ	s_ζ	R'_{mil}	Z'_{mil}
0.15	0.05	1.10	0.05	-0.37	1.35	0.02	0.001	-0.004	0.01	0.003	-0.08	-0.005
0.20	0.07	1.10	0.02	-0.48	1.35	0.02	0.001	-0.007	0.02	-0.00	-0.10	-0.008
0.25	0.09	1.11	0.05	-0.57	1.35	0.03	0.001	-0.01	0.03	0.001	-0.12	-0.007
0.33	0.11	1.14	0.21	-0.66	1.34	0.04	0.001	-0.01	0.04	-0.002	-0.16	-0.017
0.40	0.14	1.22	0.49	-0.64	1.34	0.05	0.001	-0.002	0.05	0.001	-0.19	-0.022
0.50	0.17	1.42	0.98	-0.50	1.35	0.06	0.00	0.03	0.09	-0.004	-0.23	-0.026
0.60	0.21	1.74	1.42	-0.37	1.36	0.08	-0.001	0.09	0.14	-0.01	-0.28	-0.063

Table 4.3 – Miller parameters for the magnetic equilibrium without including the fast ion pressure.

ρ	ϵ	q	\hat{s}	β'	κ	δ	ζ	s_κ	s_δ	s_ζ	R'_{mil}	Z'_{mil}
0.15	0.05	1.08	0.05	-0.36	1.31	0.02	0.0024	-0.008	0.02	0.005	-0.08	-0.006
0.20	0.07	1.08	0.02	-0.42	1.30	0.02	0.0003	-0.005	0.02	-0.003	-0.10	-0.006
0.25	0.09	1.09	0.05	-0.45	1.30	0.03	0.0010	-0.008	0.02	0.002	-0.11	-0.007
0.33	0.12	1.12	0.20	-0.42	1.30	0.04	0.0007	-0.00	0.03	-0.002	-0.13	-0.014
0.40	0.14	1.20	0.47	-0.36	1.30	0.04	0.0004	0.015	0.04	-0.002	-0.14	-0.018
0.50	0.18	1.39	0.95	-0.26	1.31	0.06	-0.0003	0.060	0.08	-0.008	-0.17	-0.023
0.60	0.21	1.70	1.40	-0.20	1.33	0.07	-0.0022	0.127	0.13	-0.021	-0.20	-0.053

**Figure 4.2** – The radial derivatives of the total pressure β' (a) and center flux surfaces R'_{mil} (b) as a function of radial location ρ . The blue curve represents the case when fast ion pressure is included in the magnetic equilibrium and red line is for the case when the fast ion pressure is neglected in the magnetic equilibrium.

linear stability analysis is carried out from radial location $\rho = 0.15$ to $\rho = 0.6$, where ρ is the normalised toroidal flux coordinate.

At $\rho = 0.15$, the nominal value of the magnetic shear is 0.01. At such a low magnetic shear, the distance between resonant flux surfaces $\delta = \frac{1}{nq'}$, with $q' = \partial q / \partial r$ and n the toroidal mode number, becomes comparable to the minor plasma radius

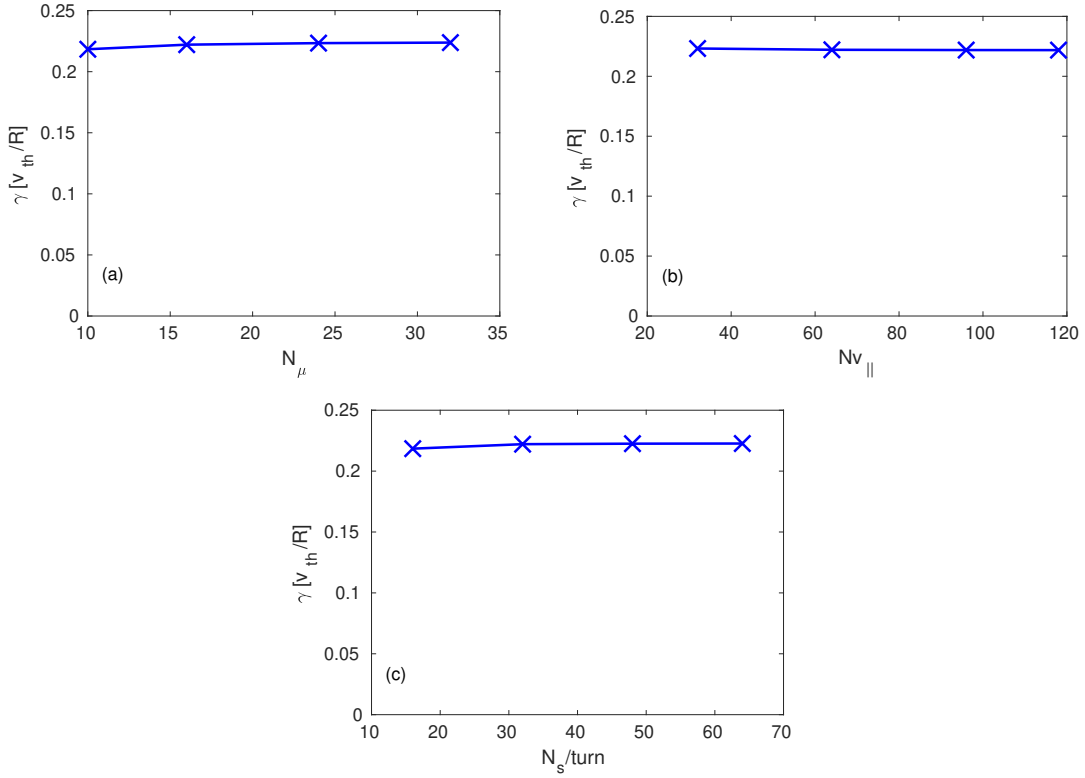


Figure 4.3 – The linear growth rate for the most unstable mode at $k_\theta \rho_i = 0.35$ for $\rho = 0.15$ as a function of the number of grid points for the magnetic moment N_μ (a), the parallel velocity $N_{v_{\parallel}}$ (b) and the number of points in the parallel direction per poloidal turns N_s (c).

Table 4.4 – Numerical grid parameters used for simulations of JET discharge 75225.

N_μ	$N_{v_{\parallel}}$	N_s
16	64	32

and the validity of the ballooning representation may be questioned (although the relevant criterion is the radial mode extent rather than the distance between resonant flux surfaces). To be on the safe side, the value of the magnetic shear at this location has therefore been increased to 0.05, which is well within the uncertainty on this quantity. The validity of the ballooning approximation is checked a posteriori in section 4.3 and the impact of the magnetic shear value on the mode growth rate is explored in figure 4.13 and 4.14.

4.2 Linear unstable modes across the minor radius and impact of fast ions

The objective of this section is to determine which kind of instabilities dominates in the inner core of the selected discharge and compare the results with other radial locations. To do so, linear gyrokinetic simulations have been performed across the plasma minor radius using the input parameters given in tables 4.1, 4.2, 4.3 and the results are presented in figure 4.4. Here, the linear growth rate and real frequencies spectra are shown at three radial locations $\rho = 0.15$, $\rho = 0.33$ and $\rho = 0.60$, as a function of $k_\theta \rho_i$, where k_θ is the binormal wave vector and $\rho_i = m_i v_{thref} / (e B_{ref})$ is the reference ion Larmor radius. In this figure, the impact of the fast ion population is investigated by performing three sets of simulations: 1) with fast ions as a kinetic species and with the fast ion pressure in the magnetic equilibrium (red curve), 2) without fast ions as a kinetic species and without the fast ion pressure in the magnetic equilibrium (green line), 3) without fast ions as a kinetic species but with fast ion pressure in the magnetic equilibrium (blue line). In this thesis's framework, including the kinetic fast ions means that this particle population has been included as a new species in the evolution of the gyrokinetic equation.

At $\rho = 0.15$, all the linearly unstable modes rotate in the ion diamagnetic drift direction ($\omega_r > 0$) and have a real frequency much larger than their linear growth rate. These unstable modes are identified as Kinetic Ballooning Modes (KBM); this point will be clarified later in the chapter (section 4.3). At the lowest $k_\theta \rho_i$, stable Micro-Tearing Modes (MTM) are also observed, characterized by their negative frequency and the even parity of the vector potential fluctuations. These are stable linearly but will matter for the quasi-linear analysis of section 5.2. Including fast ions as a kinetic species decreases the KBMs mode growth rate by about 20%, whereas the fast ion pressure in the magnetic equilibrium has almost no impact on the mode growth rate, simply because it has nearly no impact on the Miller parameters at this location as seen in figure 4.2.

At the radial location, $\rho = 0.6$, the most unstable modes are Ion Temperature Gradient (ITG) modes. Including the fast ions as a kinetic species is found to reduce the mode growth rate, consistently with the previous gyrokinetic analysis performed using the gyrokinetic code GENE [36, 77]. When the fast ion pressure is included in the magnetic equilibrium reconstruction, the ITG mode growth rate increases, which is typical at high β , as observed earlier in [89], where increasing β' in the local Grad-Shafranov equilibrium (i.e. increasing β' keeping the other Miller parameters fixed) first leads to a destabilization of the ITG modes.

At the intermediate position, $\rho = 0.33$, the situation is more complex. Without fast ions as a kinetic species and fast ions pressure in the magnetic equilibrium, the most unstable mode is an ITG at high $k_\theta \rho_i$ and a KBM mode at low $k_\theta \rho_i$, as indicated by the jump in the mode frequency. Including the fast ion pressure in the magnetic equilibrium significantly stabilizes the KBM modes and has no impact on the ITG modes. When fast ions are included as a kinetic species, the KBM and ITG modes are stabilized, consistently with the picture at $\rho = 0.15$ and $\rho = 0.6$, except at low $k_\theta \rho_i$ where a mode with a higher frequency is excited. This mode

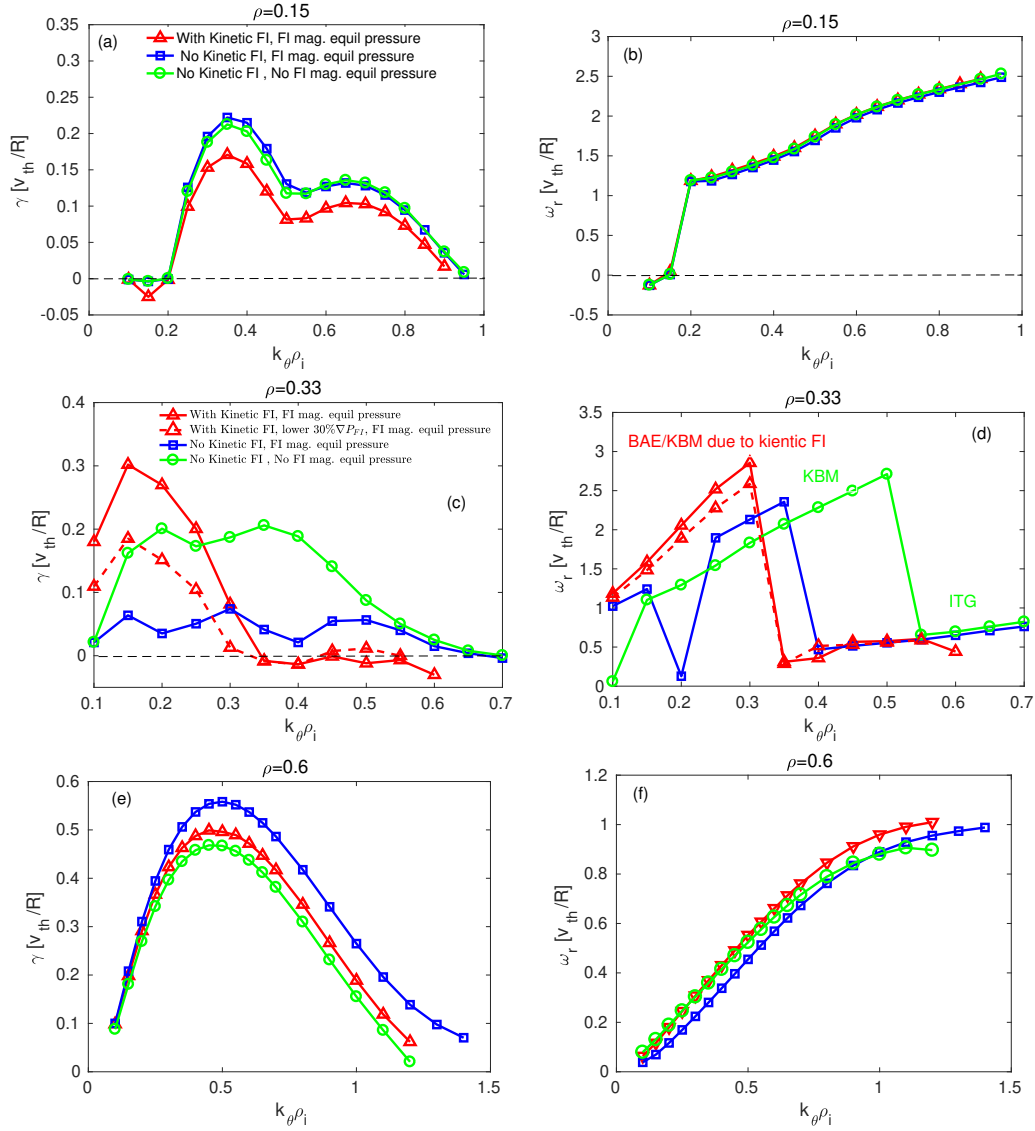


Figure 4.4 – Linear growth rate (left) and real frequency (right) spectra as a function of $k_{\theta}\rho_i$, at different radial locations: (a) and (b) at $\rho = 0.15$, (c) and (d) at $\rho = 0.33$, (e) and (f) at $\rho = 0.60$. The green curve represents the case without kinetic fast ions and without fast ion pressure in the magnetic equilibrium. The blue line correspond to the case without kinetic fast ions but the magnetic equilibrium includes the fast ion pressure. The red curve indicates the case with kinetic fast ions and fast ion pressure in the magnetic equilibrium, with the nominal fast ion pressure for the kinetic species (full line) or reduced by 30% (dashed line).

is driven by fast ions and was identified as a hybrid BAE (Beta induced Alfvén Eigenmode)/KBM mode in [36, 77]. The growth rate of this mode significantly decreases when the kinetic fast ion pressure gradient is lowered by 30% (red dashed line in figure 4.4 (c) and (d)) as noted in [36, 77]. Note that the inputs used in the present gyrokinetic simulations are slightly different from those used in [36, 77]. For the main species, this is mostly due to the fact that here fits have been done using the recently developed GPR tools [83]. For the fast ion population, the difference is

larger since the present profiles are from the standard PENCIL [86] analysis of JET whereas the ones used in [36, 77] were obtained from higher fidelity Monte Carlo NEMO-SPOT [87] simulations. The dominant instabilities and qualitative behaviour concerning the impact of fast ions are nevertheless similar.

The linear stability analysis is then extended to additional radial locations, and the maximum linear growth rate and corresponding frequency of the most unstable modes are shown as a function of the radial position in figure 4.5. In the inner core region ($\rho < 0.4$), the dominant mode is found to be a KBM (full symbol). At the mid and outer radius ($\rho \geq 0.4$) it changes to an ITG mode (open symbol). Including fast ions as a kinetic species has a stabilizing impact on the mode growth rate (the difference between blue and red curve) at all radial locations except at $\rho = 0.33$, where it destabilizes a BAE/KBM mode (full star symbol) as discussed earlier. Taking into account the fast ions pressure in the magnetic equilibrium stabilizes KBMs and slightly destabilizes ITGs, consistent with the examples discussed in figure 4.4. The fast ion stabilization of ITG modes has already been seen earlier in an ITG dominated JET plasmas [90, 36] and ASDEX Upgrade [91].

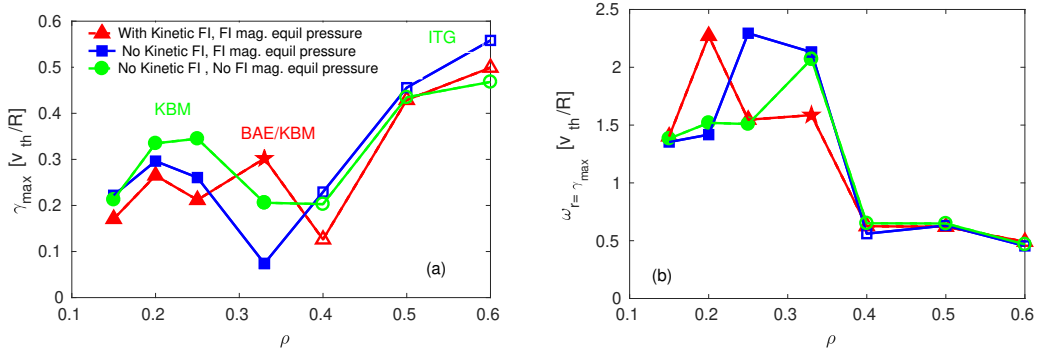


Figure 4.5 – Growth rate and frequency of the most unstable modes as a function of radial location ρ . Full symbols are used for KBM modes and open symbols for ITG modes. The (red) full star symbol at $\rho = 0.33$ corresponds to a hybrid BAE/KBM mode destabilised due to kinetic fast ions. Same color code as in figure 4.4.

The detailed investigation of the impact of kinetic fast ion on KBMs is itself an area of research and is not a focus of this work. However, it will be interesting to explore it in the future. This thesis primary goal is to study the dynamics of microinstabilities leading to turbulent transport in the inner core $\rho < 0.3$, which is a rather uncharted territory so far; therefore, fast ions will now be neglected for simplicity.

To identify the KBM threshold a linear β scan is performed from $\rho = 0.15$ to $\rho = 0.6$. Figure 4.6, shows the variation of linear growth rate and frequency as β_e is varied at three radial locations $\rho = 0.15$, $\rho = 0.33$ and $\rho = 0.60$. Here, the β_e scans are performed for the wave-vector corresponding to the most unstable mode at each β value, as in figure 4.5. These wavevectors are $k_{\theta}\rho_i = 0.35, 0.35$ and 0.5 for $\rho = 0.15, 0.33$ and 0.6 .

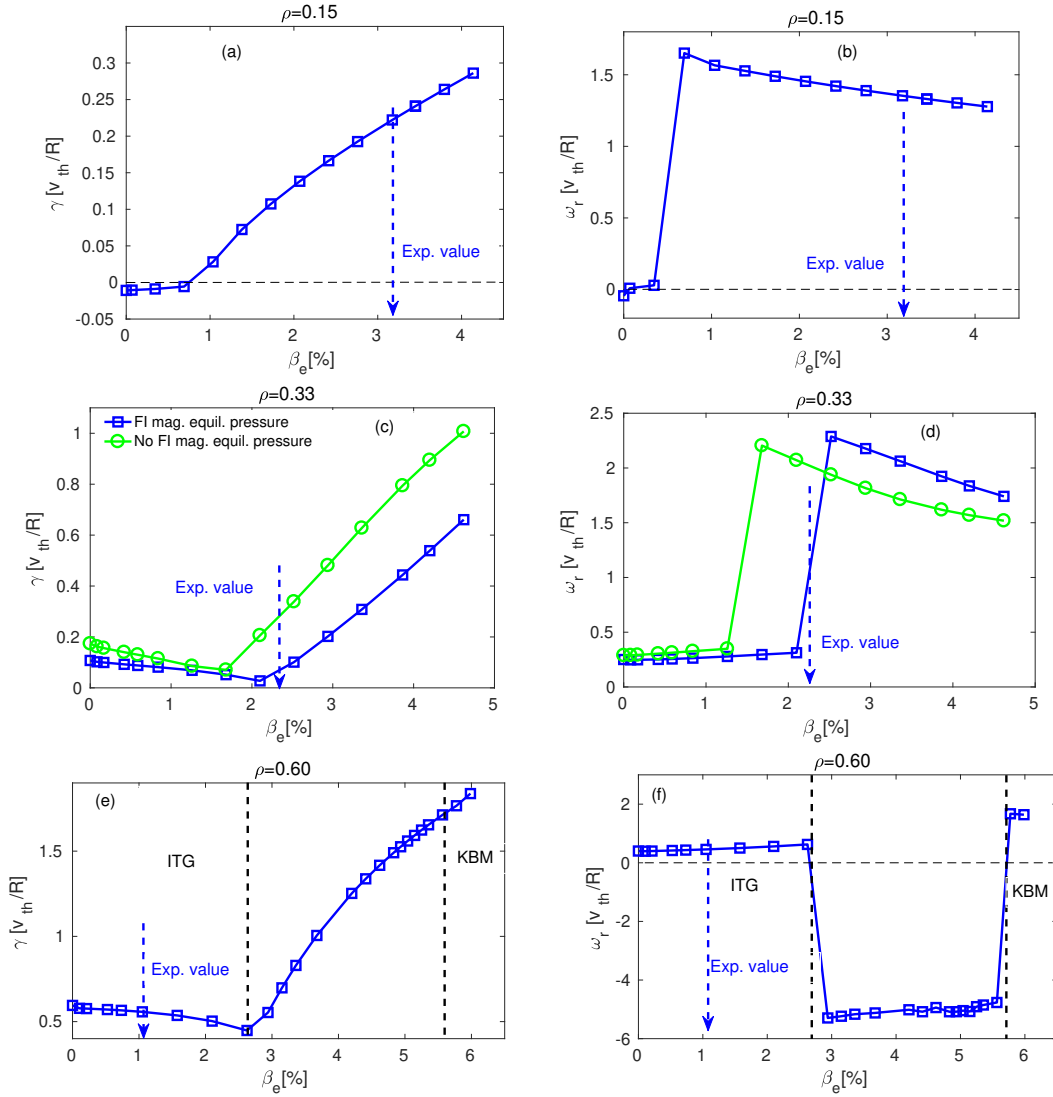


Figure 4.6 – Linear growth rate (left) and real frequency (right) spectra as a function of β_e , at different radial locations: (a) and (b) at $\rho = 0.15$, (c) and (d) at $\rho = 0.33$, (e) and (f) at $\rho = 0.60$. The vertical dotted arrow shows the experimental β_e value at the reference location. Same colour coding as in figure 4.4

At $\rho = 0.15$, no mode is unstable at low β_e . At higher β_e values, KBMs are destabilized and their growth rate increases with β . At $\rho = 0.33$, for low β_e values, the dominant instability is an ITG mode. The growth rate of this mode decreases with increasing β_e until a KBM takes over with a sharp jump in frequency. The threshold in β_e decreases when fast ion pressure is neglected in the magnetic equilibrium (the green curve). This decrease in threshold is due to the decrease in the total pressure gradient (β') at this location (seen in figure 4.2). At radial location $\rho = 0.6$, the ITG growth rate decreases with β_e until a tearing parity mode with negative frequency is destabilized. At higher values of β_e KBMs take over.

As discussed above, the KBM modes become linearly unstable only when a certain threshold in β_e is exceeded. This threshold is called β_e^{crit} and is obtained

by extrapolating the KBM growth rate by a quadratic fit and finding the value at which the KBM fit function becomes zero. The β_e^{crit} values at various radial locations are plotted in figure 4.7 (a). The β_e^{crit} threshold is less than 1% in the inner core and increases when moving further outwards. The increase in the β_e threshold is closely linked to the increase of the magnetic shear across the minor radius (Fig. 4.7 (b)) which is reminiscent of the dependence of the MHD ballooning limit $\beta_{MHD}^{crit} \sim 0.6\hat{s}/[q_0^2(2R/L_n + R/L_{Ti} + R/L_{Te})]$ (shown by the dotted red line in Fig. 4.7 (a)) expected to approximately reproduce the dependencies of β_e^{crit} for KBMs [92]. Here β_e^{crit} is found higher than β_{MHD}^{crit} , but depending on the conditions, the KBMs can also be destabilized at β_e values significantly below β_{MHD}^{crit} [93, 53, 94].

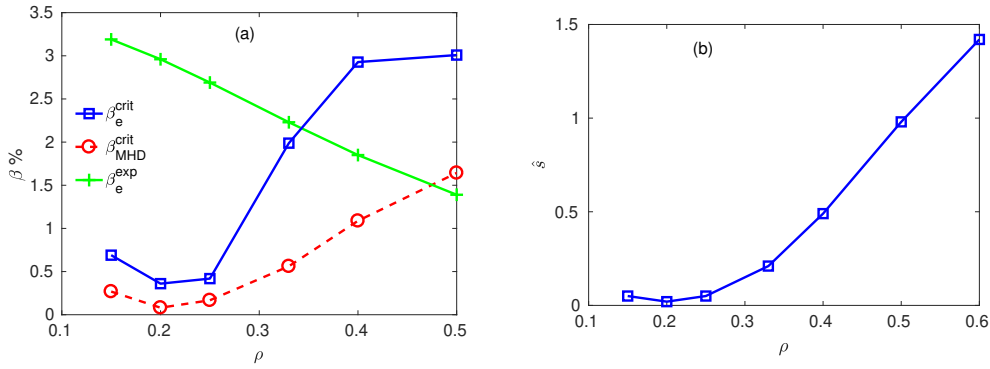


Figure 4.7 – β_e (a) and magnetic shear \hat{s} values (b) as a function of the radial location ρ . In figure (a), the blue curve corresponds to the critical beta β_e^{crit} threshold of KBM, the red (dotted) curve represents the MHD β_{MHD}^{crit} limit and the green curve experimental beta β_e^{exp} values.

The impact of the ITG/KBM transition on the cross-phase between fluctuating quantities is now explored. The linear normalized electron (Q_{eN}), ion heat (Q_{iN}) fluxes, and particle fluxes (Γ_{eN}) for $\rho = 0.33$ (from figure 4.6 (c)) are plotted as a function of β_e in figure 4.8. The fluxes are normalized to the mode amplitude as: $Q_{sN} = Q_s/\mathcal{A}_L^2$, where the mode amplitude is defined as: $\mathcal{A}_L = \sqrt{\int [|\phi|^2 + |A_{\parallel}|^2 + |B_{\parallel}|^2] ds / \int ds}$. Here, the normalized linear fluxes of heat and particle are decomposed into electrostatic (due to $\mathbf{E} \times \mathbf{B}$ drift (blue curve)) and electromagnetic (due to magnetic flutter (red curve) and compression (green curve)) fluxes, respectively (Eq. 3.56). The normalized $\mathbf{E} \times \mathbf{B}$ fluxes are dominant in both ITG and KBM regimes. The normalized magnetic flutter fluxes are negligible even for the electron channel in the KBM regime with some inward convection at high β in the ITG range. The normalized ion heat flux in the KBM regime is $\sim 70\%$ lower than in the ITG turbulence even though KBM have larger linear growth rates (Fig. 4.6 (c)). The normalized electron heat and particle fluxes also show similar behaviour than the ion heat fluxes. The phase shifts between fluctuating fields are therefore less favorable to transport for KBMs than ITGs, as seen earlier in reference [95].

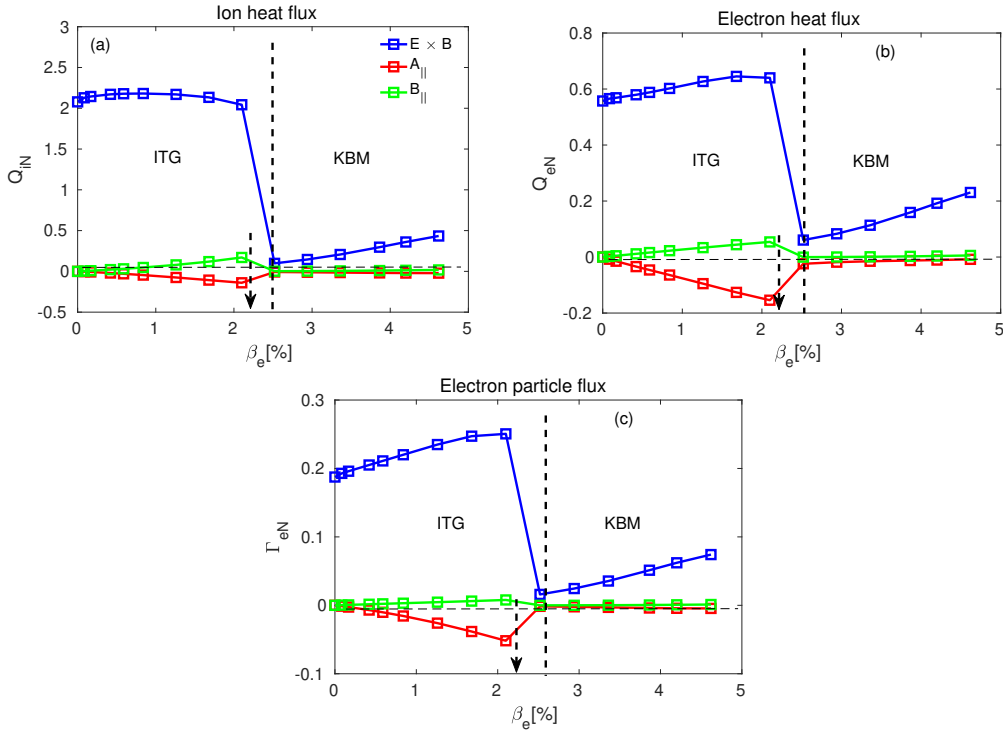


Figure 4.8 – Normalised linear ion and electron heat fluxes (a) and (b), and electron particle flux (c) as function of β_e for $k_{\theta}\rho_i = 0.35$ at $\rho = 0.33$. The blue curves corresponds to fluxes due to $\mathbf{E} \times \mathbf{B}$ contribution, red due to magnetic flutter (A_{\parallel}) and green due to magnetic compression (B_{\parallel}). The vertical dotted line represents the transition from ITG to KBM range and vertical dotted arrow shows the experimental β_e value.

Linear simulations were also performed up to electron scales for $\rho = 0.15$ and $\rho = 0.33$. Interestingly, Electron Temperature Gradient modes (ETG) that can be destabilized at high wavenumbers are found to be stable at both radii and there is no evidence of ETG mode destabilization at these locations. This observed behaviour could be understood by looking at a proxy for the linear threshold of ETG modes as given in reference [96] and defined as:

$$(R/L_{T_e})^{crit} = \max \left(\left(1 + Z_{eff} \frac{T_e}{T_i}\right) \left(1.33 + 1.91 \frac{\hat{s}}{q}\right) (1 - 1.5\epsilon), 0.8R_{Ln} \right), \quad (4.1)$$

where ϵ is a correction factor $0 \leq \epsilon \leq 0.3$ due to finite aspect ratio. The $(R/L_{T_e})^{crit}$ values at radial locations $\rho = 0.15$ and $\rho = 0.33$ is ~ 3.1 and ~ 4.0 respectively, which is higher or close to the nominal values of R/L_{T_e} at these locations.

4.3 Linear stability analysis at $\rho = 0.15$

In the following section, the focus is on the radial location $\rho = 0.15$. The identification of the most unstable mode as a KBM will be supported, and its parametric dependencies further documented. Unless otherwise stated, all linear simulations will

be performed without fast ions as a kinetic species and with the fast ion pressure included in the equilibrium.

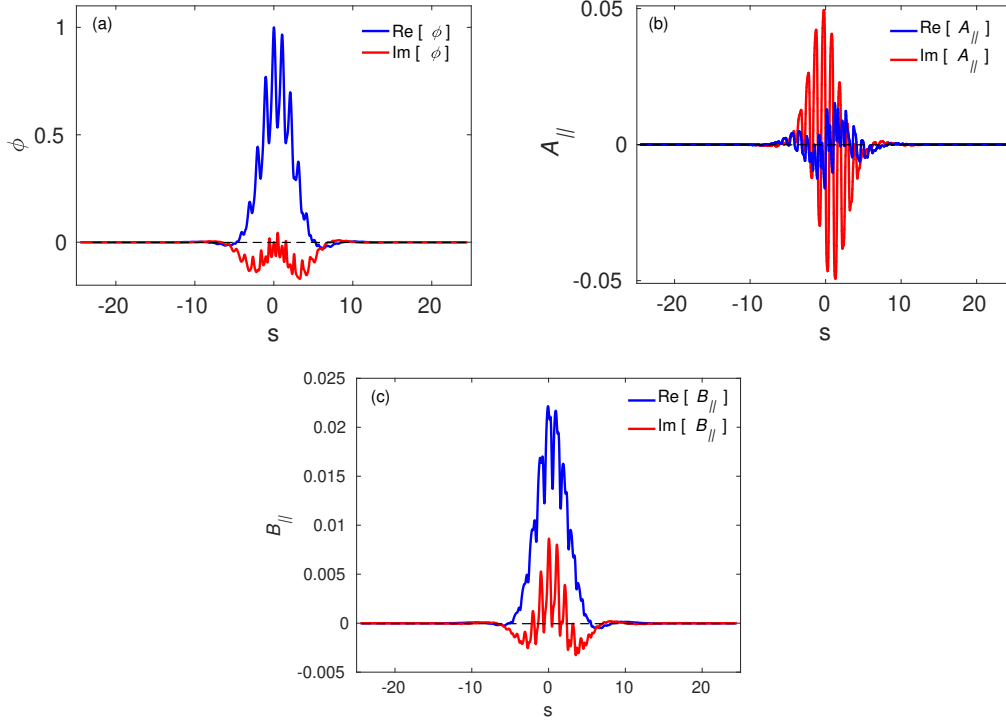


Figure 4.9 – Parallel mode structure of ϕ (a), A_{\parallel} (b) and B_{\parallel} (c), as a function of the parallel coordinate s for the most unstable mode $k_{\theta}\rho_i = 0.35$ at $\rho = 0.15$. The blue curve corresponds the real part and the red line indicates the imaginary part.

The eigenmode structure of the perturbed electrostatic potential (ϕ), vector potential (A_{\parallel}) and magnetic compression (B_{\parallel}) for the most unstable mode ($k_{\theta}\rho_i = 0.35$) is given in figure 4.9 as a function of the parallel coordinates s at $\rho = 0.15$. The perturbed fields $\delta\phi$, δA_{\parallel} and δB_{\parallel} are normalised as follows: $\phi = \alpha_L \frac{e\delta\phi}{\rho_* T_i}$, $A_{\parallel} = \alpha_L \frac{\delta A_{\parallel}}{\rho_*^2 B_{\text{ref}} R_0}$ and $B_{\parallel} = \alpha_L \frac{\delta B_{\parallel}}{\rho_* B_{\text{ref}}}$ with $\rho_* = \rho_i/R_0$ and α_L an additional normalising factor used in linear simulations to have $\text{Re}[\phi] = 1$ and $\text{Im}[\phi] = 0$ at the s position where $|\phi|$ is maximum (for the definition of perturbed fields ϕ and A_{\parallel} , see section 2.1.3.1). One poloidal turn corresponds to $\Delta s = 1$. The eigenfunctions have ballooning parity as seen earlier in the section 2.1.3 in chapter 2. The electrostatic perturbation amplitude is higher than the magnetic perturbation amplitude. Note that as a result of the up-down asymmetry of the magnetic equilibrium and the finite values of the background toroidal flow u and parallel flow shear u' which break the parallel symmetry, the parity of the eigenfunction is only approximate. It is important to note that the mode structures are extremely elongated along the field lines especially for low wavenumbers and therefore a very high radial resolution was needed (up to 50 poloidal turns at low $k_{\theta}\rho_i$) to resolve the modes properly. The corresponding radial mode width in real space is obtained from a Fourier transform along the parallel coordinate and the 2D poloidal cut of the real part of ϕ_r is shown in figure 4.10 using the local $\rho^* = 0.0033$ value. The KBM tends to be less ballooned

than ITG with a ratio of the amplitude at the LFS (Low Field-Side) and HFS (High Field-Side) of 40% compared to that for ITG at $\rho = 0.33$ of 60% difference. The radial mode width is about 5 cm and therefore much smaller than the minor radius $a \sim 1$ m or $L_{Ti} = 0.74$ m at this location. This validates a posteriori the use of the local approximation at this low magnetic shear values.

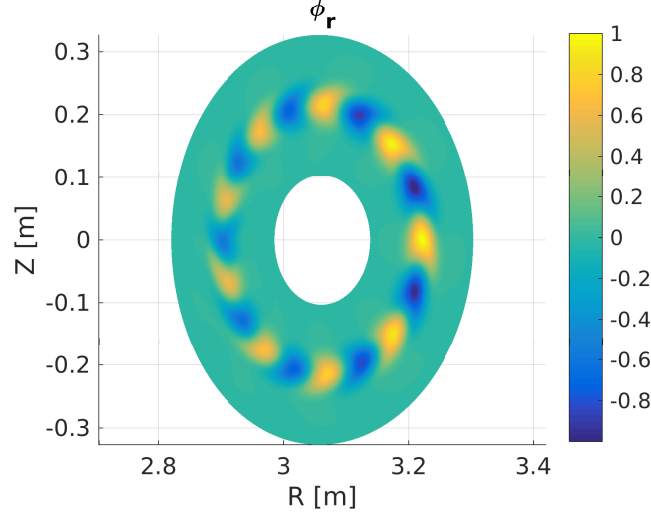


Figure 4.10 – 2D poloidal cut of real part of electrostatic potential (ϕ_r) on the R and Z plane for the most unstable mode $k_\theta \rho_i = 0.35$ at $\rho = 0.15$.

In order to further investigate the drive mechanism of these KBM modes, the main ion pressure gradient has been scanned around the experimental value by keeping the main ion density gradient constant ($R/L_{nD} = \text{const}$) and varying the main ion temperature gradient (R/L_{Ti}) in one case, or by varying the main ion density gradient and keeping the main ion temperature gradient constant ($R/L_{Ti} = \text{const}$) in another. As shown in figure 4.11, varying R/L_{Ti} at fixed R/L_n (blue curve) or R/L_n at fixed R/L_{Ti} (red curve) has almost the same impact on the mode growth rate, which suggests that the mode is driven by the ion pressure gradient.

The mode growth rate is weakly dependent on the normalized electron temperature gradient R/L_{Te} , as shown in figure 4.12.

4.3.1 Impact of magnetic shear and plasma beta

The impact of magnetic shear and the plasma beta is investigated in this section. In figure 4.13, the mode growth rates and frequencies for the magnetic shear \hat{s} scans are plotted, where the nominal value of \hat{s} is represented by a vertical dotted line. The growth rate decreases when the absolute value of the magnetic shear increases until complete stabilization. The frequency is weakly affected. The low absolute value of the magnetic shear appears to be critical for the existence of KBM modes in the inner core of these hybrid plasmas. To illustrate the impact of the magnetic shear on the parallel mode structure, the real component of the perturbed electrostatic potential ϕ_r is shown in figure 4.14 as a function of the parallel coordinate s for various values

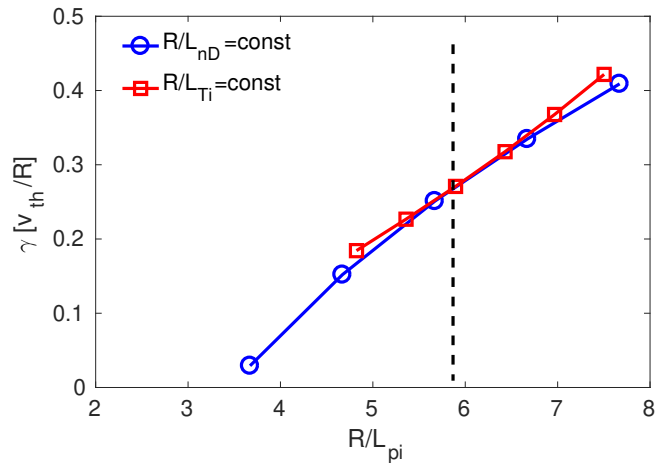


Figure 4.11 – Growth rate as a function of the main ion pressure gradient for the most unstable mode $k_{\theta}\rho_i = 0.35$. Blue (open circle) curve for the case when the main ion density gradient (R/L_{nD}) is constant and the main ion temperature gradient (R/L_{Ti}) is varied, (red square) represents the case when the main ion temperature gradient is constant and the main ion density gradient is varied. The vertical (dotted) line indicates the experimental pressure gradient.

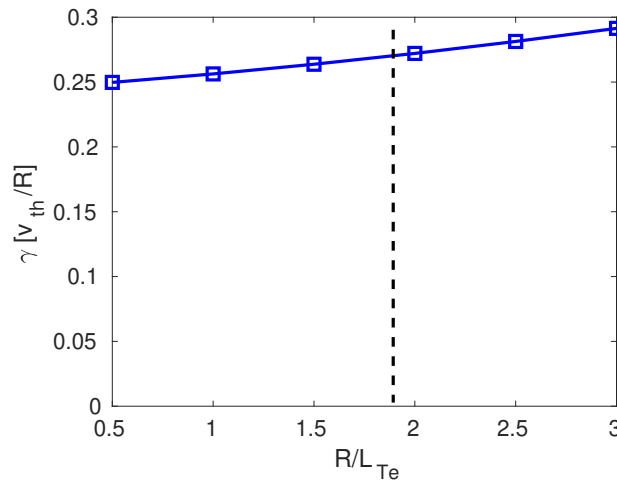


Figure 4.12 – Growth rate as a function of the normalized electron temperature gradient for the most unstable mode $k_{\theta}\rho_i = 0.35$ at $\rho = 0.15$.

of the magnetic shear with the nominal value of β_e . The mode extension along the field line gets reduced as the magnetic shear is increased.

A plasma beta β_e scan is then performed for three magnetic shear values, and the respective growth rates and mode frequencies are shown in figure 4.15. When electromagnetic effects are absent ($\beta_e = 0$), $\gamma = 0$, hence there is no electrostatic instability present. When the beta is increased, there is no instability until a threshold in beta is reached. Above the β_e threshold, the mode growth rate increases with the β , and after a sharp jump at the threshold, the mode frequency slowly decreases.

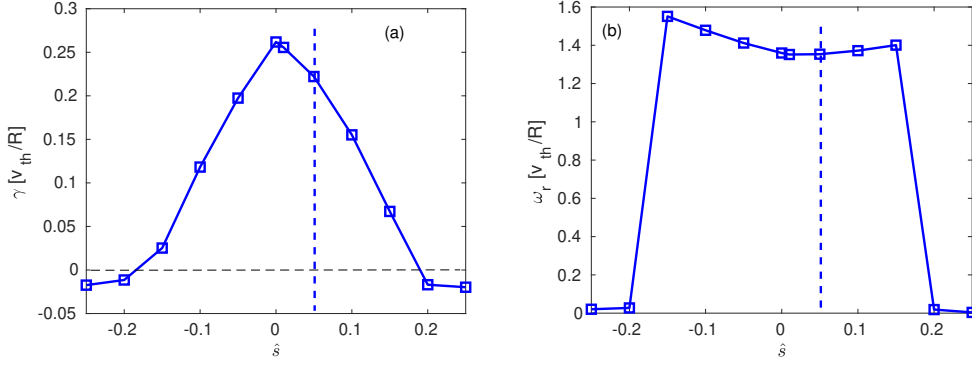


Figure 4.13 – Linear growth rate (a), and mode frequencies (b) as a function of magnetic shear \hat{s} for the most unstable mode $k_{\theta}\rho_i = 0.35$ at $\rho = 0.15$.

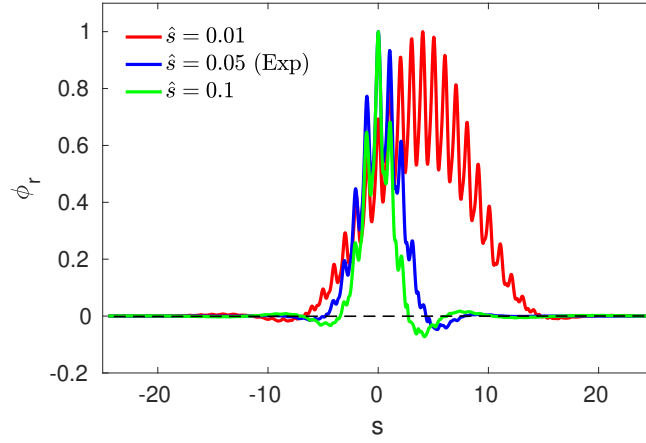


Figure 4.14 – Parallel mode structure of ϕ as a function of parallel coordinate s for three different values of magnetic shear \hat{s} for the most unstable mode $k_{\theta}\rho_i = 0.35$ at $\rho = 0.15$.

The threshold in β increases with the magnetic shear consistently with figure 4.7. Thus, the low magnetic shear in the core of these hybrid plasmas results in a low β threshold.

4.3.2 The role of the pressure gradient β'

An important parameter responsible for the stabilisation of core micro-instabilities is the pressure gradient, $\beta' \sim dp/dr$, correction to the curvature drift (see Eq. 3.9). Its impact has been examined by varying β' and keeping fixed the kinetic species gradients and the other magnetic equilibrium parameters. This is equivalent to an α scan for an $s - \alpha$ equilibrium, where $\alpha = -R_0 q^2 \beta'$. As seen from the comparison of Table 4.1 and 4.3, a β' scan differs from the self-consistent calculation of the magnetic equilibrium since in that case, the Shafranov shift is also modified. As shown in Fig. 4.16, increasing $|\beta'|$ has a strong stabilizing impact on the mode as expected due to the interchange nature of the KBM.

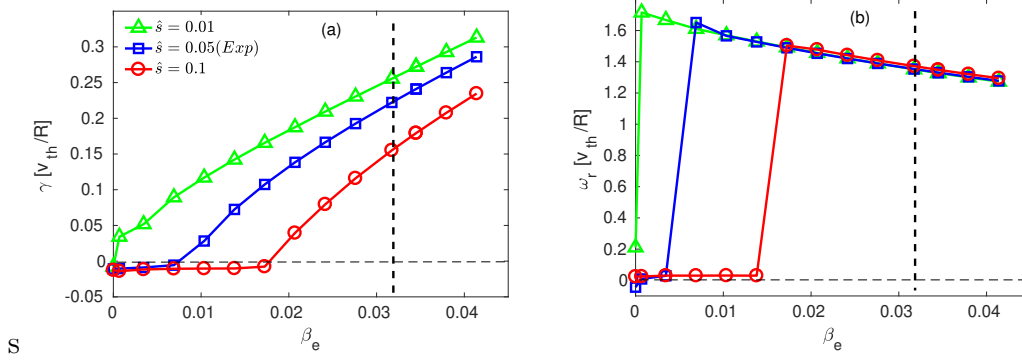


Figure 4.15 – β_e scans for various values of \hat{s} , for the most unstable mode $k_{\theta}\rho_i = 0.35$. The left panel (a) shows the linear growth rates and the right panel (b) shows the corresponding frequencies for the most unstable mode. The blue curve is for experimental value of \hat{s} and vertical (dotted) line represents the corresponding nominal value of β_e (3.2%).

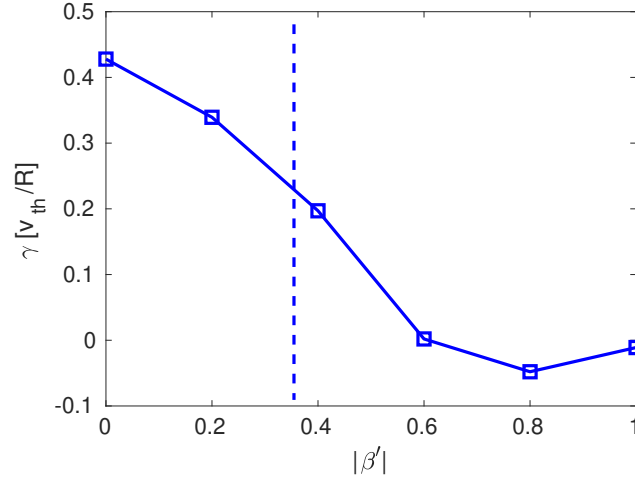


Figure 4.16 – Growth rate as a function of $|\beta'|$, for the most unstable mode at $\rho = 0.15$ and $k_{\theta}\rho_i = 0.35$. The vertical dotted line indicates the nominal value of $|\beta'|$.

4.3.3 Impact of T_e/T_i ratio and safety factor q

Now, the impacts of the T_e/T_i ratio and safety factor q on the mode growth rate are examined. A scan of the T_e/T_i ratio is plotted in figure 4.17, showing that an increase of T_e/T_i leads to a moderate increase of the mode growth rate.

The growth rate and frequencies for the q -profile scans are illustrated in figure 4.18. The mode growth rate is found to be maximum around the experimental values $q \sim 1$ (shown with vertical line), as also pointed out in [35]. However, KBM remains the dominant instability within the range of q variations considered here with decreased growth rate as q increases above its experimental value. For low q values growth rate of KBM increases as q increases as expected since β_{crit} decreases as q increases.

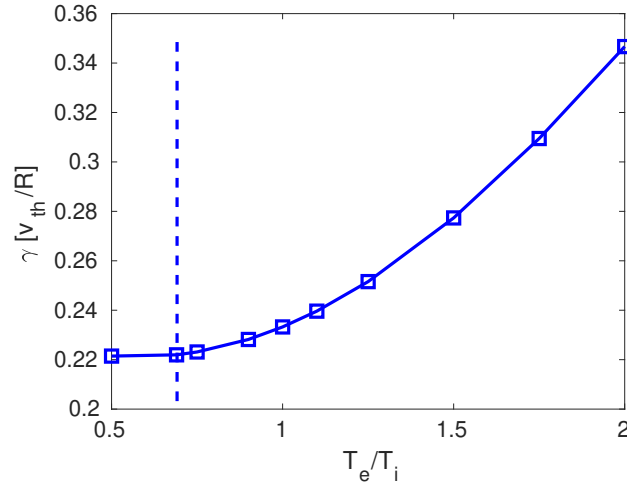


Figure 4.17 – Growth rate as a function of T_e/T_i , for $k_\theta \rho_i = 0.35$. The vertical dotted line indicates the nominal value of T_e/T_i .

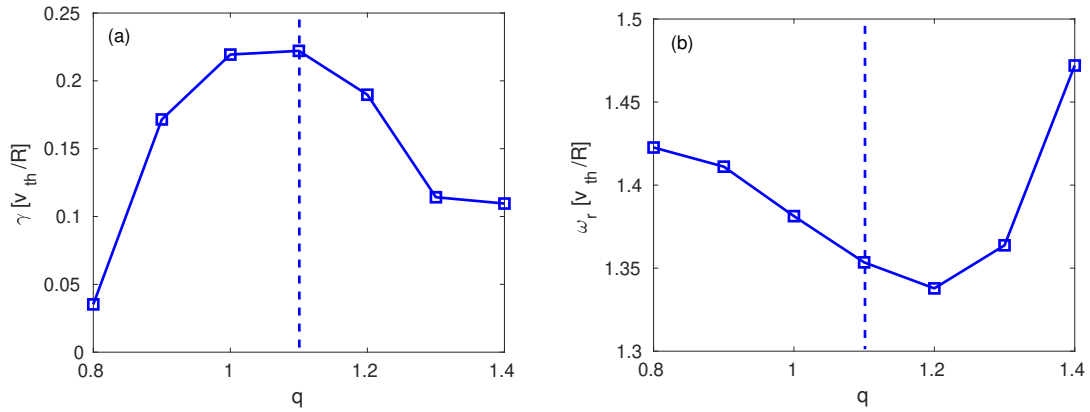


Figure 4.18 – Growth rates (a), and frequencies as function of q -profile, for $k_\theta \rho_i = 0.35$. The vertical dotted line indicates the nominal value of q .

4.3.4 Additional parameter scans

Scan of toroidal rotation (u) and its gradients (u')

In this section, the impact of toroidal rotation and its gradient on the KBM growth rates are discussed.

Two scans in u are performed one where the toroidal rotation gradient is set to zero $u' = 0$ (red curve) and for the other the nominal value $u' = 0.59$ is kept (blue curve), as plotted in the figure 4.19. The toroidal rotation has a moderate impact ($< 10\%$) on the KBM mode growth rate.

A scan over the toroidal rotation gradients u' has been performed for a fixed value of u and is shown in figure 4.20. The toroidal rotation gradient u' has a significant effect on the stability of KBM mode growth rate for the nominal value of u and surprisingly has no impact on the growth rate (red curve) when u is set to

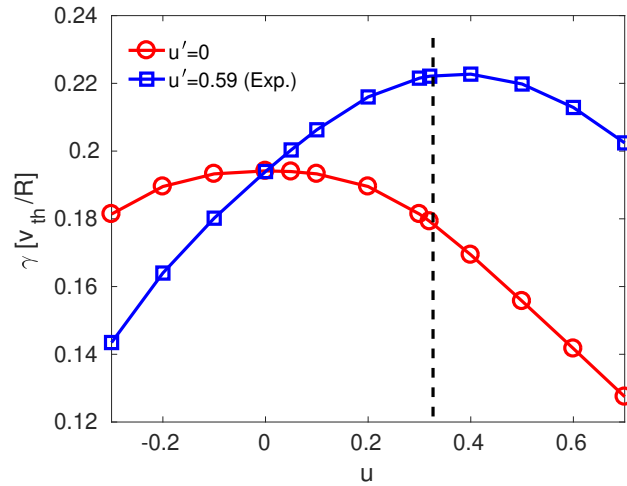


Figure 4.19 – Growth rates as function of the toroidal rotation velocity u for fixed values of the toroidal rotation gradient u' , for $k_{\theta}\rho_i = 0.35$. The blue curve shows the case with the nominal value of $u' = 0.59$ and the red curve corresponds to $u' = 0$. The vertical dotted line indicates the nominal value of u .

zero. This may be due to the existence of cross-terms proportional to u and u' that affect the linear stability, as discussed in [97] for the ITG.

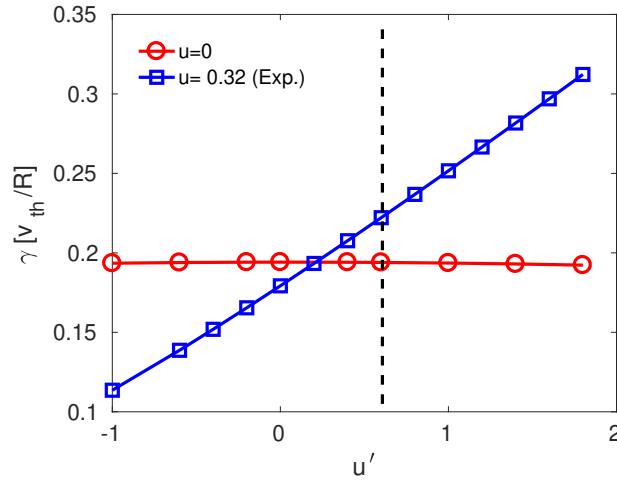


Figure 4.20 – Growth rates as function of the toroidal rotation gradient u' for fixed value of toroidal rotation velocity u , for $k_{\theta}\rho_i = 0.35$. The blue curve shows the case with the nominal value of $u = 0.32$ and the red curve corresponds to $u = 0$. The vertical dotted line indicates the nominal value of u' .

Impact of collisions and impurity

The presence of impurities in the plasma can strongly lower the fusion reaction rate and lead to difficulties in achieving high-performance plasmas. The light impurities such as Carbon (C) are fully ionized in the plasma at fusion temperatures. In contrast,

the heavy elements such as W mainly increase radiation losses of the plasma. The deleterious effect of the various elements depends on the charge of the impurity species.

The impact of Carbon impurity on the growth rate is studied by performing $k_\theta \rho_i$ scans, as illustrated in figure 4.21. In this figure, the red curve shows the case when C impurity is neglected in the simulations and collisions are included. The green line corresponds to the case when both collisions and impurities are excluded in the simulation. These results are compared with a standard case with nominal parameters, including collisions and impurities in the simulations (the blue curve). The effects of collisions and impurities have negligible effects on mode growth rates and frequencies.

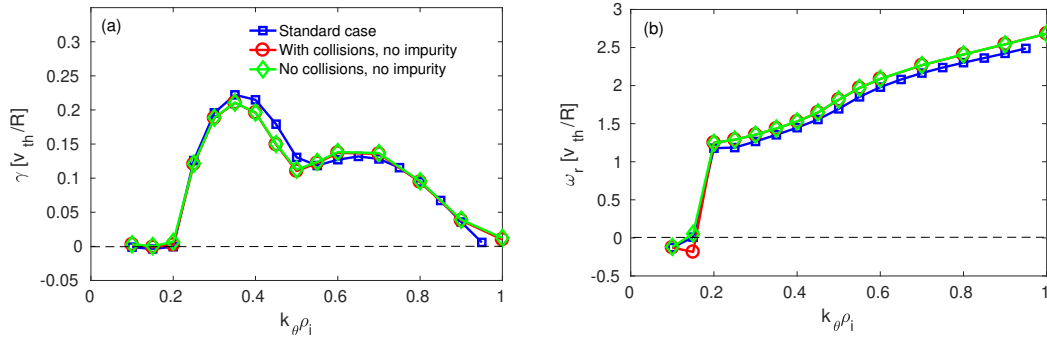


Figure 4.21 – Growth rate (a) and frequency (b) as function of $k_\theta \rho_i$. The blue curve represents the standard case, the red curve corresponds to the case where collisions are retained and Carbon impurity is neglected in the simulations and the green curve where both C impurity and collision are neglected in the simulations.

4.3.5 Identification of unstable mode as KBM

To summarise, the most unstable mode at $\rho = 0.15$ propagates in the ion magnetic drift direction with a real frequency much larger than the growth rate. The mode is driven by the ion pressure gradient and has an even (respectively odd) parity of the eigenfunction in ϕ (respectively A_\parallel) with an extended mode structure at low magnetic shear. Above a critical value β_e^{crit} , the mode is destabilized and its growth rate increases with β_e . In addition, the mode is stabilised at high magnetic shear and high $|\beta'| \sim \alpha$, as observed in [61] for KBMs. The stabilizing effect of $|\beta'|$ is expected for ballooning modes as it reduces the curvature drift. All these features lead to the identification of this mode as a KBM, consistently with [35]. Note that due to the low magnetic shear value, the MHD ballooning limit is relatively low $\beta_{MHD}^{crit} = 0.26\%$ (value at nominal parameters) and the threshold for the KBM is higher than the MHD ballooning limit, $\beta_e^{crit} > \beta_{MHD}^{crit}$, as observed at low R/L_{Ti} in [92].

The presence of this unstable mode has already been detected in global gyrokinetic simulations [35, 58], however, by retaining the global profile variations a significant reduction of the mode growth rate was found previously.

As discussed in section 2.1.3.1 KBMs are also referred to as shear-Alfvénic ion temperature gradient modes (AITG) [57, 58] driven by the finite ∇T_i excited due to wave-particle interactions with thermal ions.

This section can be concluded by remarking that the destabilization of KBMs at high β , low magnetic shear and higher T_e/T_i ratio suggests that these results are directly relevant for the prediction of inner core transport in ITER scenarios.

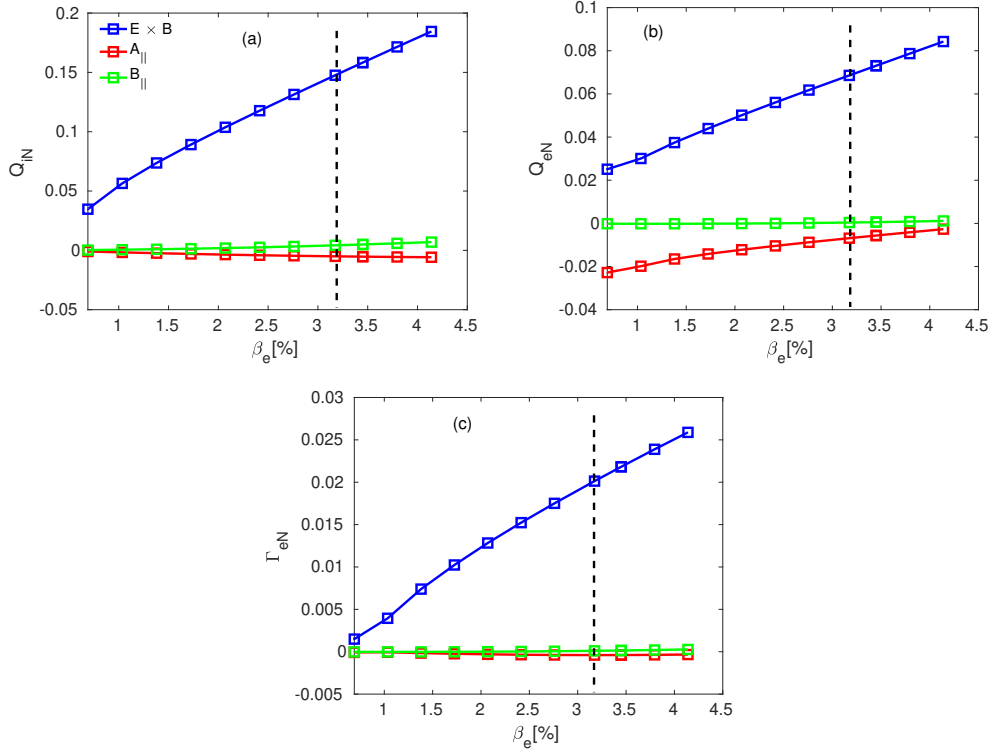


Figure 4.22 – Normalised linear ion and electron heat flux (a) and (b), and electron particle flux (c) as function of β_e for $k_{\theta}\rho_i = 0.35$ at $\rho = 0.15$. The blue curves corresponds to fluxes due to $\mathbf{E} \times \mathbf{B}$ contribution, red due to magnetic flutter (A_{\parallel}) and green due to magnetic compression (B_{\parallel}).

4.4 Linear heat and particle fluxes at $\rho = 0.15$

Following the identification of the dominant unstable modes in the inner core of JET hybrid discharge 75225, we now look at the heat and particle fluxes driven linearly by KBM modes. The normalized linear heat and particle fluxes (as defined in section 4.2) at radial location $\rho = 0.15$ for the β_e scans are presented in figure 4.22. As in figure 4.8 where the normalized linear fluxes were plotted versus β_e at $\rho = 0.33$, the contribution due to the magnetic flutter and compression part to the particle and ion heat fluxes is negligible as compared to the $\mathbf{E} \times \mathbf{B}$ part, so the total linear fluxes are essentially due to electrostatic contribution. Unlike the cases at $\rho = 0.33$, figure 4.8, for the electron heat flux, the contribution due to $\mathbf{E} \times \mathbf{B}$ part and A_{\parallel} part are both important. The magnetic flutter fluxes for the electron heat flux has a negative sign and tends towards zero when β_e increases. Heat and particle fluxes due to $\mathbf{E} \times \mathbf{B}$

contribution for all channels (electron and ion) increase with an increase in β_e . This increase in fluxes is due to linear destabilisation of KBMs at higher β_e as seen in figure 4.15.

Figure 4.23, illustrates the normalized linear heat and particle fluxes for the magnetic shear scans. Similar to the β_e scans, the magnetic flutter electron heat flux is non-negligible and inward for the magnetic shear scans. The heat and particle fluxes for both ion and electron channel decrease with an increase in absolute values of magnetic shear $|\hat{s}|$ due to stabilization of KBMs at high $|\hat{s}|$ as seen in figure 4.13.

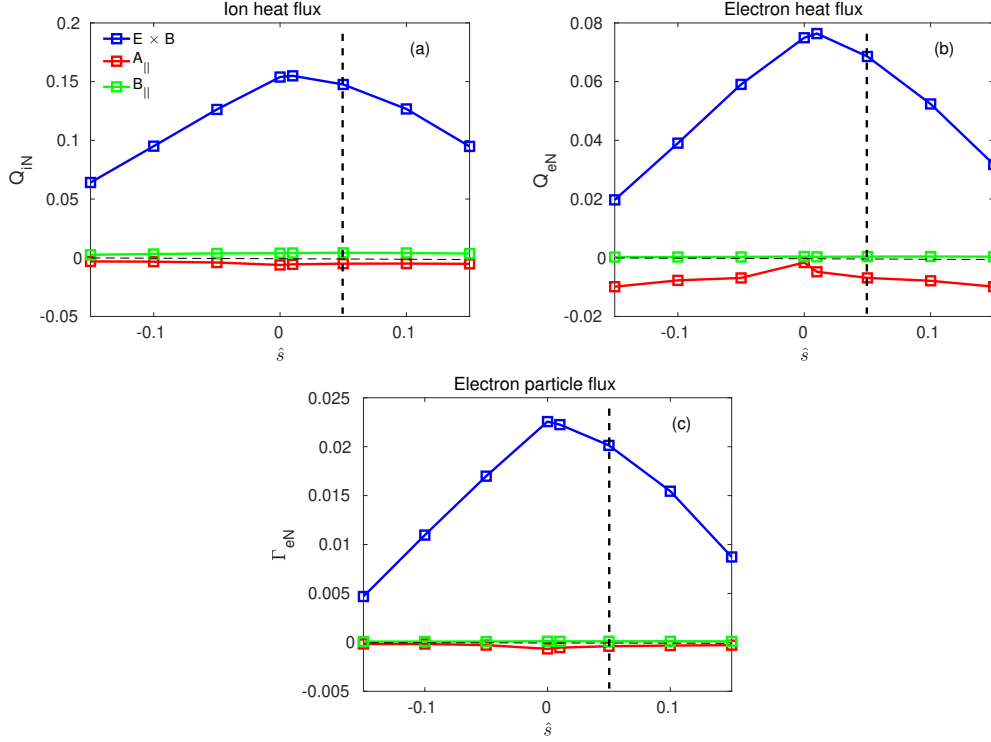


Figure 4.23 – Normalised linear ion and electron heat flux (a) and (b), and electron particle flux (c) as function of \hat{s} for $k_\theta \rho_i = 0.35$ at $\rho = 0.15$. Same colour coding as in figure 4.22.

4.5 Summary

The main results of the chapter are briefly summarised here

1. Linearly it is found that in spite of lower gradients close to the magnetic axis, the plasma is linearly unstable in the central part $\rho = 0.15$.
2. The pressure-driven instability arising in this region has been identified as a Kinetic Ballooning Mode (KBM). It has an extended poloidal mode structure due to the low magnetic shear. The low magnetic shear and high plasma beta are the main parameters responsible for the destabilization of KBM in this region. The KBM is found to be the most unstable mode in the inner core plasma region up to $\rho = 0.33$, whereas at mid and outer radius, $\rho > 0.4$, ITG is the dominant instability. The β_e

threshold, β_e^{crit} , of KBMs increases across the minor radius mostly due to an increase in magnetic shear that is not fully compensated by the increase in q^2 when moving outwards while the experimental β_e decreases when moving outward.

3. Various parametric dependencies of KBM are studied. The unstable mode has a peaked growth rate at experimental values of $q \sim 1$ and a higher T_e/T_i ratio tends to destabilize the modes. The toroidal rotation has a small impact on the KBM mode growth rate. However, an increase of the toroidal rotation gradient tends to increase the mode growth rate only, provided $u \neq 0$. Carbon impurities and collisions have a negligible impact on the mode growth rate.

4. The linear heat and particle fluxes are mostly carried by the $\mathbf{E} \times \mathbf{B}$ convection with a small inward contribution from magnetic flutter for the electron heat flux.

In the next chapter, non-linear GKW simulations will be performed and the non-linear fluxes compared to quasi-linear predictions.

5

Nonlinear gyrokinetic simulations and test of the quasi-linear approximation

In the previous chapter, the linear stability of the central region of the JET hybrid H-mode 75225 discharge at 6-6.5 s has been studied showing that KBMs are linearly unstable in this region. The linear simulations provide insight about KBM stability and its dependence on various physical parameters. However, understanding the nonlinear saturation of KBM turbulence and the resulting transport is required. Moreover, to validate the present available reduced quasi-linear turbulent transport models, their predictions need to be compared to simulated nonlinear heat and particle fluxes.

In this chapter, gyrokinetic simulations are performed in order to compute the level of turbulent transport driven by KBM modes for the selected JET 75225 discharge at $t = 6.0 - 6.5$ s and at $\rho = 0.15$ in the nonlinear regime. The parametric dependence scans for plasma beta and magnetic shear confirm the destabilisation of KBMs with higher β and stabilisation with higher magnetic shear.

The quasi-linear approximation is also tested in the inner core of the selected discharge. Computed quasi-linear fluxes due to KBM turbulence have been compared with nonlinear simulations.

5.1 Non-linear simulations at $\rho = 0.15$

The simulations are performed with $N_{\text{mod}} = 16$ binormal modes and $N_x = 509$ radial modes with a perpendicular box size of $[L_{\text{radial}}, L_{\text{bi-normal}}] = [126, 83]$ in units of ion Larmor radii. The poloidal wave vectors range from $k_{\theta}\rho_i = 0.1$ to 1.5 and the radial wave vectors extend up to $k_r\rho_i = \pm 12.3$. The high value of N_x was required to capture the elongated mode structures at low magnetic shear. A rather small time

step of $\Delta t = 1.5 \times 10^{-4} (R_0/v_{thi})$ was required to guarantee numerical stability in these high beta simulations. The other simulation parameters, briefly summarized in Table 5.1, are the same as described earlier in chapter 4: ion, electron and carbon as kinetic species, no kinetic fast ions, magnetic equilibrium with fast ion pressure, inter-species collisions with $Z_{eff} = 1.74$, no $\mathbf{E} \times \mathbf{B}$ shearing ($\gamma_E = 0$), with parallel velocity gradient drive and inertial effects (Coriolis and centrifugal forces). Even though the kinetic fast ions have a stronger effect linearly on the KBM instability, these are not included in nonlinear simulations for simplicity.

Table 5.1 – Normalized input parameters used in GKW simulations for the nonlinear gyro-kinetic simulations at $\rho = 0.15$. For the detailed list see table 4.1.

ρ	$\frac{R}{L_{Ti}}$	$\frac{R}{L_{Te}}$	$\frac{T_e}{T_i}$	$\frac{R}{L_{ne}}$	$\frac{n_C}{n_e}$	β_e [%]	\hat{s}	q	Z_{eff}	ν	u	u'	γ_E
0.15	4.23	1.99	0.69	1.51	0.01	3.19	0.05	1.1	1.74	0.015	0.32	0.59	0

The time trace of the normalised nonlinear electron and ion heat fluxes for the experimental input values of magnetic shear and plasma beta is presented in figure 5.1. The heat, particle and momentum fluxes are normalized as: $Q_{N,s} = \frac{Q_s^r}{n_s T_s \rho_*^2 v_{thi}}$, $\Gamma_{N,s} = \frac{\Gamma_s^r}{n_s \rho_*^2 v_{thi}}$, $\Pi_{N,s} = \frac{\Pi_s^r}{m_s n_s v_{ths} \rho_*^2 v_{thi}}$, where $\rho_* = \rho_i/R_0$ is the normalized Larmor radius. The fluxes are decomposed into $\mathbf{E} \times \mathbf{B}$ (blue), magnetic flutter (red) and magnetic compression (green) contributions. Horizontal dotted lines illustrate the corresponding time averages with the same colour coding as in the left figure. As seen here, the ion heat flux is dominated by the $\mathbf{E} \times \mathbf{B}$ contribution, with almost negligible contributions from the magnetic flutter and magnetic compression, consistently with the linear fluxes ratio, see Fig. 5.7. For the electron heat flux, the $\mathbf{E} \times \mathbf{B}$ contribution is still dominant, but the magnetic flutter also contributes significantly. Here, the most striking observation is that the magnetic flutter contribution in the nonlinear phase has an opposite sign (outward convection) and is much larger than that in the linear phase. This point will be further investigated in the section dedicated to the quasi-linear modelling. This suggests that the impact of magnetic flutter component has a crucial impact on the total electron heat transport and cannot be neglected in interpretive transport simulations in the inner core.

The zonal flows (ZFs) are a well-known saturation mechanism for ITG turbulence [98]. To investigate the saturation mechanism in KBM turbulence, the time trace of electrostatic potential $|\phi|$ for the zonal modes (all $k_\theta = 0$ modes) for different radial modes are plotted in figure 5.2 (a). Here, the blue curve represents the lowest k_r modes (k_r^{min}), the red curve for the second-lowest radial mode and the green for the third-lowest mode. In figure 5.2 (b), the amplitudes of the zonal flows are plotted as function of radial modes k_r . The zonal flows are found to have a significant amplitude and the temporal correlation of their evolution with respect to the heat fluxes suggest that they may play a role in the saturation of KBM turbulence. Nonetheless, the presence of other saturation mechanisms cannot be excluded at this stage. To know the impact of zonal flows on KBM turbulence saturation precisely, the interplay between the energy transfer between the zonal modes and drift waves also needs to be

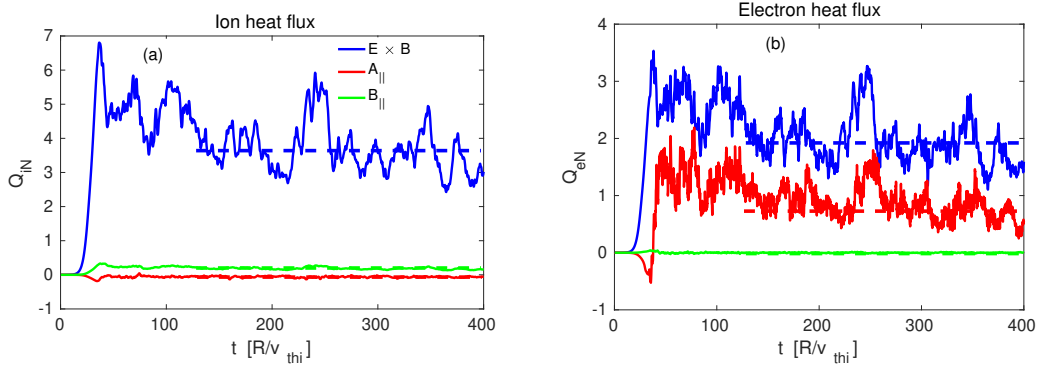


Figure 5.1 – Time trace of nonlinear ion (a) and electron (b) normalised heat fluxes for the JET 75225 discharge at $\rho = 0.15$ for the reference case. The blue curve represents the $\mathbf{E} \times \mathbf{B}$ contribution to the fluxes, the red curve the magnetic flutter contribution (A_{\parallel}) and the green curve the magnetic contribution (B_{\parallel}).

known. This detailed study is out of the scope of the present thesis. Therefore, more work is still required to get a clear picture of the dominant saturation mechanism of KBM turbulence in the central region of these hybrid discharges.

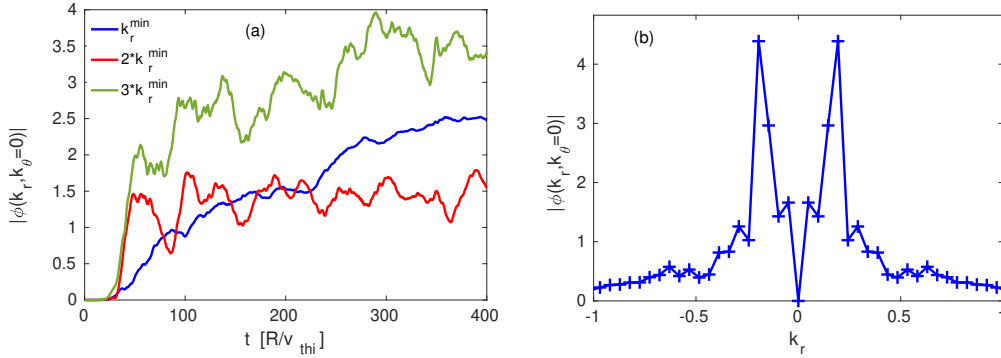


Figure 5.2 – Time trace of flux-surface averaged zonal modes ($k_{\theta} = 0$ modes) for the three lowest radial modes (a) and the amplitudes of zonal modes as function of radial (k_r) modes (b) for the JET 75225 discharge at $\rho = 0.15$ for the reference case.

The electrostatic potential $|\phi|^2$ and vector potential $|A_{\parallel}|^2$ spectra for the reference case at $\rho = 0.15$ are shown in figure 5.3. The spectra is plotted as a function of poloidal wave vector $k_{\theta}\rho_i$ by summing over $k_r\rho_i$ (a) and (b) and radial wave vector by summing over $k_{\theta}\rho_i$ modes (c) and (d). The amplitude of $|\phi|^2$ is much larger than that of $|A_{\parallel}|^2$. The slope of $|\phi|^2$ spectra obtained from these nonlinear simulations are fitted with k_{θ} and k_r exponent, it is found that the k_{θ}^{-3} spectrum when $k_{\theta}\rho_i > k_{\theta}\rho_i^{max}$ and k_{θ}^2 when $k_{\theta}\rho_i < k_{\theta}\rho_i^{max}$ (shown by the magenta and red color in figure 5.3 (a)), where $k_{\theta}\rho_i^{max}$ is the wave vector at which this maximum is reached, reproduces the nonlinear spectra accurately. For radial wave vector, the exponent $k_r^{-3.3}$ represents the best fit for the nonlinear spectra (shown by the green curve in figure 5.3 (c)).

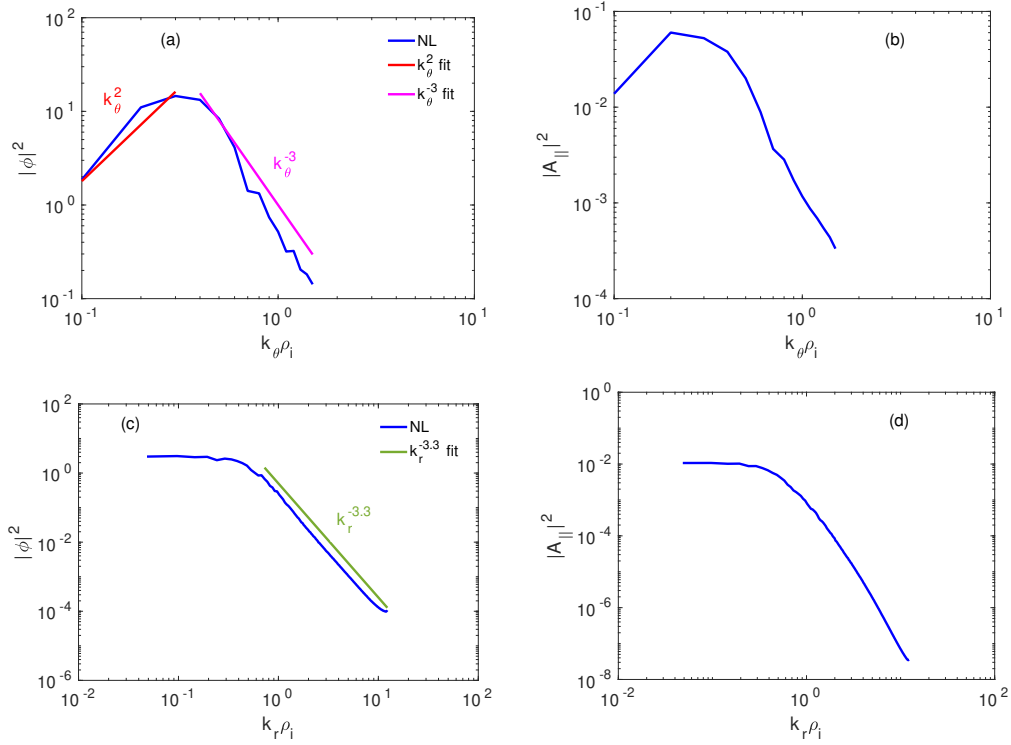


Figure 5.3 – $|\phi|^2$ and $|A_{\parallel}|^2$ spectra as a function of poloidal wave vector $k_{\theta}\rho_i$ (a) and (b) and radial wave vector $k_r\rho_i$ (c) and (d) for the reference case at $\rho = 0.15$. The blue curve represents the nonlinear simulations results, the red and magenta curves are the k_{θ}^2 and k_{θ}^{-3} fit, and the green curve is $k_r^{-3.3}$ fit.

The time-averaged heat, particle and momentum fluxes in physical units are then shown as a function of β_e in figure 5.4. The local value of $\rho_* = 0.0033$ was used for converting the normalised fluxes to SI units at $\rho = 0.15$. The time interval for the temporal average was from 120 and $300R_0/v_{thi}$ for all cases. Here, the total fluxes due to sum of all contributions are indicated by a black line and the $\mathbf{E} \times \mathbf{B}$, magnetic flutter and magnetic compression contributions by coloured dotted lines blue, red and green respectively. All fluxes are observed to increase with increasing plasma beta. For the ion heat transport channel, the fluxes are dominated by the $\mathbf{E} \times \mathbf{B}$ contribution. For the electron heat transport, the magnetic flutter contribution increases with the plasma beta and becomes comparable to the $\mathbf{E} \times \mathbf{B}$ contribution at $\beta_e = 3.8\%$. The higher heat and particle fluxes with β_e in figure 5.4 are qualitatively consistent with the linear destabilization of the KBMs at higher beta seen in figure 4.15. The ion momentum flux shows a similar trend as the particle flux. To calculate the momentum diffusivity, the effective Prandtl number $Pr = \frac{\Pi_{iN}}{Q_{iN}} \frac{R/L_{Ti}}{u'}$ is shown as a function of β_e in figure 5.4 (f). Prandtl number varies slightly ($\sim 3\%$) with increasing beta.

In figure 5.5, the fluxes dependence on the magnetic shear \hat{s} is illustrated in a two-point scan. The nonlinear heat and particle fluxes for both the ion and the electron channel and ion momentum fluxes are reduced with increasing magnetic

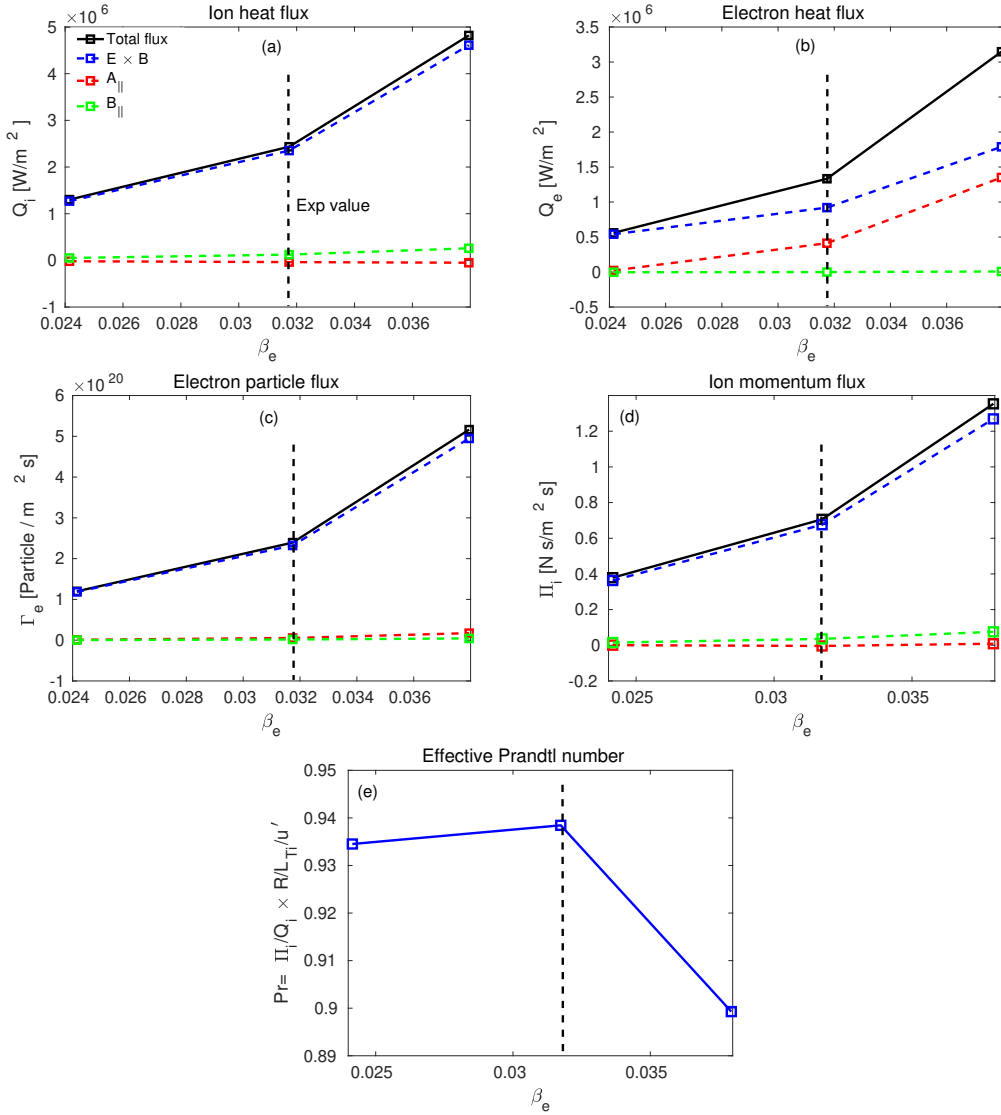


Figure 5.4 – Nonlinear ion heat fluxes (a), electron heat fluxes (b), electron particle fluxes (c), ion momentum fluxes (d) and effective Prandtl number (Pr) (e) as a function of β_e , at $\rho = 0.15$. The solid black line represents the total fluxes. Other colour coding is same as in figure 5.1.

shear, which is also in qualitative agreement with the KBMs stabilisation observed at higher \hat{s} in the linear simulations of figure 4.13.

The quantitative comparison of the nonlinear fluxes with the experimental values would require to include the impact of fast ions, which have been seen to be slightly stabilising linearly in chapter 4 and known to non-linearly stabilise ITG turbulence [36, 99, 77]. The impact of profile shearing effects, which by assumption is not included in the local approximation, has been shown to decrease the linear growth rate of KBM modes in hybrid H-modes [35] and should also be assessed. Finally, a scan in the main KBM drive, R/L_{T_i} and/or R/L_n , would also be required as in any comparison of gradient-driven simulation predictions with the experiments. Such a study is beyond the scope of the present thesis, but it is nevertheless interesting to

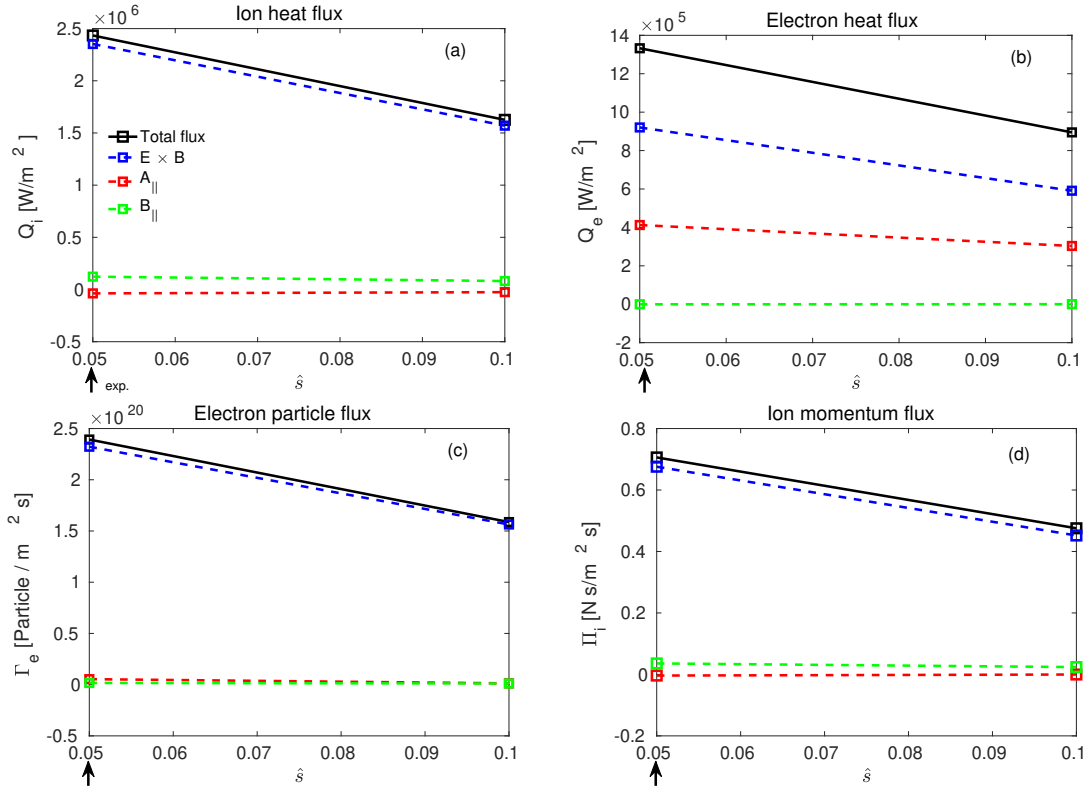


Figure 5.5 – Nonlinear ion heat fluxes (a), electron heat fluxes (b) and electron particle fluxes (c) as a function of magnetic shear \hat{s} , at $\rho = 0.15$. Same colour coding as in fig. 5.1.

give the value of the experimental fluxes for reference. The particle and heat fluxes at $\rho = 0.15$, computed from power balance analysis with CRONOS in [36, 77], are $Q_e = 16 \text{ kW/m}^2$, $Q_i = 47 \text{ kW/m}^2$ and $\Gamma = 3.6 \times 10^{18} \text{ m}^{-2} \text{ s}^{-1}$. The neoclassical ion heat flux, $Q_i^{neo} = 13 \text{ kW/m}^2$, accounts for about a third of the experimental ion heat flux. The computed turbulent fluxes are, however, almost two orders of magnitude larger than the experimental ones, which strongly invites to extend the study and perform a scan in the KBM drives (R/L_n and R/L_{Ti}). The quasi-linear model is used to test the sensitivity of these fluxes to the KBM drives in section 5.3.

5.2 Test of the quasilinear approximation in the inner core

In the last section, nonlinear gyrokinetic simulations of KBM turbulence were presented. The cost of these simulations is too high for extensive parameter scans and use in integrating modelling. As an example the runs for the reference case with $\beta_e = 3.2\%$ shown in figure 5.1 alone required around 1.2 million CPU hours of simulation time to reach up to $t[R_0/v_{thi}] = 600$. Therefore, reduced models are developed for the prediction of heat, particle and momentum fluxes to alleviate the expensive numerical cost of nonlinear simulations [100, 101, 102, 48]. Standard quasi-linear models work reasonably well in the core region, $0.3 \leq \rho \leq 0.7$, though,

their validity still needs to be tested in the inner core $\rho < 0.3$. The purpose of the present section is to test the validity of standard quasi-linear models based on the nonlinear simulations of section 5.1 featuring KBM turbulence in the inner core of the JET 75225 discharge at $t = 6.0 - 6.5$ s and $\rho = 0.15$.

5.2.1 Quasi-linear approximation

The quasilinear approximation assumes that the phase difference between fluctuating fields (e.g. n and ϕ for the $\mathbf{E} \times \mathbf{B}$ particle flux) is similar in the linear and the non-linear regimes. This is usually observed for ITG and TEM turbulence and was more recently shown to also be valid for KBM turbulence [95]. When this approximation holds, the quasi-linear fluxes can be computed as [48, 33]:

$$Q_{s,\mathbf{E} \times \mathbf{B}}^{\text{QL}} = \sum_{k_r, k_\theta} Q_{s,\mathbf{E} \times \mathbf{B}}^N \mathcal{A}_{\text{QL}}^2, \quad (5.1)$$

$$Q_{s,A_\parallel}^{\text{QL}} = \sum_{k_r, k_\theta} Q_{s,A_\parallel}^N \mathcal{A}_{\text{QL}}^2, \quad (5.2)$$

where the first term on the right-hand side is the flux surface average linear flux normalised to the mode amplitude, $Q_s^N = Q_s / \mathcal{A}_L^2$, and the second term is an approximation of the nonlinear saturation amplitude: $\mathcal{A}_{\text{QL}} \sim \mathcal{A}_{\text{NL}}$. This saturated potential is usually constructed based on nonlinear simulations and experimental observations [33, 100].

In linear runs, the mode amplitude is defined as:

$$\mathcal{A}_L(k_r, k_\theta, t) = \sqrt{\int \int [|\phi|^2 + |A_\parallel|^2 + |B_\parallel|^2] ds} / \int ds \quad (5.3)$$

where s is the parallel coordinate and the integral is performed over the full flux-tube domain, i.e. it includes several poloidal turns. In non-linear runs, an extra temporal average is added and the integral in the parallel direction is performed for one poloidal turn only:

$$\mathcal{A}_{\text{NL}}(k_r, k_\theta, t) = \sqrt{\frac{1}{\Delta t} \int \int [|\phi|^2 + |A_\parallel|^2 + |B_\parallel|^2] ds dt} \quad (5.4)$$

with Δt the length of the interval used for the temporal average.

In most quasi-linear models, the linear fluxes are computed at $k_r \rho_i = 0$ only, which is what is done here. We verified in Fig. 5.6 that the KBM growth rate and the linear fluxes vary very little with the radial wave vector.

5.2.1.1 Mixing length model

A common choice for the quasilinear model is to define the saturated mode amplitude based on a mixing length estimate [48]:

$$\mathcal{W}_1 = C_1 \max \left[\frac{\gamma}{\langle k_\perp^2 \rangle}, 0 \right], \quad (5.5)$$

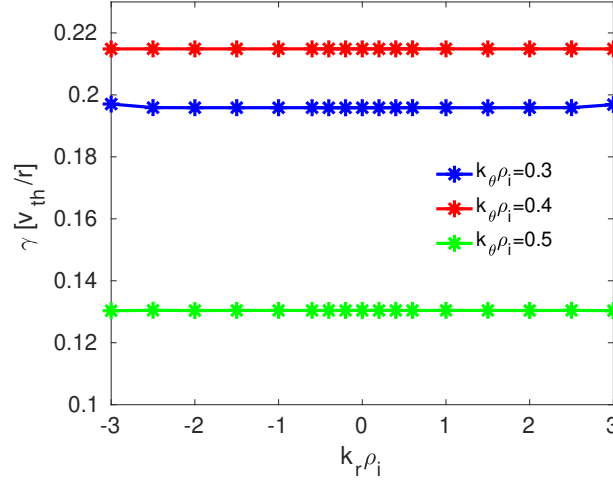


Figure 5.6 – Linear growth rate as a function of radial wave vector ($k_r \rho_i$) for three different values of $k_{\theta} \rho_i$. The blue curve corresponds to $k_{\theta} \rho_i = 0.3$, the red curve for $k_{\theta} \rho_i = 0.4$ and the green represents $k_{\theta} \rho_i = 0.5$.

and assume $\mathcal{A}_{QL}^2 = \mathcal{W}_1$ to compute the quasi-linear fluxes using Eq. (5.1). Here, $\langle k_{\perp}^2 \rangle$ is an effective perpendicular wave vector which takes into account the extended structure of electrostatic potential along the field line and is defined as:

$$\langle k_{\perp}^2 \rangle = \frac{\int k_{\perp}(s)^2 |\phi|^2 ds}{\int |\phi|^2 ds}, \quad (5.6)$$

where the integral is performed along the whole flux tube.

In GKW coordinates, k_{\perp} can be written as:

$$k_{\perp}^2 = k_r^2 g^{rr} + 2k_{\theta} k_r g^{r\theta} + k_{\theta}^2 g^{\theta\theta}, \quad (5.7)$$

where g is the contravariant metric tensor.

The main drawback of this model is that linearly stable modes will never contribute to the quasi-linear fluxes. As it will be seen in the present case, this prevents from capturing the magnetic flutter fluxes at low $k_{\theta} \rho_i$.

5.2.1.2 QuaLiKiz model

Another widely used quasilinear model is the one integrated into QuaLiKiz [33, 103]. In this model, the saturated mode amplitude is approximated by:

$$\mathcal{W}_n = C_n \mathcal{S}_k \max \left[\frac{\gamma}{\langle k_{\perp}^2 \rangle} \right] \frac{1}{k_{\theta} \rho_i^{max}}, \quad (5.8)$$

with spectral form factor S_k given as

$$S_k = \left(\frac{k_\theta \rho_i}{k_\theta \rho_i^{\max}} \right)^{x_n} \quad \text{for} \quad k_\theta \rho_i < k_\theta \rho_i^{\max}, \quad (5.9)$$

$$S_k = \left(\frac{k_\theta \rho_i}{k_\theta \rho_i^{\max}} \right)^{-3} \quad \text{for} \quad k_\theta \rho_i > k_\theta \rho_i^{\max}, \quad (5.10)$$

where the maximum of $\gamma / \langle k_\perp^2 \rangle$ is taken over the $k_\theta \rho_i$ spectrum and $k_\theta \rho_i^{\max}$ is the wave vector at which this maximum is reached. Here, we will test two different spectral shapes: \mathcal{W}_2 and \mathcal{W}_3 with $x_2 = 1$ and $x_3 = 2$, respectively, to highlight the sensitivity of the magnetic flutter fluxes to the spectral rule used at low $k_\theta \rho_i$. \mathcal{W}_2 is the current choice in QuaLiKiz. \mathcal{W}_3 has the values closest to the nonlinear exponent as seen in the nonlinear spectra (figure 5.3). Note that the QuaLiKiz model includes other-dimensional terms that are absorbed in the C_n factor since they do not vary in the present study. The QuaLiKiz model also offers the possibility to account for the contributions of several eigenmodes per wave vector. In the present work, only the contribution from the most unstable modes has been considered.

5.2.2 Linear heat and particle fluxes

In chapter 4, figure 4.22 and 4.23, we have focused on the linear heat and particle fluxes for the most unstable mode $k_\theta \rho_i = 0.35$ only. Here we are investigating fluxes for the whole $k_\theta \rho_i$ range. The linear heat and particle fluxes normalised to the mode amplitude are presented in figure 5.7 as a function of $k_\theta \rho_i$ for the nominal parameters at $\rho = 0.15$. The flux contribution due to magnetic flutter and compression part for particle and heat (electrons, ions) is negligible compared to the $\mathbf{E} \times \mathbf{B}$ part, except at low $k_\theta \rho_i$ modes. At $k_\theta \rho_i = 0.1$, the electron heat flux from magnetic flutter contributions is about 9.4 (this point cannot be seen in the figure 5.7 (b)) and largely exceeds the $\mathbf{E} \times \mathbf{B}$ contribution. The large (normalised) electron heat flux from magnetic flutter is observed in the spectral region where micro-tearing modes are identified in figure 4.4. These micro-tearing modes are linearly stable ($\gamma < 0$) but are nevertheless the modes with the largest growth rate at low $k_\theta \rho_i$ values. The particle flux generated by KBMs in hybrid plasmas are positive (outward) directed with the maximum located at the $k_\theta \rho_i = 0.40$ for the $\mathbf{E} \times \mathbf{B}$ part. The higher heat fluxes as compared to electrons indicates the main channel of transport for KBMs is the ion heat flux.

5.2.3 Comparison of nonlinear and quasi-linear spectra

The non-linear $k_\theta \rho_i$ spectra of ϕ and A_\parallel are compared to the various quasi-linear weights introduced above for different plasma beta and magnetic shear in figures 5.8 and 5.9. Here, figure 5.8 (a) is for $\beta_e = 2.4\%$, (b) for $\beta_e = 3.2\%$, (c) corresponds to $\beta_e = 3.8\%$ at nominal magnetic shear ($\hat{s} = 0.05$) and (d) is for higher magnetic shear $\hat{s} = 0.1$ at nominal beta ($\beta_e = 3.2\%$). The values of $\mathcal{A}_{A_\parallel, NL}^2$ are much lower than that of $\mathcal{A}_{\phi, NL}^2$, but the ϕ and A_\parallel non-linear spectra have a very similar shape. At higher beta, the peak of non-linear spectra are shifted towards low $k_\theta \rho_i$ values, as previously observed in [104]. Note that the non-linear spectra are much less peaked than those

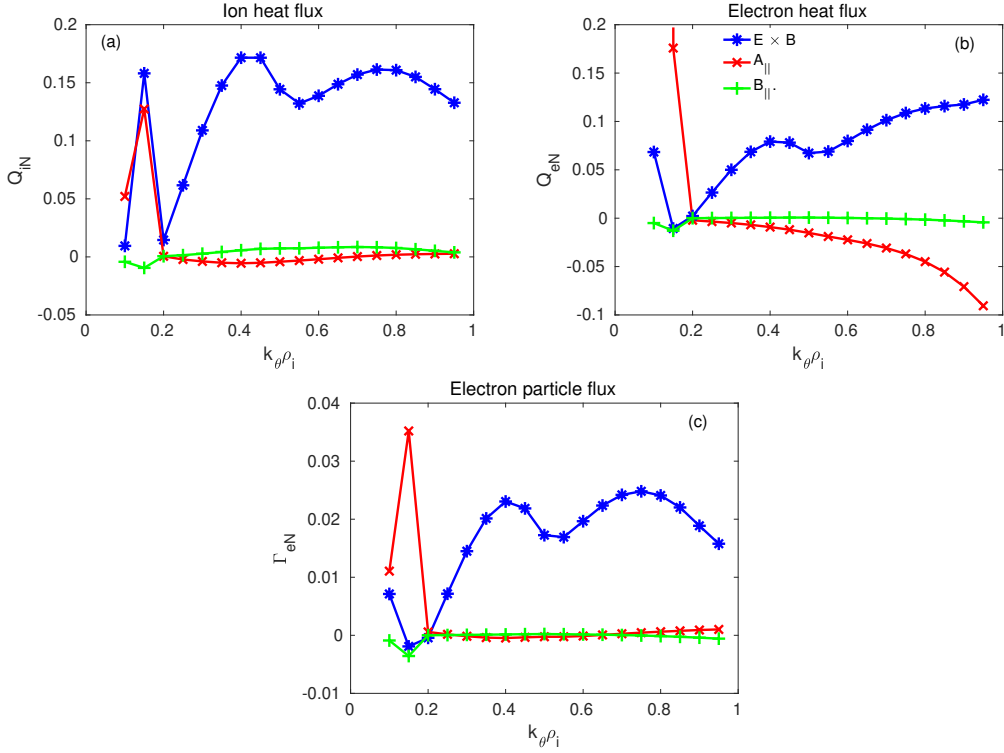


Figure 5.7 – Linear ion (a), electron heat fluxes (b), and particle fluxes (c) normalised with the mode amplitude as a function of $k_\theta \rho_i$, at $\rho = 0.15$. The blue (*) curve corresponds to flux contribution due to $\mathbf{E} \times \mathbf{B}$, the red (x) for magnetic flutter and green (+) for magnetic compression part.

observed in [95] for the Cyclone Base Case at $R/L_{T_e} = 0$ and are more typical of those observed for ITG turbulence. Here, the quasi-linear spectra are normalised to the peak of the nonlinear spectrum to focus on how accurately they reproduce the shape of the nonlinear spectra. As anticipated, the standard mixing length model does not capture the finite amplitude of the fields for $k_\theta \rho_i < 0.3$ since all linear modes are stable in this region. The QuaLiKiz-like model performs much better to this respect, especially the \mathcal{W}_3 variant. All models fail to capture the variation of the spectral width and peak location with β .

5.2.4 Comparison of quasi-linear fluxes with non-linear simulations

To finally test the quasi-linear predictions based on the various saturation rules discussed here, the resulting quasi-linear heat, particle and momentum fluxes obtained with the three quasi-linear models \mathcal{W}_1 , \mathcal{W}_2 and \mathcal{W}_3 are now compared with the nonlinear fluxes, using the same $k_\theta \rho_i$ grid as in the nonlinear simulations to compute the normalised linear fluxes. A scalar multiplication factor of $C_1 = 12.4$, $C_2 = 4.24$ and $C_3 = 4.32$ is used to match the computed quasilinear ion heat flux with the non-linear simulations at $\beta_e = 3.2\%$.

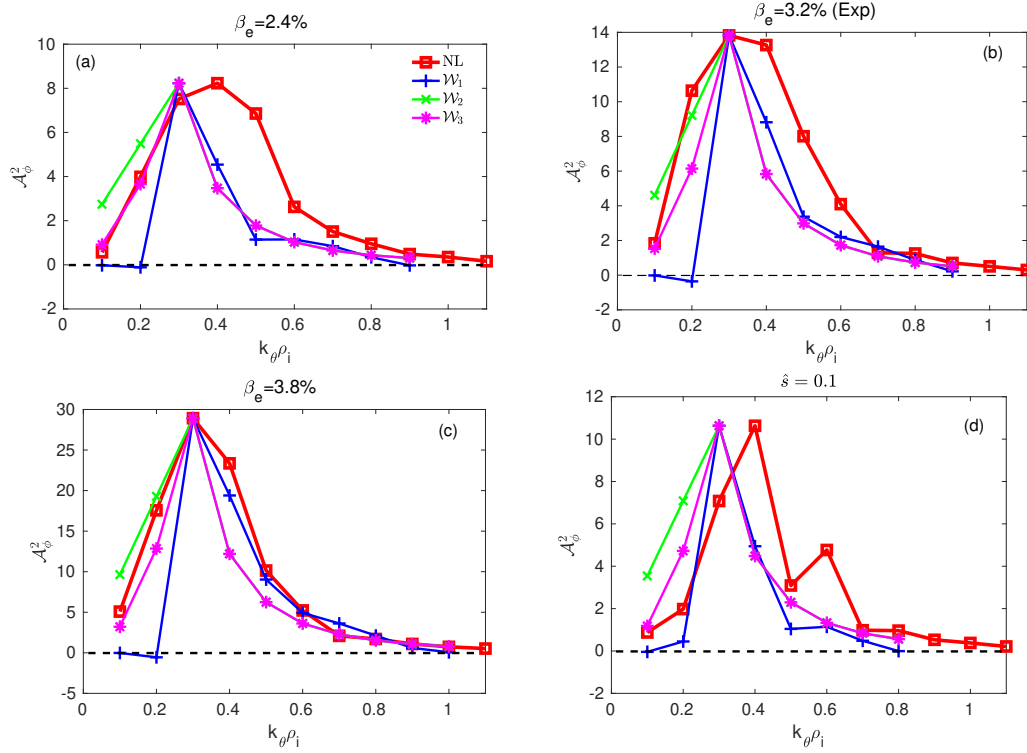


Figure 5.8 – Normalized quasilinear spectra and GKW non-linear saturated electric potential for different plasma beta $\beta_e = 2.4\%$ (a), $\beta_e = 3.2\%$ (b), $\beta_e = 3.8\%$ (c) with nominal magnetic shear ($\hat{s} = 0.05$), and for higher magnetic shear $\hat{s} = 0.1$ at nominal plasma beta ($\beta_e = 3.2\%$)(d) as function of $k_\theta \rho_i$, at $\rho = 0.15$. The quasi-linear spectra are normalized to the maximum of the nonlinear ones. The red curve (square) corresponds to nonlinear, the blue (+) to the quasi-linear model \mathcal{W}_1 , the green (\times) for \mathcal{W}_2 and the magenta (*) for \mathcal{W}_3 .

5.2.4.1 Comparison of $\mathbf{E} \times \mathbf{B}$ fluxes

The corresponding $\mathbf{E} \times \mathbf{B}$ heat, particle and momentum fluxes are plotted in figure 5.10 for the beta scan. As illustrated in figure 5.10 (a), all quasi-linear models yield comparable results for the $\mathbf{E} \times \mathbf{B}$ part of the electron and ion heat fluxes. The general trend of increasing $\mathbf{E} \times \mathbf{B}$ heat flux with β is captured, but the steeper increase at high β is underestimated by 20 to 25% by all models. The same situation is observed for the $\mathbf{E} \times \mathbf{B}$ particle and momentum fluxes, i.e. the increase of the flux with β is well captured at low β but underestimated by some 25% at $\beta_e = 3.8\%$. Quantitatively, the quasilinear particle flux amplitude is underestimated at $\beta_e = 3.8\%$ by $\sim 25\%$ for weight \mathcal{W}_1 and by $\sim 31\%$ for weights \mathcal{W}_2 and \mathcal{W}_3 . For the momentum flux, the \mathcal{W}_3 model performs significantly better than the others.

The comparison is then extended to the magnetic shear scan in figure 5.11. The quasi-linear heat, particle and momentum $\mathbf{E} \times \mathbf{B}$ fluxes decrease with a higher absolute value of magnetic shear, in qualitative agreement with the nonlinear results due to stabilisation of KBM at higher magnetic shear values. Quantitatively, the mixing length model \mathcal{W}_1 performs the worst and underestimates the nonlinear ion heat flux by $\sim 42\%$ and the electron heat flux by $\sim 53\%$ at higher magnetic shear

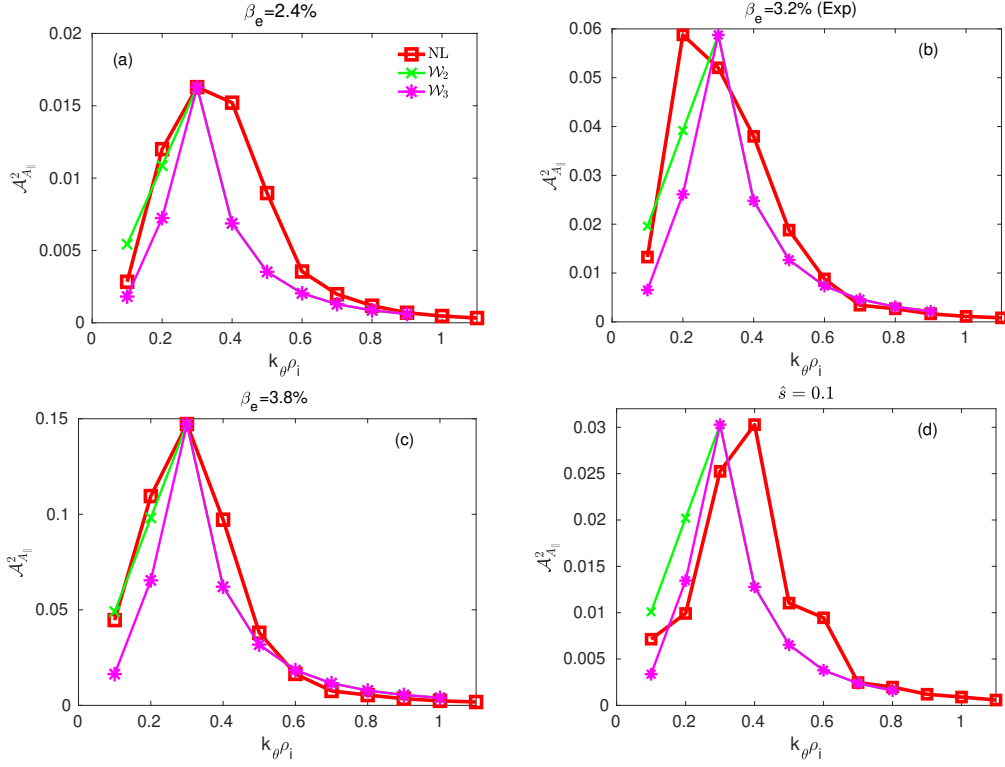


Figure 5.9 – Normalized quasilinear spectra and GKW non-linear saturated vector potential for different plasma beta $\beta_e = 2.4\%$ (a), $\beta_e = 3.2\%$ (b), $\beta_e = 3.8\%$ (c) with nominal magnetic shear, and for higher magnetic shear $\hat{s} = 0.1$ at nominal plasma beta (d) as function of $k_{\theta} \rho_i$, at $\rho = 0.15$. The quasi-linear spectra are normalized to the maximum of the nonlinear ones. The red curve (square) corresponds to nonlinear, the blue (+) to the quasi-linear model \mathcal{W}_1 , the green (\times) for \mathcal{W}_2 and the magenta ($*$) for \mathcal{W}_3 .

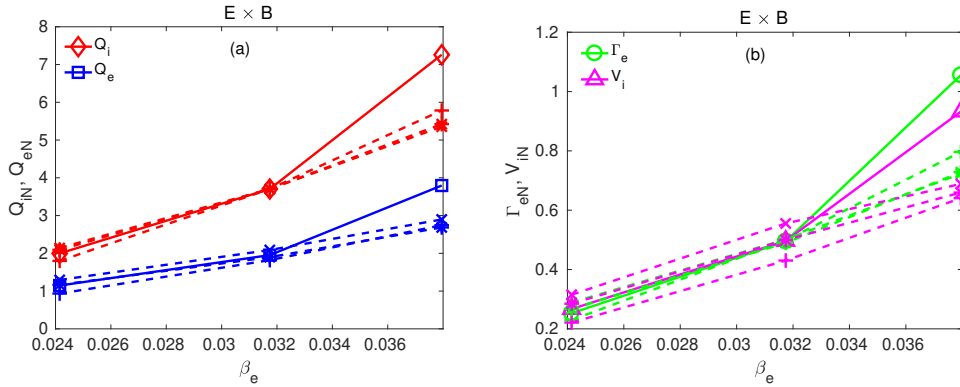


Figure 5.10 – $\mathbf{E} \times \mathbf{B}$ ion and electron heat fluxes (a) and particle and ion momentum flux (b) as a function of β_e , at $\rho = 0.15$. The solid lines are for the non-linear results and the dashed lines for the quasilinear models. The plus signs + corresponds to the QL model \mathcal{W}_1 , the crosses \times are for \mathcal{W}_2 and the star $*$ are for \mathcal{W}_3 .

$\hat{s} = 0.1$. The best results are obtained with the \mathcal{W}_3 model which underestimates the ion heat flux by $\sim 14\%$ whereas it is in good agreement for the electron heat flux at higher magnetic shear. The same trend is obtained for the particle and momentum flux, with \mathcal{W}_3 performing significantly better than the other models.

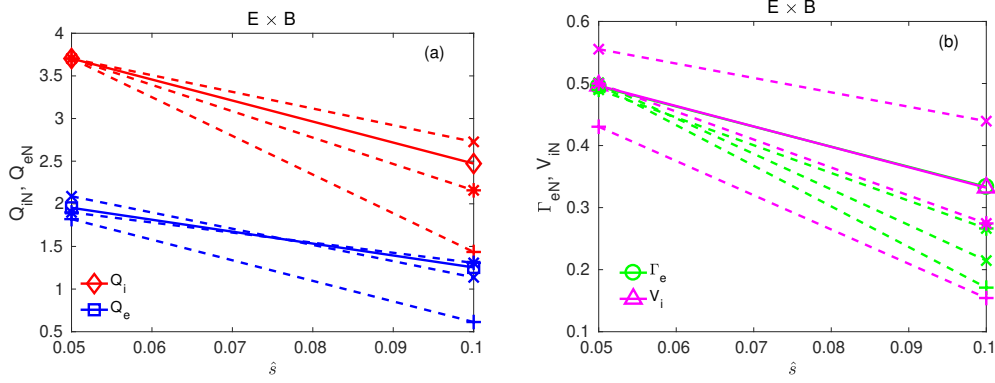


Figure 5.11 – $\mathbf{E} \times \mathbf{B}$ ion and electron heat fluxes (a) and ion momentum flux (b) as a function of the magnetic shear \hat{s} , at $\rho = 0.15$. The solid lines are for the non-linear results and the dashed lines for the quasilinear models. The plus signs + corresponds to the QL model \mathcal{W}_1 , the crosses \times are for \mathcal{W}_2 and the star $*$ are for \mathcal{W}_3 .

5.2.4.2 Comparison of magnetic flutter fluxes

As seen in figure 5.4 and 5.5, the only non-negligible magnetic flutter contribution is to the electron heat flux. Therefore, now we will focus on this channel for the comparison with the quasi-linear models. To start with, we examine the parity of the modes as a function of $k_\theta \rho_i$. The magnetic flutter fluxes obtained with the \mathcal{W}_1 , \mathcal{W}_2 and \mathcal{W}_3 models for the electron are then compared to the non-linear fluxes in Fig. 5.13.

The parity factor is defined as [63]:

$$P_{A_\parallel} = \frac{|\int Re[A_\parallel] ds|}{\int |Re[A_\parallel]| ds} \quad (5.11)$$

The parity factor is zero (A_\parallel is odd) for pure ballooning parity (KBM) and may be as high as one (A_\parallel is even) for tearing parity modes (MTM). Figure 5.12 illustrates the parity factor for the A_\parallel and ϕ fluctuations for the nominal parameters at $\rho = 0.15$. At the lowest $k_\theta \rho_i$, there is a marked increase in the parity factor for A_\parallel and decrease for ϕ , suggesting a nonlinear excitation of the stable MTM at this location.

As illustrated in figure 5.13, for the electron heat flux, the mixing length model \mathcal{W}_1 strongly underestimates the magnetic flutter contribution, as anticipated, since it cannot capture the contribution from the linearly stable micro-tearing modes at $k_\theta \rho_i = 0.1$. In contrast, the \mathcal{W}_2 and \mathcal{W}_3 models strongly overestimate the magnetic flutter heat flux. The factor of 3 difference between the electron heat flux predictions

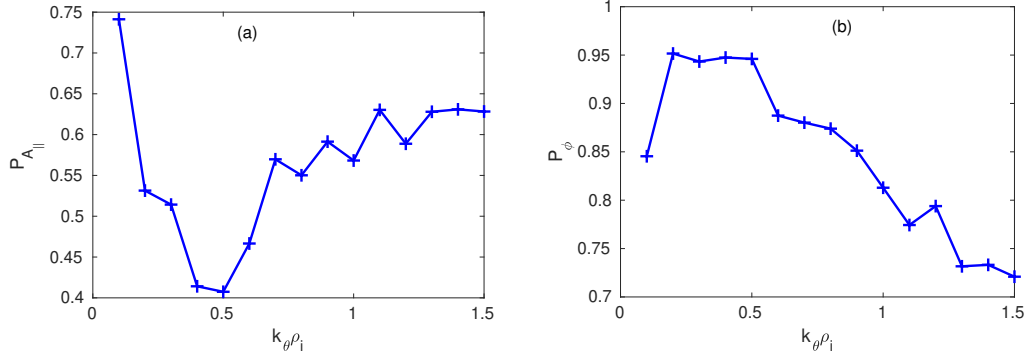


Figure 5.12 – Parity factor for the A_\parallel fluctuations and Φ fluctuations as a function of $k_\theta \rho_i$ in non-linear simulations, at $\rho = 0.15$.

of the \mathcal{W}_2 and \mathcal{W}_3 models highlights the extreme sensitivity to the modeled amplitude at the lower end of the $k_\theta \rho_i$ spectrum.

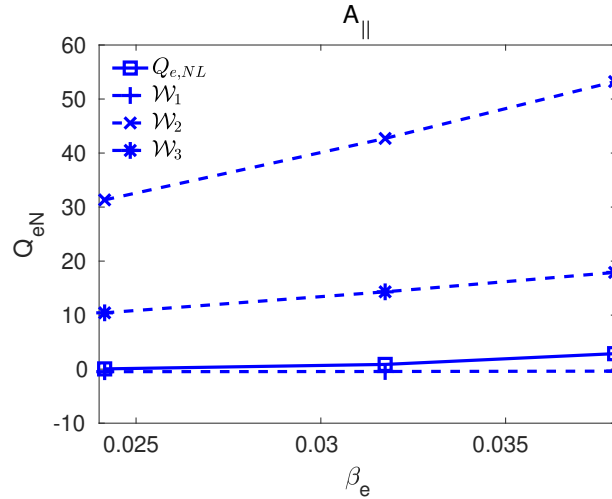


Figure 5.13 – Magnetic flutter electron heat flux as a function of β_e , at $\rho = 0.15$. The solid lines are the non-linear results and the dashed lines are for the quasilinear models. The plus signs + corresponds to QL weight \mathcal{W}_1 , the crosses \times are for \mathcal{W}_2 and the star $*$ are for \mathcal{W}_3 .

To better understand the discrepancy for the electron magnetic flutter part, the ratio of the A_\parallel fluctuations amplitude to the total fluctuation amplitude is shown in figure 5.14 as a function of $k_\theta \rho_i$ for linear and non-linear simulations.

For $k_\theta \rho_i > 0.2$, this ratio is observed to be comparable in linear and non-linear simulations ($\sim 40\%$ difference at $k_\theta \rho_i = 0.9$), but at $k_\theta \rho_i = 0.1$ the linear ratio is more than 10 times larger than the non-linear one. Linearly, the ratio $\mathcal{A}_{A_\parallel}^2 / \mathcal{A}^2$ at low $k_\theta \rho_i$ is governed by the most unstable mode, i.e. micro-tearing modes (MTM) in the present case. Since these modes are linearly stable, the evolution of their amplitude tends to be dominated by the non-linear interactions in the non-linear regime, which results in a much smaller value of $\mathcal{A}_{A_\parallel}^2 / \mathcal{A}^2$ at $k_\theta \rho_i = 0.1$.

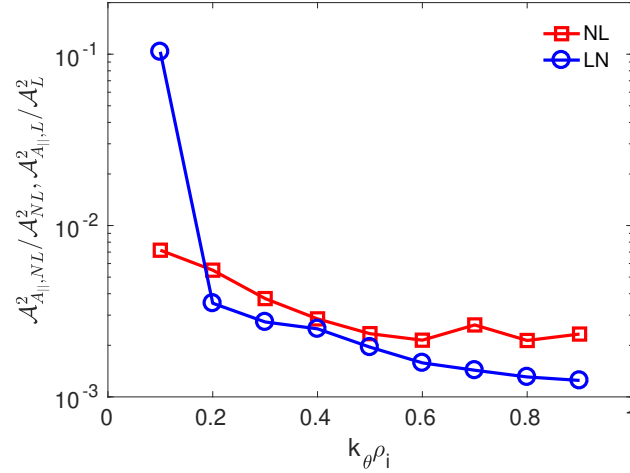


Figure 5.14 – Ratio of the A_\parallel fluctuations amplitude, $\mathcal{A}_{A_\parallel}^2$ to the total fluctuation amplitude \mathcal{A}^2 as a function of $k_\theta \rho_i$ in linear and non-linear simulations, at $\rho = 0.15$.

In an attempt to capture this effect in the QuaLiKiz-like quasi-linear model, an extra normalisation of the magnetic flutter fluxes has been introduced. First, it is assumed that:

$$\frac{\mathcal{A}_{A_\parallel, NL}}{\mathcal{A}_{NL}} \sim \frac{\mathcal{A}_{A_\parallel, L}(k_\theta \rho_i^{max})}{\mathcal{A}_L(k_\theta \rho_i^{max})} \quad (5.12)$$

and then, the following quantity is introduced:

$$A_\parallel^{ratio} = \frac{\mathcal{A}_L(k_\theta \rho_i)}{\mathcal{A}_{A_\parallel, L}(k_\theta \rho_i)} \frac{\mathcal{A}_{A_\parallel, L}(k_\theta \rho_i^{max})}{\mathcal{A}_L(k_\theta \rho_i^{max})}, \quad (5.13)$$

that is used to renormalise the amplitude of A_\parallel in the magnetic flutter fluxes based on the assumption in Eq. (5.12):

$$Q_{s, A_\parallel}^{QL} = \sum_{k_\theta} Q_{s, A_\parallel}^N \mathcal{A}_{QL}^2 A_\parallel^{ratio} \quad (5.14)$$

This model will be referred as \mathcal{W}_2^* and \mathcal{W}_3^* and is compared to the non-linear results for beta in Fig. 5.15 (a).

The renormalisation of A_\parallel in the linear magnetic flutter fluxes makes the prediction of the QuaLiKiz-like model for the electron magnetic flutter contribution much closer to the values of the fluxes obtained in the nonlinear simulations, in particular for \mathcal{W}_3^* . The extreme sensitivity to the assumption used for the low $k_\theta \rho_i$ part of the spectrum is again visible when by comparing \mathcal{W}_2^* and \mathcal{W}_3^* : more than a factor of three difference on the magnetic flutter electron heat flux can be obtained with a modest change in the quasi-linear spectrum. The extra normalisation of magnetic flutter part has no impact on the quasi-linear ion heat, particle and momentum parts since the only non-negligible magnetic flutter contribution is to the electron heat flux.

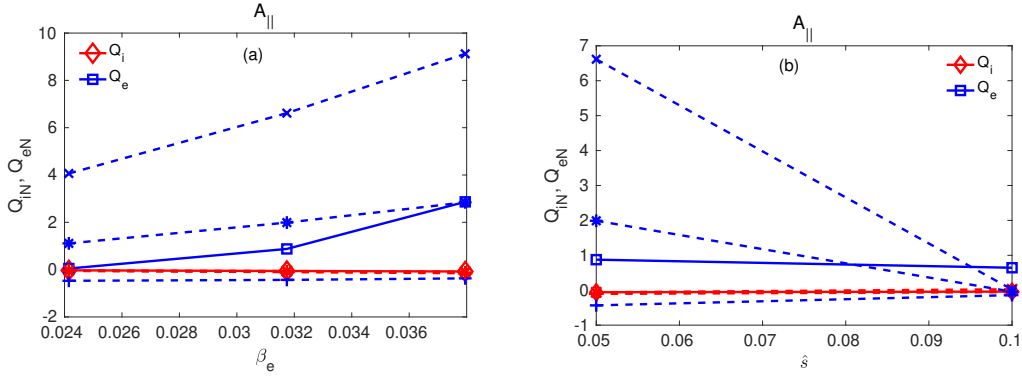


Figure 5.15 – Magnetic flutter ion and electron heat fluxes as a function of β_e (a) and magnetic shear (b) at $\rho = 0.15$. The solid lines are the non-linear results and the dashed lines are for the quasi-linear models. The plus signs + corresponds to the model \mathcal{W}_1 , the crosses \times are for \mathcal{W}_2^* and the star $*$ are for \mathcal{W}_3^* .

The quasilinear electron fluxes for magnetic shear scans due to magnetic flutter contributions with this new normalisation are plotted in figure 5.15 (b). The magnetic flutter contribution to the electron heat flux for \mathcal{W}_2^* is overestimated at $\hat{s} = 0.05$ and underestimated at $\hat{s} = 0.1$. For the QL rule \mathcal{W}_3^* , QL fluxes are overestimated by $\sim 50\%$ at lower magnetic shear and underestimated at higher magnetic shear by more than $\sim 90\%$.

Sub-dominant MTMs and their contribution to magnetic flutter transport is an area of research on its own [105, 63, 106] and it is clear that more work is required to predict the magnetic flutter fluxes in a quasi-linear model accurately. It is nevertheless encouraging to see that once the saturated level of A_{\parallel} is captured, standard quasi-linear models predictions are of the right order of magnitude compared to nonlinear results.

5.3 Sensitivity of the quasilinear ion heat fluxes to input gradients

In this section, the sensitivity of the nonlinear ion heat fluxes to the main KBM drives (R/L_{Ti} and R/L_n) is investigated using the reduced quasi-linear models. The most accurate QL model \mathcal{W}_3 (described in section 5.2) is used to test if variations in input parameter can lead to a significant reduction of predicted turbulent fluxes down to the experimental levels or not. Linear simulations are performed with reduced gradients and corresponding plots are shown in figure 5.16. Here in figure 5.16 (a), the blue curve corresponds to the case with no kinetic fast ions in the simulation, and the red curve is with kinetic fast ions for the nominal value of R/L_{ne} . The red curve in figure 5.16 (b) represents the case with kinetic fast ions and reduced $R/L_{Ti} = 3.2$. Including kinetic fast ions and reducing R/L_{Ti} by 20% with nominal R/L_{ne} decreases the quasi-linear ion heat fluxes by a factor of 10. Further reducing R/L_{ne} by 20% yields quasi-linear ion heat fluxes values close to the experimental power balance heat fluxes values. This shows that the quasi-linear heat fluxes are

extremely sensitive to the main KBM drives and that a reduction of these drive within the experimental uncertainties is sufficient to match the power balance fluxes.

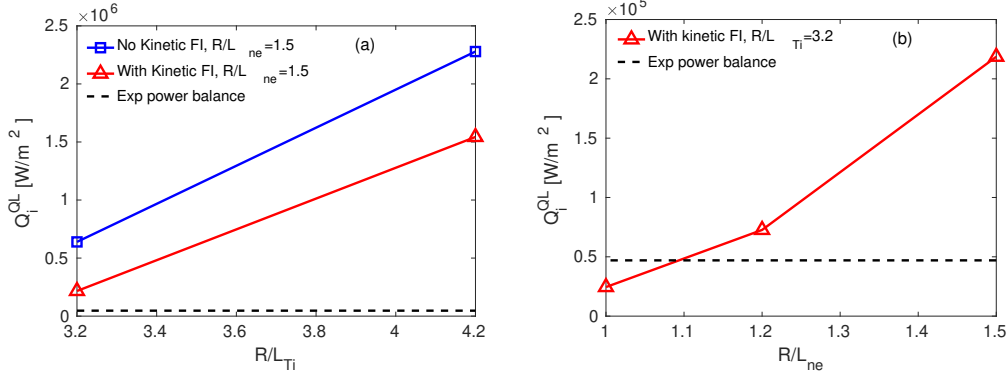


Figure 5.16 – Quasilinear ion heat fluxes for the QL model \mathcal{W}_3 as a function of R/L_{Ti} for the nominal value of R/L_{ne} (a) and R/L_{ne} with kinetic fast ions and $R/L_{Ti} = 3.2$ (b) at $\rho = 0.15$. The blue curve is for the case without kinetic fast ions and nominal value of $R/L_{ne} = 1.5$ and the red curve is for the case with kinetic fast ions.

5.4 Summary

To summarise this chapter, the quasi-linear ion and electron heat fluxes, particle and momentum fluxes estimation for three different QL models are found in reasonable agreement with nonlinear fluxes amplitude for the $\mathbf{E} \times \mathbf{B}$ contribution with some departure at higher beta and high magnetic shear, especially for the basic mixing length model (\mathcal{W}_1).

For the magnetic flutter contribution to the electron heat flux, which represents about half of the total electron heat flux, capturing the contribution of linearly stable micro-tearing modes excited in the nonlinear regime is essential. This proves to be a difficult exercise, extremely sensitive to the exact value of the saturated A_{\parallel} values at low $k_{\theta}\rho_i$. The QuaLiKiz-like mixing length model (\mathcal{W}_3^*) yields the best results, even though further improvements would be desirable to capture both the β_e and \hat{s} impacts. Reducing the KBM drives R/L_{Ti} and R/L_{ne} by about 20% and including kinetic fast-ion strongly reduces the quasi-linear in heat flux to the point where it matches with the experimental value.

6

Conclusions and future perspective

Accumulation of tungsten (W) in the plasma central region is a key issue which can limit the performances of the present as well as future fusion devices such as ITER. Tungsten accumulation in the central part of ITER ($\rho < 0.3$) is expected to be determined by neoclassical and turbulent processes. Understanding turbulent transport in this region is crucial to predict the turbulent W fluxes and the background plasma profiles which determine W neoclassical transport. Predicting core transport in the region $\rho < 0.3$ is also very important for the fusion reaction rate. In this thesis, the available reduced transport models that can be applied to ITER are tested based on existing plasma discharges of the JET tokamak.

To better characterise turbulent transport and to test the quasi-linear approximation in the central region close to the magnetic axis, a linear gyro-kinetic investigation has first been carried out for JET high- β MHD-free hybrid H-mode discharge 75225 in the time interval $t = 6.0 - 6.5s$ at $\rho = 0.15$ as well as on other radial locations using the gyrokinetic code GKW in the local approximation. The role of MHD activity that was not present in these selected hybrid discharges can be crucial in the central region, especially in baseline scenarios with $q < 1$ and sawteeth. In spite of lower gradients close to the magnetic axis, the plasma is found linearly unstable. The pressure-driven instability arising in this region has been identified as a Kinetic Ballooning Mode (KBM) with an extended mode structure along the magnetic field line in ballooning space due to the low magnetic shear. The low magnetic shear and high plasma beta values are responsible for the onset and destabilisation of KBM in this region. It is found that the low magnetic shear of these hybrid plasmas can lead to a shift of the KBM threshold towards low β_e values. It is also found that the KBM instability dominates up to $\rho = 0.33$. At mid and outer radius, $\rho > 0.4$, ITG becomes the dominant instability. This is due to the fact that the critical beta for the destabilisation of KBMs increases across the minor radius

from $\rho = 0.15$ to $\rho = 0.6$, mostly due to the increased magnetic shear. Furthermore, the impact of kinetic fast ions is always stabilising at all radial locations except at $\rho = 0.33$ where a fast ion driven mode is excited. Including the fast ion pressure in the magnetic equilibrium leads to stabilisation of KBM modes and destabilisation for ITG modes. The higher T_e/T_i ratio leads to an increase of the KBM growth rate. In comparison to the impact of magnetic shear, β or β' , the impact of the electron to ion temperature ratio T_e/T_i and safety factor q is smaller but tend to favour the destabilisation of KBM modes in electron heated plasmas with a q profile just above unity. A scan of toroidal rotation (u) and toroidal rotation gradient (u') indicates that the toroidal rotation has a moderate impact ($< 10\%$) on the KBM mode growth rate but increasing the toroidal rotation gradient significantly destabilises the KBM. The collisions and impurities have negligible effects on the KBM growth rate and frequency.

Non-linearly, the excitation of KBMs drives heat and particle fluxes increasing with higher beta and lower magnetic shear consistently with linear results. Non-linearly, the $\mathbf{E} \times \mathbf{B}$ contribution to the ion heat flux is found to be dominant. For the electron heat flux, the most striking observation is that the magnetic flutter contribution to the nonlinear heat flux is much larger and with an opposite sign to what is observed in linear simulations. This contribution possibly arises from stable micro-tearing modes at $k_\theta \rho_i < 0.2$ that are excited non-linearly. The nonlinear excitation of MTM modes at low $k_\theta \rho_i$ is supported by the parity factor of magnetic fluctuations. Accounting for these micro-tearing modes is necessary to predict the mechanisms for energy and particle turbulent transport in the inner core of high-performance plasmas. The nonlinear heat flux values for electron and ion for nominal parameters at $\rho = 0.15$ are found to be much larger than the experimental power balance values. Additional simulations including kinetic fast ions, background $\mathbf{E} \times \mathbf{B}$ shearing and scans in the main KBM drives (R/L_{Ti} and R/L_n) within the experimental uncertainties are now required to test whether the nonlinear fluxes values can be compatible with the experimental ones.

The validity of standard quasi-linear (QL) models has also been tested for the selected JET discharge. At $\rho = 0.15$, it is found that the quasi-linear fluxes estimates are in good agreement with nonlinear fluxes for the $\mathbf{E} \times \mathbf{B}$ contributions with some departure at high beta. However, these models fail to capture the magnetic flutter contribution to the electron heat flux due to the non-linearly excited micro-tearing modes. An extension of the model used in QuaLiKiz is shown to improve the description of the magnetic flutter contribution, even though further work would be required to obtain a robust model. The QL model was used to test the sensitivity of these fluxes to the KBM drives. A decrease of R/L_{Ti} and R/L_n by about 20% was sufficient to match the experimental fluxes, demonstrating the strong sensitivity of the QL fluxes to the input gradients.

A sizeable level of turbulent transport in the inner core is favourable to avoid W accumulation. Tungsten turbulent diffusion can mitigate the neoclassical inward pinch of W in the inner core and help in preventing W accumulation. This mechanism could be particularly relevant for ITER where the level of neoclassical transport to overcome is low. To test this mechanism, the gyrokinetic analysis has been extended

to the ITER conventional H-mode scenario in DT with 15 MA plasma current and $Q=10$. Reference profiles for this case were obtained from ASTRA simulations using a scaling based transport model for the core and with EPED1+SOLPS pedestal for the H-mode $Hy2, 98 = 1$ [107]. It is found that KBM is also unstable for this predicted ITER H-mode case. Future work will extend this evaluation to other ITER low Q scenarios, such as the $Q = 5$ steady-state one, and will compare turbulent heat and particle fluxes with neoclassical fluxes to predict W accumulation in the inner core of ITER.

A

Simplified dispersion relation for ITG instability

A simplified analytical dispersion relation for ITG instabilities and their physical picture is described in this appendix. Two kinetic and fluid models are used to build the linear dispersion relation to describe the toroidal and slab ITG.

A.1 The δf gyrokinetic equation in the slab-like approximation

A.1.1 Reference gyro-kinetic equation

The starting point is the gyrokinetic equation in the local approximation 3.12, described in chapter 3. In this equation, we neglect the vector potential fluctuations to make the model electrostatic and further neglect the Coriolis, centrifugal term, parallel rotation gradient, and β' correction to the curvature drift.

After these assumptions the gyrokinetic equation is

$$\frac{\partial f}{\partial t} + (v_{\parallel} \mathbf{b} + \mathbf{v}_{\mathbf{D}} + \mathbf{v}_{\mathbf{E}}) \cdot \nabla f - \frac{\mathbf{b}}{m} \cdot (\mu \nabla B) \frac{\partial f}{\partial v_{\parallel}} = S, \quad (\text{A.1})$$

where S is given as

$$S = -(\mathbf{v}_{\mathbf{E}} + \mathbf{v}_{\mathbf{D}}) \cdot \left[\frac{\nabla n_0}{n_0} + \left(\frac{v_{\parallel}^2}{v_{th}^2} + \frac{\mu B}{T} - \frac{3}{2} \right) \frac{\nabla T}{T} \right] F_m - \frac{Ze}{T} [v_{\parallel} \mathbf{b} + \mathbf{v}_{\mathbf{D}}] \cdot \nabla \langle \phi \rangle_{gy} F_M. \quad (\text{A.2})$$

F_M is the Maxwellian distribution function (equation 3.14) reduces to:

$$F = F_M = \frac{n_0}{\pi^{3/2} v_{th}^3} \exp \left[-\frac{v_{\parallel}^2}{v_{th}^2} \right], \quad (\text{A.3})$$

and \mathbf{v}_D , \mathbf{v}_E are the drifts due to inhomogeneous magnetic fields, and $\mathbf{E} \times \mathbf{B}$ drifts

$$\mathbf{v}_D = \frac{1}{Ze} \left[\frac{mv_{\parallel}^2}{B} + \mu \right] \frac{\mathbf{B} \times \nabla B}{B^2}, \quad (\text{A.4})$$

$$\mathbf{v}_\chi = \mathbf{v}_E = \frac{\mathbf{b} \times \nabla \langle \phi \rangle_{gy}}{B}. \quad (\text{A.5})$$

A.1.2 Coordinate system and magnetic geometry

The model is derived using the orthogonal coordinate system $(x; y; z)$ which is related to the toroidal coordinate system $(R; Z; \varphi)$ (see figure A.1) by:

$$x = R, y = Z, z = R_0 \varphi,$$

with R_0 a reference major radius, taken to be the major radius at the low field side mid-plane of the flux surface of interest.

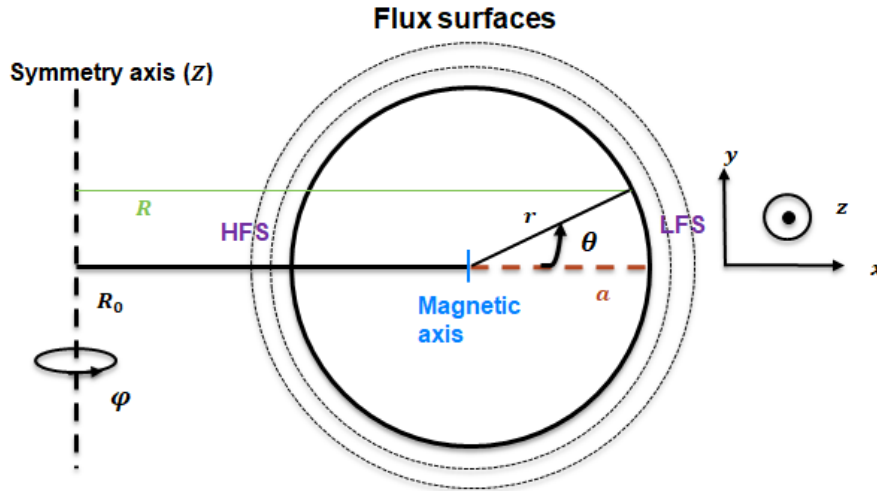


Figure A.1 – Schematic of a poloidal cross section of a tokamak representing coordinates and notations.

The magnetic field is assumed to be purely toroidal and all quantities are evaluated at the low field side mid-plane (one-point model):

$$\mathbf{B} = RB\nabla\varphi = B\mathbf{e}_z \quad \text{with} \quad B = \frac{R_0 B_0}{R} \quad (\text{A.6})$$

$$\nabla\varphi = \frac{1}{R}\mathbf{e}_\varphi \Rightarrow \mathbf{e}_\varphi = \frac{\nabla\varphi}{|\nabla\varphi|} = R\nabla\varphi \quad \rightarrow \text{Unit vector in the toroidal direction}$$

$$\nabla \mathbf{B} = -\frac{R_0 B_0}{R^2} \mathbf{e}_x, \quad (\text{A.7})$$

$$\nabla \mathbf{B}|_{R=R_0} = -\frac{B_0}{R_0} \mathbf{e}_x. \quad (\text{A.8})$$

With this, the drift velocity from equation A.4

$$\mathbf{v}_D = -\frac{1}{Ze} \left[\frac{mv_{\parallel}^2}{B} + \mu \right] \frac{1}{R_0} \mathbf{e}_y. \quad (\text{A.9})$$

A.1.3 Perturbed quantities and gyro-average

The simulation domain is assumed to be homogeneous in the x , y , and z direction in the local limit and assuming solutions of the form.

$$f = f_1 e^{i[\mathbf{k} \cdot \mathbf{x} - \omega t]}$$

$$\phi = \phi_1 e^{i[\mathbf{k} \cdot \mathbf{x} - \omega t]}$$

where $\omega = \omega_r + i\gamma$ is the complex frequency.

$$\nabla f = f_1 e^{-i\omega t} \left[(ik_x \mathbf{x}) e^{(ik_x x)} + (ik_y \mathbf{y}) e^{(ik_y y)} + (ik_z \mathbf{z}) e^{(ik_z z)} \right]$$

$$\nabla f = f i \mathbf{k}. \quad (\text{A.10})$$

where $\mathbf{k} = (k_x \mathbf{e}_x + k_y \mathbf{e}_y + k_z \mathbf{e}_z)$

Similarly

$$\nabla \phi = \phi i \mathbf{k}. \quad (\text{A.11})$$

The gyro-average of ϕ is defined as

$$\langle \phi \rangle_{gy}(\mathbf{X}) = \int_0^{2\pi} \frac{d\zeta}{2\pi} (\mathbf{X} + \rho) \quad (\text{A.12})$$

where \mathbf{X} is the gyro-center position and ρ is the Larmor radius, see section 2.1.1 (which depends on the gyro-angle ζ).

The gyro-averaging operator in guiding-center phase space is simply an integral over the gyro-phase ζ

$$\langle \dots \rangle_{gy} = \frac{1}{2\pi} \int_0^{2\pi} \dots d\zeta \quad (\text{A.13})$$

$\vec{\rho} = \rho \mathbf{a}$; with ρ - larmor radius vector and $\mathbf{a} = \mathbf{x} \cos \varphi + \mathbf{y} \sin \varphi$ - unit vector

$$\mathbf{x} = \mathbf{X} + \rho(\mathbf{x} \cos \varphi + \mathbf{y} \sin \varphi) \quad (\text{A.14})$$

$$\langle \phi(\mathbf{x}) \rangle_{\langle \mathbf{x} \rangle} = \langle \phi(\mathbf{X} + \rho) \rangle_{\langle \mathbf{x} \rangle} \quad (\text{A.15})$$

$$\langle \phi(\mathbf{x}) \rangle_{\langle \mathbf{x} \rangle} = \frac{1}{2\pi} \int_0^{2\pi} \phi_1 e^{i\mathbf{k} \cdot (\mathbf{X} + \rho)} d\zeta d\varphi$$

$$\langle \Phi \rangle_{gy} = J_0(k_\perp \rho) \Phi \quad (\text{A.16})$$

Noting that the Bessel function of the first kind J_0 can be written as

$$J_0(z) = \int_0^\pi e^{iz \cos \theta} d\theta \quad (\text{A.17})$$

When $k_\perp \rho = 0$, the value of $J_0(k_\perp \rho) = 1$ and when $k_\perp \rho = \infty$, $J_0(k_\perp \rho) = 0$.

The expression for \mathbf{v}_E can be written as

$$\begin{aligned} \mathbf{v}_E &= \frac{\mathbf{b} \times \nabla \langle \phi \rangle_{gy}}{B} \\ \mathbf{v}_E &= i \frac{k_x \mathbf{e}_y - k_y \mathbf{e}_x}{B} \langle \phi \rangle_{gy} \end{aligned} \quad (\text{A.18})$$

A.1.4 Linearized one-point gyro-kinetic equation

On rewriting the reference gyrokinetic equation A.1 in a simplified form after putting the values of all the terms, we get the equation:

$$\begin{aligned} -i\omega f + v_\parallel k_z f i - \left(\frac{mv_\parallel^2}{ZeBR_0} + \frac{mv_\perp^2}{2ZeBR_0} \right) i f k_y - \frac{k_x - k_y}{B} \phi f &= \frac{k_y}{B} \frac{\nabla n_0}{n_0} \phi i F_m \\ + \frac{k_y}{B} \phi i \left(\frac{v_\parallel^2}{v_{th}^2} + \frac{\mu B}{T} - \frac{3}{2} \right) \frac{\nabla T}{T} F_m - \frac{Ze}{T} \left[v_\parallel k_z - (mv_\parallel^2 + mv_\perp^2/2) \frac{k_y}{ZeBR_0} \right] \phi i F_m \end{aligned} \quad (\text{A.19})$$

Dividing whole equations by $-i$ and neglecting terms quadratic in the perturbed quantities

$$\begin{aligned} \omega f - v_\parallel k_z f + [mv_\parallel^2 + mv_\perp^2/2] \frac{f k_y}{ZeBR_0} &= \left[-\frac{\nabla n_0}{n_0} - \left(\frac{v_\parallel^2}{v_{th}^2} + \frac{mv_\perp^2}{2T} - \frac{3}{2} \right) \frac{\nabla T}{T} \right] \frac{k_y}{B} F_m \phi \\ + \frac{Ze}{T} \left[v_\parallel k_z - (mv_\parallel^2 + mv_\perp^2/2) \frac{k_y}{ZeBR_0} \right] \phi F_m \end{aligned} \quad (\text{A.20})$$

This linearized equation is then written in a more compact form using the following definitions:

$$\omega_D = v_D^{th} k_y = -\frac{mv_{th}^2}{ZeBR_0} k_y \quad \omega_E = -\frac{v_E^x T_e}{R_0 e \phi} = \frac{T_e k_y}{eBR_0} \quad (\text{A.21})$$

$$R/L_n = -\frac{R_0}{n} \frac{\partial n}{\partial x}, \quad R/L_T = -\frac{R_0}{T} \frac{\partial T}{\partial x} \quad (\text{A.22})$$

$$\mathcal{E}_D = \frac{v_\parallel^2}{v_{th}^2} + \frac{1}{2} \frac{v_\perp^2}{v_{th}^2}, \quad \mathcal{E}_T = \frac{v^2}{v_{th}^2} - \frac{3}{2} \quad (\text{A.23})$$

Also, it is seen that $\omega_D = -2\omega_E$ and $v^2 = v_{\parallel}^2 + v_{\perp}^2$

Here, v_{th} is the thermal velocity, ω_D is the characteristic frequency of the curvature and ∇B drift at the thermal velocity over a wavelength of the perturbed quantities, and ω_E is the characteristic frequency of the radial $\mathbf{E} \times \mathbf{B}$ drift over the reference length R_0 for an electrostatic potential perturbation of wave vector k_y and amplitude T_e/e (neglecting the gyro-average).

So, the final reduced gyro-kinetic equation in slab like approximation is written as:

$$\omega f + [-v_{\parallel}k_z - \mathcal{E}_D\omega_D] f = \left[\frac{R}{L_n} + \mathcal{E}_T \frac{R}{L_T} \right] \frac{\omega_E e}{T_e} F_m \phi + \frac{Ze}{T} [v_{\parallel}k_z + \mathcal{E}_D\omega_D] \phi F_M. \quad (\text{A.24})$$

A.1.5 Quasi-neutrality and adiabatic electron approximation

The quasi-neutrality equation, states that the sum of the gyro-center density and of the polarization density is zero:

$$\sum_{sp} Z_{sp} \int J_0(k_{\perp}\rho) f_{sp} d\mathbf{v} + Z_{sp}^2 n_{sp} [\Gamma(b) - 1] \frac{e\phi}{T_{sp}} = 0 \quad (\text{A.25})$$

This is the normalized version with the inertial term neglected. The sum is over the plasma species and the integral over velocity space. Also

$$\Gamma(b) = I_0(b)e^{-b} = \int_0^{\infty} J_0^2(\sqrt{2bx})e^{-x} dx \quad (\text{A.26})$$

where I_0 is the modified Bessel function of the first kind.

Assuming two species only, main ions and electrons and neglecting the gyro-average for the electrons (i.e. assume $\rho_e = 0$), $J_0(0) = 1$

$$Z_i \int J_0(k_{\perp}\rho_i) f_i d\mathbf{v} + Z_i^2 n_i [\Gamma(b) - 1] \frac{e\phi}{T_i} - \int f_e d\mathbf{v} + n_e [1 - 1] \frac{e\phi}{T_e} = 0 \quad (\text{A.27})$$

$$Z_i \int J_0(k_{\perp}\rho_i) f_i d\mathbf{v} + Z_i^2 n_i [\Gamma(b) - 1] \frac{e\phi}{T_i} - \delta n_e = 0 \quad (\text{A.28})$$

Using the adiabatic electron approximation $\frac{\delta n_e}{n_e} = \frac{e\phi}{T_e}$ to further simplify the quasi-neutrality equation

$$Z_i \int J_0(k_{\perp}\rho_i) f_i d\mathbf{v} + Z_i^2 n_i [\Gamma(b) - 1] \frac{e\phi}{T_i} - \frac{n_e e\phi}{T_e} = 0 \quad (\text{A.29})$$

A.1.6 Final set of equations

Simplifying the model even further by assuming an ion charge of unity $Z = 1$, equal electron and ion temperature $T_e = T_i$, and neglecting the gyro-average for ions.

$$\int f_i d\mathbf{v} = \frac{n_e e \phi}{T} \quad (\text{A.30})$$

$$\tilde{n} = n_{e0} \hat{\phi} = n_0 \hat{\phi}$$

where $\hat{n} = \tilde{n}/n_0$ and $\hat{\phi} = e\phi/T$

The final quasi-neutrality equation is:

$$\hat{n} = \hat{\phi} \quad (\text{A.31})$$

The final linearized gyrokinetic equation is:

$$\omega f + [-v_{\parallel} k_z - \mathcal{E}_D \omega_D] f = \left[\frac{R}{L_n} + \mathcal{E}_T \frac{R}{L_T} \right] \frac{\omega_{Ee}}{T_e} F_m \phi + \frac{Ze}{T} [v_{\parallel} k_z + \mathcal{E}_D \omega_D] \phi F_M \quad (\text{A.32})$$

In the section [A.2](#), we will take moments of this equation to derive a fluid dispersion relation for the ITG and compare it to the kinetic solution in section [A.3](#).

A.2 Fluid Model

A.2.1 Moments of distribution function

The first three moments of the perturbed distribution functions are

$$\tilde{n} = \int f d\mathbf{v}, \quad (\text{A.33})$$

$$\tilde{n} \tilde{v}_{\parallel} = \int f v_{\parallel} d\mathbf{v}, \quad (\text{A.34})$$

$$\delta p = \int f \frac{1}{2} m v_{\parallel}^2 d\mathbf{v}. \quad (\text{A.35})$$

Here the integral is performed over the velocity space. The perturbed temperature δT is defined from the linearization of the perturbed pressure.

The perturbed distribution function is defined as:

$$f = F_M \left[\frac{\tilde{n}}{n_0} + 2 \frac{\tilde{u}_{\parallel}}{v_{th}} \frac{v_{\parallel}}{v_{th}} + \frac{\tilde{T}}{T} \left(\frac{v^2}{v_{th}^2} - \frac{3}{2} \right) \right]. \quad (\text{A.36})$$

The Maxwellian distribution function is:

$$F = F_M = \frac{n_0}{\pi^{3/2} v_{th}^3} \exp \left(- \frac{v_{\parallel}^2 + v_{\perp}^2}{v_{th}^2} \right). \quad (\text{A.37})$$

I. Zeroth Moment (continuity equation)

We first integrate the linearized equation with respect to velocity space

$$\begin{aligned} \int \omega f d\mathbf{v} + \int [-v_{\parallel} k_z - \mathcal{E}_D \omega_D] f d\mathbf{v} &= \int \left[\frac{R}{L_n} + \mathcal{E}_T \frac{R}{L_T} \right] \frac{\omega_{Ee}}{T_e} F_m \phi d\mathbf{v} \\ &+ \int \frac{Ze}{T} [v_{\parallel} k_z + \mathcal{E}_D \omega_D] \phi F_M d\mathbf{v}. \end{aligned} \quad (\text{A.38})$$

Noting the various moments:

$$\{G\}_f = \int f G d\mathbf{v}$$

we have

$$\begin{aligned} \{v_{\parallel}\}_f &= n_0 \tilde{u}_{\parallel}; & \{\mathcal{E}_D \omega_D\}_f &= \omega_D \left[\tilde{n} + n_0 \frac{\tilde{T}}{T} \right]; & \{1\}_F &= n_0; \\ \{v_{\parallel}\}_F &= 0; & \{\mathcal{E}_T\}_F &= 0; & \{\mathcal{E}_D \omega_D\}_F &= \omega_D n_0. \end{aligned}$$

With these values the equation A.38 becomes

$$\omega \tilde{n} + \left[-n_0 \tilde{u}_{\parallel} k_z - \omega_D \left(\tilde{n} + n_0 \frac{\tilde{T}}{T} \right) \right] = \left[\frac{R}{L_n} \frac{\omega_{Ee}}{T_e} + \frac{Ze}{T} \omega_D \right] \phi n_0 \quad (\text{A.39})$$

Normalizing the above equation with the values

$$\begin{aligned} \hat{n} &= \frac{\tilde{n}}{n_0}, & \hat{\phi} &= \frac{e\phi}{T_e}, & \hat{\omega} &= \omega \frac{R}{v_{th}}, & \hat{\omega}_E &= \omega_E \frac{R}{v_{th}}, & \hat{\omega}_D &= \omega_D \frac{R}{v_{th}} \\ \hat{T} &= \frac{\tilde{T}}{T}, & \hat{u}_{\parallel} &= \frac{\tilde{u}_{\parallel}}{v_{th}}, & \hat{k}_z &= k_z R \end{aligned}$$

The final equation for the continuity equation is

$$\hat{\omega} \hat{n} - \hat{k}_z \hat{u}_{\parallel} - \hat{\omega}_D (\hat{n} + \hat{T}) = [\hat{\omega}_E R / L_n + \hat{\omega}_D] \hat{\phi} \quad (\text{A.40})$$

II. First Moment (parallel velocity moment)

Multiplying by v_{\parallel} and integrate over the velocity space.

$$\begin{aligned} \omega \int v_{\parallel} f d\mathbf{v} + \int [-v_{\parallel} k_z - \mathcal{E}_D \omega_D] f v_{\parallel} d\mathbf{v} &= \int v_{\parallel} \left[\frac{R}{L_n} + \mathcal{E}_T \frac{R}{L_T} \right] \frac{\omega_{Ee}}{T_e} F_m \phi d\mathbf{v} \\ &+ \int v_{\parallel} [v_{\parallel} k_z + \mathcal{E}_D \omega_D] \frac{e\phi}{T} F_M d\mathbf{v} \end{aligned} \quad (\text{A.41})$$

Here $d\mathbf{v} = dv_{\parallel} dv_{\perp}$

$$\begin{aligned} \{v_{\parallel}\}_f &= n_0 \tilde{u}_{\parallel}; & \{v_{\parallel}^2\}_f &= \frac{v_{th}^2 n_0}{2} (\hat{n} + \hat{T}); & \{v_{\parallel} \mathcal{E}_D\}_f &= 2n_0 \tilde{u}_{\parallel}; & \{v_{\parallel}\}_F &= 0 \\ \{v_{\parallel} \mathcal{E}_T\}_F &= 0; & \{v_{\parallel}^2\}_F &= \frac{n_0 v_{th}^2}{2}; & \{v_{\parallel} \mathcal{E}_D\}_F &= 0 \end{aligned}$$

The parallel velocity moment equation is

$$\hat{\omega}\hat{u}_{\parallel} - \frac{\hat{k}_z}{2}(\hat{n} + \hat{T}) - 2\hat{u}_{\parallel}\hat{\omega}_D = \frac{\hat{k}_z\hat{\phi}}{2} \quad (\text{A.42})$$

III. Second Moment (Energy balance equation)

$$\begin{aligned} \omega \int v^2 f d\mathbf{v} - \int v^2 v_{\parallel} k_z f d\mathbf{v} - \int \mathcal{E}_D \omega_D v^2 f d\mathbf{v} &= \int v^2 \left[\frac{R}{L_n} + \mathcal{E}_T \frac{R}{L_T} \right] \frac{\omega_E e}{T_e} F_m \phi d\mathbf{v} \\ &+ \int v^2 [v_{\parallel} k_z + \mathcal{E}_D \omega_D] \frac{e\phi}{T} F_M d\mathbf{v} \end{aligned} \quad (\text{A.43})$$

$$\begin{aligned} \{v^2\}_f &= \frac{3}{2}n_0v_{th}^2(\hat{n} + \hat{T}); & \{v^2v_{\parallel}\}_f &= \frac{5}{2}\tilde{u}_{\parallel}n_0v_{th}^2; & \{\mathcal{E}_Dv^2\}_f &= \frac{5}{2}v_{th}^2n_0(\hat{n} + 2\hat{T}) \\ \{v^2\}_F &= \frac{3}{2}v_{th}^2n_0; & \{\mathcal{E}_Tv^2\}_F &= \frac{3}{2}v_{th}^2n_0; & \{v^2v_{\parallel}\}_F &= 0; & \{v^2\mathcal{E}_D\}_F &= \frac{5}{2}v_{th}^2n_0 \end{aligned}$$

Putting all these values in the equation A.43:

$$\begin{aligned} \omega \frac{3}{2}v_{th}^2n_0(\hat{n} + \hat{T}) - k_z \frac{5}{2}\tilde{u}_{\parallel}v_{th}^2n_0 - \omega_D \frac{5}{2}v_{th}^2n_0(\hat{n} + 2\hat{T}) &= \left[\frac{R}{L_n} \frac{3}{2}v_{th}^2n_0 + \frac{R}{L_T} \frac{3}{2}v_{th}^2n_0 \right] \frac{e\phi}{T_e} \omega_E \\ &+ \frac{5}{2}v_{th}^2n_0\omega_D \frac{e\phi}{T_e} \end{aligned} \quad (\text{A.44})$$

Normalizing equation, we get the final pressure balance equation

$$\hat{\omega}(\hat{n} + \hat{T}) - \frac{5}{3}\hat{k}_z\hat{u}_{\parallel} - \frac{5}{3}\hat{\omega}_D(\hat{n} + 2\hat{T}) = \left[\left(\frac{R}{L_n} + \frac{R}{L_T} \right) \hat{\omega}_E + \frac{5}{3}\hat{\omega}_D \right] \hat{\phi} \quad (\text{A.45})$$

Subtracting the continuity equation from this equation

$$\begin{aligned} \hat{\omega}\hat{n} + \hat{\omega}\hat{T} - \hat{\omega}\hat{n} - \frac{5}{3}\hat{k}_z\hat{u}_{\parallel} + \hat{k}_z\hat{u}_{\parallel} - \frac{5}{3}\hat{\omega}_D(\hat{n} + 2\hat{T}) + \hat{\omega}_D(\hat{n} + \hat{T}) &= \left[\left(\frac{R}{L_n} + \frac{R}{L_T} \right) \hat{\omega}_E + \frac{5}{3}\hat{\omega}_D \right] \hat{\phi} \\ &- [\omega_E R/L_n + \omega_D] \hat{\phi} \end{aligned} \quad (\text{A.46})$$

$$\hat{\omega}\hat{T} - \frac{2}{3}\hat{k}_z\hat{u}_{\parallel} - \frac{2}{3}\hat{\omega}_D\hat{n} - \frac{7}{3}\hat{\omega}_D\hat{T} = \left[\frac{R}{L_T}\hat{\omega}_E + \frac{2}{3}\hat{\omega}_D \right] \hat{\phi} \quad (\text{A.47})$$

on normalizing with respect to $\hat{\omega}_D = -2$ and using $\omega_D = -2\omega_E$; we get $\omega_E = 1$

$$\hat{\omega}\hat{T} - \frac{2}{3}\hat{k}_z\hat{u}_{\parallel} + \frac{4}{3}\hat{n} + \frac{14}{3}\hat{T} = \left[\frac{R}{L_T} - \frac{4}{3} \right] \hat{\phi} \quad (\text{A.48})$$

This equation is a normalized version of the energy balance equation when taking the value of $\hat{\omega}_D = -2$.

A.2.2 Toroidal ITG and SLAB ITG

Writing a full set of equations together with the quasi-neutrality equation again

$$\begin{cases} \hat{\omega}\hat{n} - \hat{k}_z\hat{u}_{\parallel} - \hat{\omega}_D(\hat{n} + \hat{T}) = [\hat{\omega}_E R/L_n + \hat{\omega}_D] \hat{\phi} \\ \hat{\omega}\hat{u}_{\parallel} - \frac{\hat{k}_z}{2}(\hat{n} + \hat{T}) - 2\hat{u}_{\parallel}\hat{\omega}_D = \frac{\hat{k}_z\hat{\phi}}{2} \\ \hat{\omega}\hat{T} - \frac{2}{3}\hat{k}_z\hat{u}_{\parallel} - \frac{2}{3}\hat{\omega}_D\hat{n} - \frac{7}{3}\hat{\omega}_D\hat{T} = \left[\frac{R}{L_T}\hat{\omega}_E + \frac{2}{3}\hat{\omega}_D\right] \hat{\phi}, \\ \hat{n} = \hat{\phi} \end{cases}$$

A.2.2.1 Toroidal ITG

Physical Picture of Toroidal ITG

Considering the simplest case by keeping temperature and temperature gradient R/L_T and neglecting all the other terms.

$$\begin{cases} \hat{\omega}\hat{n} - \hat{\omega}_D\hat{T} = 0 \\ \hat{\omega}\hat{T} - \frac{R}{L_T}\hat{\omega}_E\hat{\phi} = 0 \\ \hat{n} = \hat{\phi} \end{cases}$$

On solving above equation, we can find the growth rate of unstable mode as:

$$\hat{\omega} = \pm\sqrt{\hat{\omega}_D\hat{\omega}_E} \sqrt{R/L_T} \Rightarrow \omega_r + \nu\gamma = \pm\sqrt{\hat{\omega}_D\hat{\omega}_E} \sqrt{R/L_T} \quad (\text{A.49})$$

$$\gamma = \sqrt{|\hat{\omega}_D\hat{\omega}_E|} \sqrt{R/L_T} \quad (\text{A.50})$$

We can see clearly from this equation that the growth rate is directly proportional to the normalized logarithmic temperature gradient. Therefore, the growth rate increases with an increase in the temperature gradient.

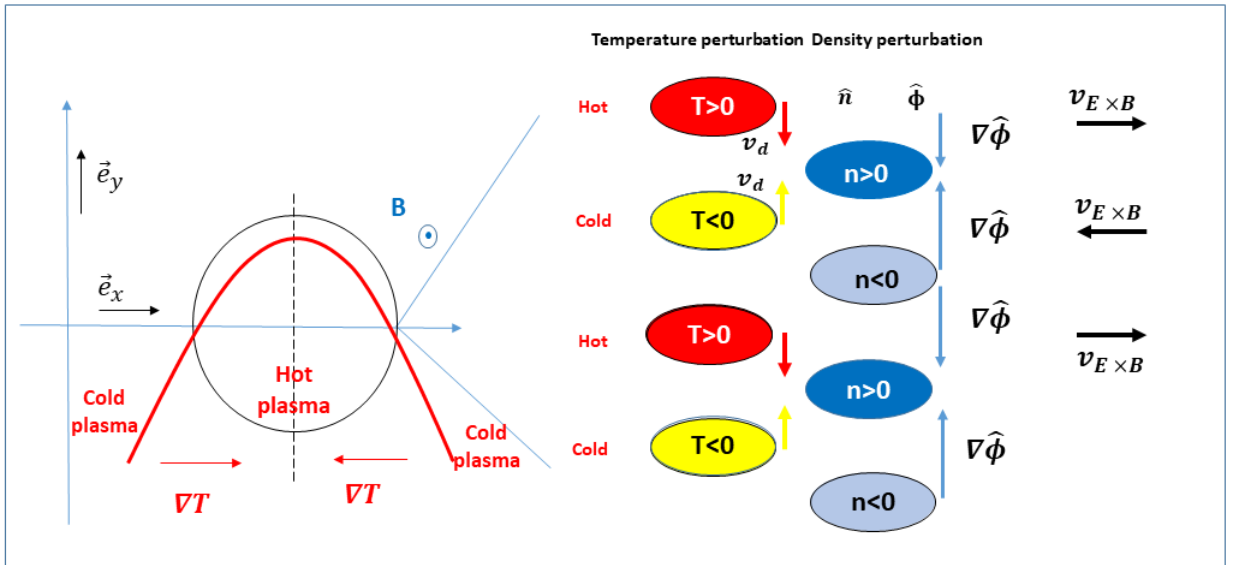


Figure A.2 – Physical picture of toroidal ITG.

As illustrated in figure A.2, starting from a small temperature perturbation, the temperature dependence of the ∇B drift will generate a density perturbation (by compression) as can be seen from the first equation. Because density perturbation is directly proportional to electrostatic potential as from the third equation, perturbation of electrostatic potential will follow the same direction as density. From the second equation we can see that this electrostatic potential perturbation will act on the background distribution function and because of $\mathbf{E} \times \mathbf{B}$ drift this hotter plasma will move towards hotter plasma and cold plasma will move towards cold plasma side which will enhance the perturbation on the low field side.

Whereas on high field-side, the hotter plasma will move towards the colder side and colder plasma will move towards the hotter side that will suppress the perturbation.

Steps to derive Toroidal ITG

Neglect the parallel motion (strong inertia) $\hat{u} = 0$ and put $\hat{k}_z = 0 = \hat{k}_\parallel$.

Writing continuity and energy balance equations together with quasi-neutrality equation

$$\begin{cases} \hat{\omega}\hat{n} - \hat{\omega}_D(\hat{n} + \hat{T}) = [\hat{\omega}_E R/L_n + \hat{\omega}_D] \hat{\phi} \\ \hat{\omega}\hat{T} - \frac{2}{3}\hat{\omega}_D\hat{n} - \frac{7}{3}\hat{\omega}_D\hat{T} = \left[\frac{R}{L_T}\hat{\omega}_E + \frac{2}{3}\hat{\omega}_D\right] \hat{\phi} \\ \hat{n} = \hat{\phi} \end{cases}$$

Replacing \hat{n} by $\hat{\phi}$

$$\hat{\omega}\hat{\phi} - \hat{\omega}_D(\hat{\phi} + \hat{T}) = [\hat{\omega}_E R/L_n + \hat{\omega}_D] \hat{\phi} \quad (\text{A.51})$$

$$\hat{\omega}\hat{T} - \frac{2}{3}\hat{\omega}_D\hat{\phi} - \frac{7}{3}\hat{\omega}_D\hat{T} = \left[\frac{R}{L_T}\hat{\omega}_E + \frac{2}{3}\hat{\omega}_D\right] \hat{\phi} \quad (\text{A.52})$$

Finding the value of \hat{T} from equation A.51

$$\hat{T} = \frac{1}{\hat{\omega}_D} \left[\hat{\omega}\hat{\phi} - 2\hat{\omega}_D\hat{\phi} - \frac{R}{L_n}\hat{\omega}_E\hat{\phi} \right] = 0 \quad (\text{A.53})$$

and substituting this value in the equation A.52 and solving for $\hat{\phi}$ we get the final equation as :

$$\hat{\omega}^2 - \hat{\omega} \left(\frac{13}{3}\hat{\omega}_D + \hat{\omega}_E \frac{R}{L_N} \right) + \hat{\omega}_D \hat{\omega}_E \left(\frac{7}{3} \frac{R}{L_n} - \frac{R}{L_T} + \frac{10}{3} \frac{\hat{\omega}_D}{\hat{\omega}_E} \right) = 0 \quad (\text{A.54})$$

This is another simplified dispersion relation for toroidal ITG. The solution of this equation will give the growth rate. From this equation we can see clearly on keeping all the terms, we would have found that Eigenvalues are not just imaginary (as in the previous model), but complex numbers in which the imaginary part (growth

rate) is positive provided that the normalized logarithmic temperature gradient R/L_T exceeds a particular value (threshold).

The solution to the above equation is

$$\hat{\omega} = \frac{1}{2} \left[\left(\frac{13}{3} \hat{\omega}_D + \hat{\omega}_E \frac{R}{L_N} \right) \pm \sqrt{\underbrace{\left(\frac{13}{3} \hat{\omega}_D + \hat{\omega}_E \frac{R}{L_N} \right)^2 - 4 \hat{\omega}_D \hat{\omega}_E \left(\frac{7}{3} \frac{R}{L_n} - \frac{R}{L_T} + \frac{10}{3} \frac{\hat{\omega}_D}{\hat{\omega}_E} \right)}_{\Delta}} \right]$$

where $\hat{\omega} = \hat{\omega}_r + i\gamma$

$$\hat{\omega}_r + i\gamma = \frac{1}{2} \left[\left(\frac{13}{3} \hat{\omega}_D + \hat{\omega}_E \frac{R}{L_N} \right) \pm \sqrt{\Delta} \right] \quad (\text{A.55})$$

When $\Delta < 0$, $\gamma = \pm \sqrt{|\Delta|}$

$$\gamma = \pm \frac{1}{2} \sqrt{\left(\frac{13}{3} \hat{\omega}_D + \hat{\omega}_E \frac{R}{L_N} \right)^2 - 4 \hat{\omega}_D \hat{\omega}_E \left(\frac{7}{3} \frac{R}{L_n} - \frac{R}{L_T} + \frac{10}{3} \frac{\hat{\omega}_D}{\hat{\omega}_E} \right)} \quad (\text{A.56})$$

From this dispersion relation we can see the variation of growth rate γ as a function of R/L_n and R/L_T for a fixed value of $\hat{\omega}_D$ and $\hat{\omega}_E$.

For $k_y \rho = 0.4$, $\hat{\omega}_D = -k_y \rho$, $\hat{\omega}_E = k_y \rho / 2$ the variation of growth rate γ as a function of R/L_n and R/L_T is given in figure A.3 and a 2D contour plot is represented in figure A.4.

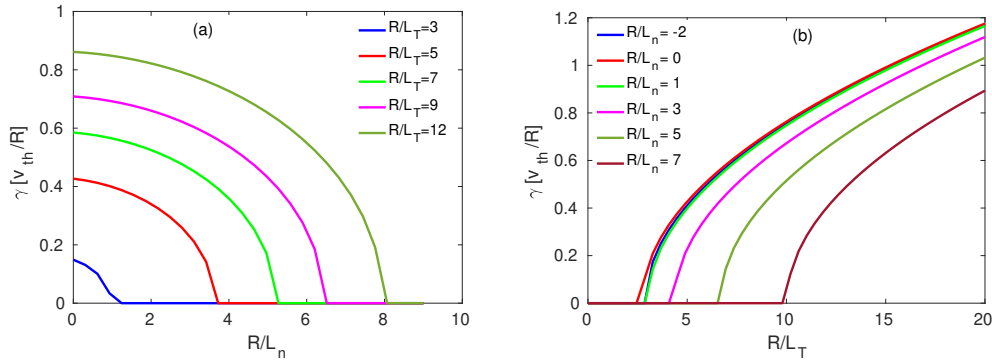


Figure A.3 – Growth rate (γ) as a function of density gradient scale length (R/L_n) for a fixed value of (R/L_T) (a) and temperature gradient scale length (R/L_T) for a fixed value of (R/L_n) (b) for toroidal ITG using fluid model.

From figure A.3, we can see that the density gradient is stabilizing the toroidal ITG, whereas temperature gradient is enhancing the linear growth rate, which causes instability in the plasma. Also, for a particular value of density gradient, there will be a minimum threshold value of temperature gradient for perturbation to grow below which it is stable.

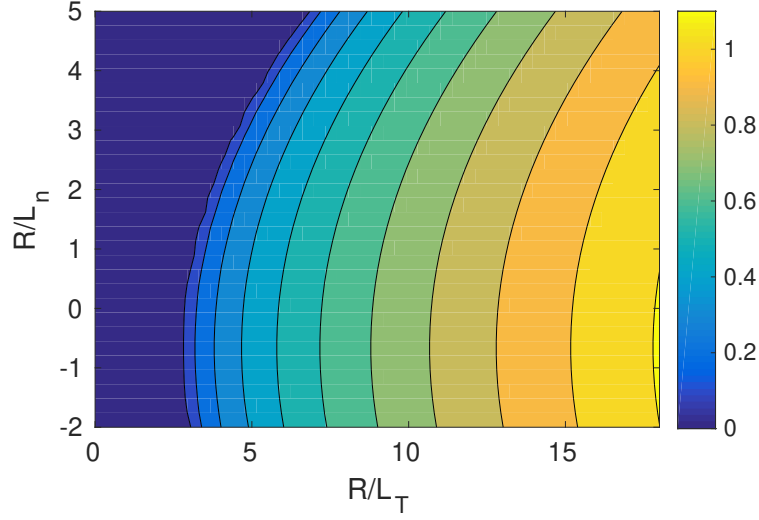


Figure A.4 – Growth rate (γ) as a function of density gradient scale length (R/L_n) and temperature gradient scale length (R/L_T) for toroidal ITG using fluid model.

A.2.2.2 Slab ITG

Assume $\hat{\omega}_D = 0$

$$\begin{cases} \hat{\omega}\hat{n} - \hat{k}_z\hat{u}_{\parallel} = \hat{\omega}_E R/L_n \hat{\phi} \\ \hat{\omega}\hat{u}_{\parallel} - \frac{\hat{k}_z}{2}(\hat{n} + \hat{T}) = \frac{\hat{k}_z\hat{\phi}}{2} \\ \hat{\omega}\hat{T} - \frac{2}{3}\hat{k}_z\hat{u}_{\parallel} = \frac{R}{L_T}\hat{\omega}_E\hat{\phi} \\ \hat{n} = \hat{\phi} \end{cases}$$

Finding the value of \hat{u}_{\parallel} from first equation and \hat{T} from 2nd equation and simplifying we get the dispersion relation for slab ITG as

$$\hat{\omega} \left(\frac{2\hat{\omega}^2\hat{\phi}}{\hat{k}_z^2} - \frac{2\hat{\omega}\hat{\omega}_E R/L_n \hat{\phi}}{\hat{k}_z^2} - 2\hat{\phi} \right) - \frac{2}{3}\hat{k}_z \left(\frac{\hat{\omega}\hat{\phi} - \hat{\omega}_E R/L_n \hat{\phi}}{\hat{k}_z} \right) = \frac{R}{L_T}\hat{\omega}_E\hat{\phi} \quad (\text{A.57})$$

$$\hat{\omega}^3 - \hat{\omega}^2\hat{\omega}_E R/L_n - \frac{4}{3}\hat{\omega}\hat{k}_z^2 + \hat{\omega}_E\hat{k}_z^2 \left(\frac{1}{3}R/L_n - \frac{1}{2}R/L_T \right) = 0 \quad (\text{A.58})$$

This is the final dispersion relation for Slab ITG with adiabatic electrons and electrostatic case. This is a cubic polynomial, and analytical solution of this equation is nontrivial. However, it can be solved numerically.

Contour plots of growth rate (γ) as function of normalized logarithmic temperature gradient (R/L_T) and density gradient (R/L_n) for $q = 1.1$, $k_Z = 1/q$ and different values of $k_y\rho$ ($\omega_E = k_y/2$) is given in figure A.5. As we can see from figure on increasing $k_y\rho$, i.e., increasing ω_E ($k_y\rho = \omega_E/2$), growth rate threshold decreases.

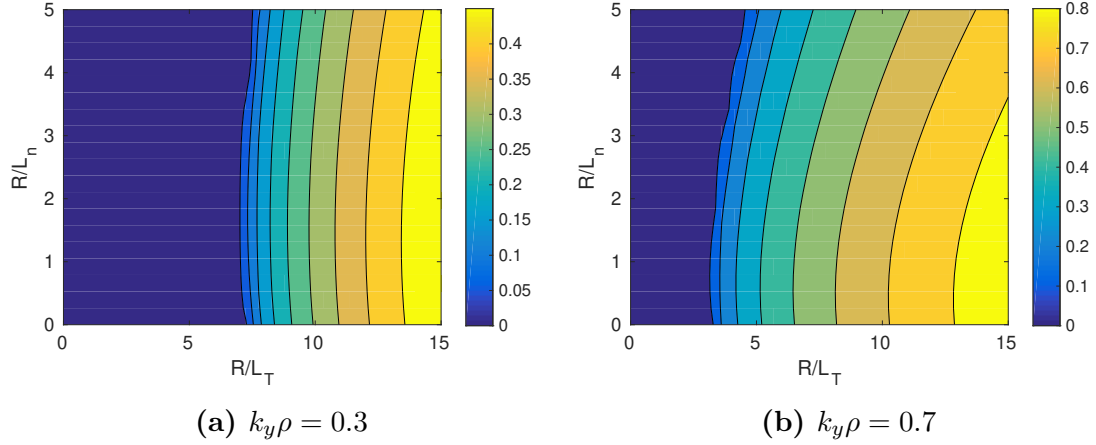


Figure A.5 – Growth rate (γ) as a function of density gradient scale length (R/L_n) and temperature gradient scale length (R/L_T) for $k_y\rho = 0.3$ (a) and $k_y\rho = 0.7$ (b), for slab ITG using fluid model and for a fixed value of $q=1.1$.

For $k_y\rho = 0.3$ and for different values of q ($k_z = 1/q$), contour plots of growth rate (γ) as function of normalized logarithmic temperature gradient (R/L_T) and density gradient (R/L_n) is given in figure A.6. As seen, the threshold of growth rate decreases with increasing q value. Also, for higher values of q density gradient stabilizing the slab ITG, however, temperature gradient enhancing the growth rate.

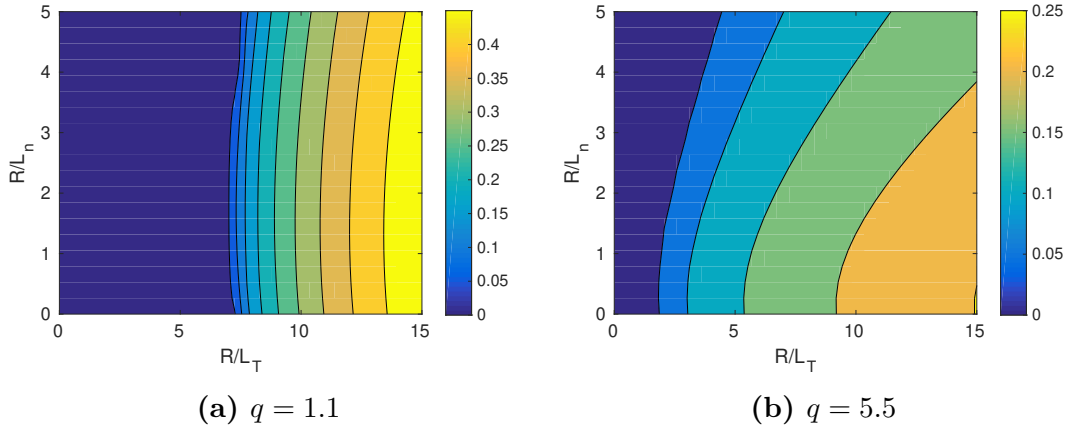


Figure A.6 – Growth rate (γ) as a function of density gradient scale length (R/L_n) and temperature gradient scale length (R/L_T) for $q = 1.1$ (a) and $q = 5.5$ (b), for slab ITG using fluid model and for a fixed value of $k_y\rho = 0.3$.

Growth rate as a function of normalized logarithmic density gradient (R/L_n) for various values of R/L_T and growth rate as function of temperature gradient (R/L_T) for various values of R/L_n for $k_y = 0.3$ and $q = 1.1$ is given in figure A.7 (a) and (b).

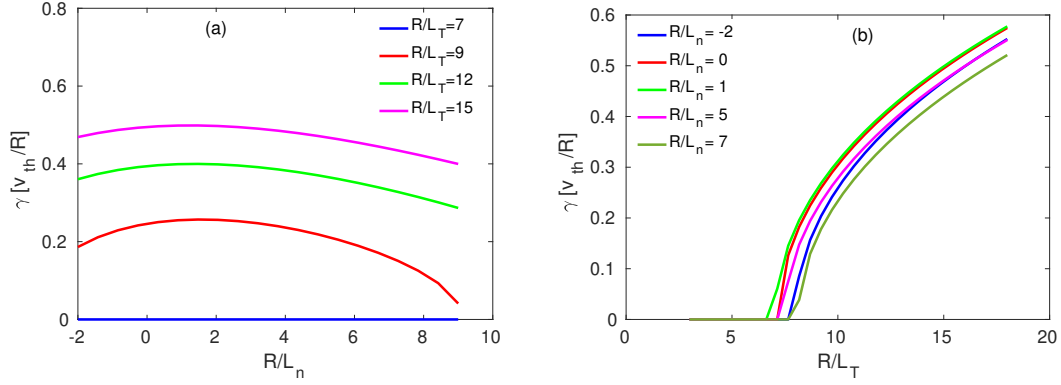


Figure A.7 – Growth rate (γ) as a function of density gradient scale length (R/L_n) for a fixed value of (R/L_T) (a) and temperature gradient scale length (R/L_T) for a fixed value of (R/L_n) (b) for slab ITG using the fluid model for $k_y \rho = 0.3$ and $q = 1.1$.

As can be seen from the figure, above a threshold, the density gradient stabilized the slab ITG; however, temperature gradient increases the growth rate that will destabilize the mode.

A.3 Kinetic model

Combining the final linearized quasi-neutrality equation and the linearized gyrokinetic equation of section A.1.6 to write a dispersion relation

$$\hat{n} = \hat{\phi} \quad (\text{A.59})$$

$$\omega f + [-v_{\parallel} k_z - \mathcal{E}_D \omega_D] f = \left[\frac{R}{L_n} + \mathcal{E}_T \frac{R}{L_T} \right] \frac{\omega_E e}{T_e} F_m \phi + [v_{\parallel} k_z + \mathcal{E}_D \omega_D] \frac{e \phi}{T} F_M \quad (\text{A.60})$$

The distribution function in an un-normalized form is given as

$$f = \frac{[(R/L_n + \mathcal{E}_T R/L_T) \omega_E + [v_{\parallel} k_z + \mathcal{E}_D \omega_D] \frac{e \phi}{T} F_M]}{\omega - v_{\parallel} k_z - \mathcal{E}_D \omega_D} \quad (\text{A.61})$$

Normalizing the equation with the quantities using the relation v_{th} for velocities, R_0 for lengths and v_{th}/R_0 for frequencies.

$$\hat{v} = \frac{\tilde{v}_{\parallel}}{v_{th}}; \quad \hat{k}_z = k_z R; \quad \hat{\omega}_D = \omega_D R_0 / v_{th}; \quad \hat{\omega}_E = \omega_E R_0 / v_{th}$$

The $\hat{\omega}_D$ and $\hat{\omega}_E$ can also be written as function of the reference larmor radius ρ_0 defined as: $\rho_0 = \frac{m v_{th}}{e B}$:

$$\hat{\omega}_D = -\rho_i k_y; \quad \hat{\omega}_E = \frac{1}{2} \rho_i k_y$$

The normalized background distribution function is defined as $\hat{F}_M = F_M v_{th}^3/n_0$, and the perturbed distribution function is : $\hat{f} = f v_{th}^3/n_0$.

$$\hat{F}_M = \frac{1}{\Pi^{3/2}} e^{-(\hat{v}_{\parallel}^2 + \hat{v}_{\perp}^2)} \quad (\text{A.62})$$

$$f = \frac{[(R/L_n + \mathcal{E}_T R/L_T) \hat{\omega}_E + [\hat{v}_{\parallel} \hat{k}_z + \mathcal{E}_D \hat{\omega}_D]] \hat{\phi} F_M}{\hat{\omega} - \hat{v}_{\parallel} \hat{k}_z - \mathcal{E}_D \hat{\omega}_D} \quad (\text{A.63})$$

$$\hat{n} = \frac{\tilde{n}}{n_0} = \frac{1}{n_0} \int f d\mathbf{v} \quad (\text{A.64})$$

$$\hat{n} = \frac{\hat{\phi}}{n_0} \int \frac{(R/L_n + \mathcal{E}_T R/L_T) \hat{\omega}_E + \hat{v}_{\parallel} \hat{k}_z + \mathcal{E}_D \hat{\omega}_D}{\hat{\omega} - \hat{v}_{\parallel} \hat{k}_z - \mathcal{E}_D \hat{\omega}_D} F_M d\mathbf{v} \quad (\text{A.65})$$

where $d\mathbf{v}$ is defined as $d\mathbf{v} = d\hat{v}_{\parallel} d\hat{v}_y d\hat{v}_x v_{th}^3$, $\mathbf{v} = v_{\parallel} \mathbf{b} + v_{\perp} (\cos \alpha \hat{e}_x + \sin \alpha \hat{e}_y)$

$$1 = \int \frac{(R/L_n + \mathcal{E}_T R/L_T) \hat{\omega}_E + \hat{v}_{\parallel} \hat{k}_z + \mathcal{E}_D \hat{\omega}_D}{\hat{\omega} - \hat{v}_{\parallel} \hat{k}_z - \mathcal{E}_D \hat{\omega}_D} \hat{F}_M 2\pi d\hat{v}_{\parallel} d\hat{v}_{\perp} \quad (\text{A.66})$$

where $\omega = \omega_r + i\gamma$, $\mathcal{E}_T = \hat{v}_{\parallel}^2 + \hat{v}_{\perp}^2 - 3/2$, $\mathcal{E}_D = \hat{v}^2 + 1/2\hat{v}_{\perp}^2$

$$1 = \int \underbrace{\frac{(R/L_n + \mathcal{E}_T R/L_T) \hat{\omega}_E + \hat{v}_{\parallel} \hat{k}_z + \mathcal{E}_D \hat{\omega}_D}{\hat{\omega} - \hat{v}_{\parallel} \hat{k}_z - \mathcal{E}_D \hat{\omega}_D} \hat{F}_M}_{\hat{f}} d\hat{v} \quad (\text{A.67})$$

$$\omega = \omega_r(ii) + i\gamma(jj)$$

$$|\int \hat{f} d\hat{v} - 1| = 0 \quad (\text{A.68})$$

where

$$\hat{f} = \hat{F}_M \frac{(R/L_n + \mathcal{E}_T R/L_T) \hat{\omega}_E + \hat{v}_{\parallel} \hat{k}_z + \mathcal{E}_D \hat{\omega}_D}{\hat{\omega} - \hat{v}_{\parallel} \hat{k}_z - \mathcal{E}_D \hat{\omega}_D} \quad (\text{A.69})$$

There is no analytical solution exist for this equation (at least without approximation). So, to find the solution of above equation (eq: A.67), it need to be solved numerically. On plotting $(\int \hat{f} d\hat{v} - 1)$ as function of γ and ω_r , zeros of the contour represents the solution.

Linear growth rate γ as a function of temperature gradient scale length (R/L_T) for the fixed value of density gradient scale length $R/L_n = 1$ and $R/L_n = 3$, with $k_y \rho = 0.3$, $k_z = 0$, $\omega_D = -k_y \rho$, $\omega_D = k_y \rho/2$ is shown in figure A.8. The figure shows that there is minimum threshold value of R/L_T for growth rate to start and after that it increases as value of the R/L_T increases.

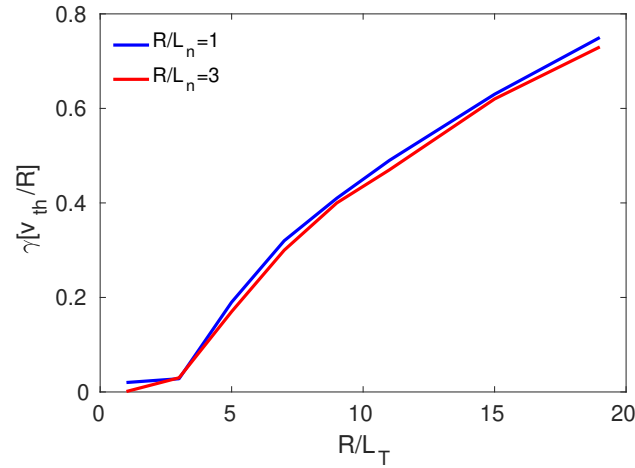


Figure A.8 – Growth rate ($\hat{\gamma}$) as function of R/L_T for a fixed value of $R/L_n = 1$ (blue curve) and $R/L_n = 3$ (red curve) for the kinetic model. Other parameters are $k_y\rho = 0.3$, $k_z = 0$, $\omega_D = -k_y\rho$, $\omega_D = k_y\rho/2$.

A comparison of growth rate ($\hat{\gamma}$) as function of R/L_T for a fixed value of $R/L_n = 3$ for the kinetic model and fluid model is shown in figure A.9.

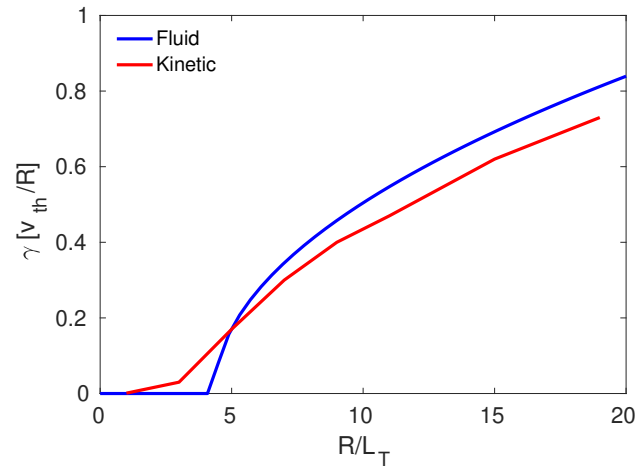


Figure A.9 – Comparison of growth rate ($\hat{\gamma}$) as function of R/L_T for a fixed value of $R/L_n = 3$, $k_y\rho = 0.3$, $k_z = 0$, $\omega_D = -k_y\rho$, and $\omega_D = k_y\rho/2$ for fluid model (blue curve) and kinetic model (red curve).

It can be seen from figure A.9 that in the region far away from the threshold value of temperature gradient scale length, both fluid model and kinetic models are in good agreement to predict growth rate. However, close to threshold value fluid models predicts zero growth rate, whereas the kinetic model indicates a finite growth rate in the system. Therefore, the fluid model fails to give a growth rate at close to a threshold value; hence, we need a kinetic model to explain it.

Bibliography

- [1] *BP Statistical Review of World Energy*, 2019.
- [2] Francis F. Chen. *Introduction to Plasma Physics and Controlled Fusion*. Springer, Cham, 2018.
- [3] Ralph Dux. *Plasmaphysik und Fusionsforschung, Teil 2: Fusionsforschung*, 2002.
- [4] J D Lawson. Some criteria for a power producing thermonuclear reactor. *Proceedings of the Physical Society. Section B*, 70(1):6–10, jan 1957. doi: 10.1088/0370-1301/70/1/303. URL <https://doi.org/10.1088%2F0370-1301%2F70%2F1%2F303>.
- [5] NIF-<https://lasers.llnl.gov>.
- [6] LMJ <https://www.lmj.cea.fr>.
- [7] Daniel Clery. *A Piece of the sun: the quest for fusion energy*. The Overlook Press, 2014.
- [8] M. Keilhacker. Fusion physics progress on jet. *Fusion Engineering and Design*, 46(2):273 – 290, 1999. doi: [https://doi.org/10.1016/S0920-3796\(99\)00020-4](https://doi.org/10.1016/S0920-3796(99)00020-4).
- [9] ITER Organization. *What will ITER do?*, 2017. URL <https://www.iter.org/sci/Goals>.
- [10] *Fusion Physics*. Non-serial Publications. INTERNATIONAL ATOMIC ENERGY AGENCY, Vienna, 2012. ISBN 978-92-0-130410-0. URL <https://www.iaea.org/publications/8879/fusion-physics>.
- [11] <https://www.eurofusion.org/>.
- [12] John Wesson. *Tokamaks*. Clarendon Press Oxford University Press, Oxford New York, 2004. ISBN 0198509227.
- [13] CEA. *Magnetic confinement*, 2001.
- [14] F Ryter, W Suttrop, B Brüsehaber, M Kaufmann, V Mertens, H Murmann, A G Peeters, J Stober, J Schweinzer, H Zohm, and ASDEX Upgrade Team. H-mode power threshold and transition in ASDEX upgrade. *Plasma Physics and Controlled Fusion*, 40(5):725–729, may 1998. doi: 10.1088/0741-3335/40/5/032. URL <https://doi.org/10.1088%2F0741-3335%2F40%2F5%2F032>.
- [15] A. E. Hubbard, D. G. Whyte, R. M. Churchill, I. Cziegler, A. Dominguez, T. Golfinopoulos, J. W. Hughes, J. E. Rice, I. Bespamyatnov, M. J. Greenwald, N. Howard, B. Lipschultz, E. S. Marmor, M. L. Reinke, W. L. Rowan, and J. L.

- Terry. Edge energy transport barrier and turbulence in the i-mode regime on alcator c-mod. *Physics of Plasmas*, 18(5):056115, 2011. doi: 10.1063/1.3582135. URL <https://doi.org/10.1063/1.3582135>.
- [16] H Zohm. Edge localized modes (ELMs). *Plasma Physics and Controlled Fusion*, 38(2):105–128, feb 1996. doi: 10.1088/0741-3335/38/2/001. URL <https://doi.org/10.1088%2F0741-3335%2F38%2F2%2F001>.
- [17] F. L. Hinton and R. D. Hazeltine. Theory of plasma transport in toroidal confinement systems. *Rev. Mod. Phys.*, 48:239–308, Apr 1976. doi: 10.1103/RevModPhys.48.239. URL <https://link.aps.org/doi/10.1103/RevModPhys.48.239>.
- [18] W. A. Houlberg, K. C. Shaing, S. P. Hirshman, and M. C. Zarnstorff. Bootstrap current and neoclassical transport in tokamaks of arbitrary collisionality and aspect ratio. *Physics of Plasmas*, 4(9):3230–3242, 1997. doi: 10.1063/1.872465. URL <https://doi.org/10.1063/1.872465>.
- [19] E A Belli and J Candy. Kinetic calculation of neoclassical transport including self-consistent electron and impurity dynamics. *Plasma Physics and Controlled Fusion*, 50(9):095010, jul 2008. doi: 10.1088/0741-3335/50/9/095010. URL <https://doi.org/10.1088%2F0741-3335%2F50%2F9%2F095010>.
- [20] Per Helander and Dieter Sigmar. *Collisional Transport in Magnetized Plasmas*. Cambridge University Press, 2002.
- [21] W. Horton. Drift waves and transport. *Rev. Mod. Phys.*, 71:735–778, Apr 1999. doi: 10.1103/RevModPhys.71.735.
- [22] G F Matthews, M Beurskens, S Brezinsek, M Groth, E Joffrin, A Loving, M Kear, M-L Mayoral, R Neu, P Prior, V Riccardo, F Rimini, M Rubel, G Sips, E Villedieu, P de Vries, and M L Watkins and. JET ITER-like wall—overview and experimental programme. *Physica Scripta*, T145:014001, 2011. doi: 10.1088/0031-8949/2011/t145/014001. URL <https://doi.org/10.1088%2F0031-8949%2F2011%2Ft145%2F014001>.
- [23] R Neu et. al. Plasma wall interaction and its implication in an all tungsten divertor tokamak. *Plasma Physics and Controlled Fusion*, 49(12B):B59–B70, 2007.
- [24] J Bucalossi, M Missirlian, P Moreau, F Samaille, E Tsitrone, D van Houtte, T Batal, C Bourdelle, M Chantant, Y Corre, et al. The west project: Testing iter divertor high heat flux component technology in a steady state tokamak environment. *Fusion Engineering and Design*, 89(7-8):907–912, 2014.
- [25] R. Dux. *Impurity Transport in Tokamak Plasmas, Technical Report 10/27, IPP, Garching, Germany*, sept 2004.
- [26] T. Pütterich, R. Neu, R. Dux, A.D. Whiteford, M.G. O'Mullane, and H.P. Summers and. Calculation and experimental test of the cooling factor of tungsten.

- Nuclear Fusion*, 50(2):025012, 1 2010. doi: 10.1088/0029-5515/50/2/025012. URL <https://doi.org/10.1088%2F0029-5515%2F50%2F2%2F025012>.
- [27] E. Joffrin, M. Baruzzo, M. Beurskens, C. Bourdelle, S. Brezinsek, J. Bucalossi, P. Buratti, G. Calabro, C.D. Challis, M. Clever, J. Coenen, E. Delabie, R. Dux, P. Lomas, E. de la Luna, P. de Vries, J. Flanagan, L. Frassinetti, D. Frigione, C. Giroud, M. Groth, N. Hawkes, J. Hobirk, M. Lehnen, G. Maddison, J. Mailoux, C.F. Maggi, G. Matthews, M. Mayoral, A. Meigs, R. Neu, I. Nunes, T. Puetterich, F. Rimini, M. Sertoli, B. Sieglin, A.C.C. Sips, G. van Rooij, and I. Voitsekhovitch and. First scenario development with the JET new ITER-like wall. *Nuclear Fusion*, 54(1):013011, 12 2013. doi: 10.1088/0029-5515/54/1/013011. URL <https://doi.org/10.1088%2F0029-5515%2F54%2F1%2F013011>.
- [28] C. Angioni, P. Mantica, T. Pütterich, M. Valisa, M. Baruzzo, E.A. Belli, P. Belo, F.J. Casson, C. Challis, P. Drewelow, C. Giroud, N. Hawkes, T.C. Hender, J. Hobirk, T. Koskela, L. Lauro Taroni, C.F. Maggi, J. Mlynar, T. Odstreil, M.L. Reinke, and M. Romanelli and. Tungsten transport in JET h-mode plasmas in hybrid scenario, experimental observations and modelling. *Nuclear Fusion*, 54(8):083028, 7 2014. doi: 10.1088/0029-5515/54/8/083028. URL <https://doi.org/10.1088%2F0029-5515%2F54%2F8%2F083028>.
- [29] R Neu, R Dux, A Geier, A Kallenbach, R Pugno, V Rohde, D Bolshukhin, J C Fuchs, O Gehre, O Gruber, J Hobirk, M Kaufmann, K Krieger, M Laux, C Maggi, H Murmann, J Neuhauser, F Ryter, A C C Sips, A Stäbler, J Stober, W Suttrop, H Zohm, and the ASDEX Upgrade Team. Impurity behaviour in the ASDEX upgrade divertor tokamak with large area tungsten walls. *Plasma Physics and Controlled Fusion*, 44(6):811–826, 5 2002. doi: 10.1088/0741-3335/44/6/313. URL <https://doi.org/10.1088%2F0741-3335%2F44%2F6%2F313>.
- [30] R. Neu, R. Dux, A. Geier, O. Gruber, A. Kallenbach, K. Krieger, H. Maier, R. Pugno, V. Rohde, and S. Schweizer. Tungsten as plasma-facing material in asdex upgrade. *Fusion Engineering and Design*, 65(3):367 – 374, 2003. ISSN 0920-3796. doi: [https://doi.org/10.1016/S0920-3796\(02\)00381-2](https://doi.org/10.1016/S0920-3796(02)00381-2). URL <http://www.sciencedirect.com/science/article/pii/S0920379602003812>. 1st International Workshop on Innovative Concepts for Plasma - Interactive Components in Fusion Devices.
- [31] A Kallenbach, R Neu, R Dux, H-U Fahrbach, J C Fuchs, L Giannone, O Gruber, A Herrmann, P T Lang, B Lipschultz, C F Maggi, J Neuhauser, V Philipps, T Pütterich, V Rohde, J Roth, G Sergienko, A Sips, and ASDEX Upgrade Team. Tokamak operation with high-z plasma facing components. *Plasma Physics and Controlled Fusion*, 47(12B):B207–B222, 2005. doi: 10.1088/0741-3335/47/12b/s16. URL <https://doi.org/10.1088%2F0741-3335%2F47%2F12b%2Fs16>.
- [32] C. Angioni, F. J. Casson, P. Mantica, T. Pütterich, M. Valisa, E. A. Belli, R. Bilato, C. Giroud, and P. Helander. The impact of poloidal asymmetries on tungsten transport in the core of jet h-mode plasmas. *Physics of Plasmas*, 22(5):055902, 2015. doi: 10.1063/1.4919036. URL <https://aip.scitation.org/doi/abs/10.1063/1.4919036>.

- [33] C. Bourdelle, X. Garbet, F. Imbeaux, A. Casati, N. Dubuit, R. Guirlet, and T. Parisot. A new gyrokinetic quasilinear transport model applied to particle transport in tokamak plasmas. *Physics of Plasmas*, 14(11):112501, 2007. doi: 10.1063/1.2800869. URL <https://doi.org/10.1063/1.2800869>.
- [34] G. M. Staebler, J. E. Kinsey, and R. E. Waltz. A theory-based transport model with comprehensive physics. *Physics of Plasmas*, 14(5):055909, 2007. doi: 10.1063/1.2436852. URL <https://doi.org/10.1063/1.2436852>.
- [35] S. Moradi, I. Pusztai, I. Voitsekhovitch, L. Garzotti, C. Bourdelle, M.J. Pueschel, I. Lupelli, and M. Romanelli and. Core micro-instability analysis of JET hybrid and baseline discharges with carbon wall. *Nuclear Fusion*, 54(12):123016, 2014. doi: 10.1088/0029-5515/54/12/123016. URL <https://doi.org/10.1088/0029-5515/54/12/123016>.
- [36] J Citrin, J Garcia, T Gorler, F Jenko, P Mantica, D Told, C Bourdelle, D R Hatch, G M D Hogeweyj, T Johnson, M J Pueschel, and M Schneider. Electromagnetic stabilization of tokamak microturbulence in a high- β regime. *Plasma Physics and Controlled Fusion*, 57(1):014032, 2015. doi: 10.1088/0741-3335/57/1/014032. URL <https://doi.org/10.1088/0741-3335/57/1/014032>.
- [37] M.F.F Nave, J Rapp, T Bolzonella, R Dux, M.J Mantsinen, R Budny, P Dumortier, M. von Hellermann, S Jachmich, H.R Koslowski, G Maddison, A Messiaen, P Monier-Garbet, J Ongena, M.E Puiatti, J Strachan, G Telesca, B Unterberg, M Valisa, P. de Vries, and contributors to the JET-EFDA Workprogramme. Role of sawtooth in avoiding impurity accumulation and maintaining good confinement in JET radiative mantle discharges. *Nuclear Fusion*, 43(10):1204–1213, sep 2003. doi: 10.1088/0029-5515/43/10/023. URL <https://doi.org/10.1088/0029-5515/43/10/023>.
- [38] T Putterich, R Dux, R Neu, M Bernert, M N A Beurskens, V Bobkov, S Brezinsek, C Challis, J W Coenen, I Coffey, A Czarnecka, C Giroud, P Jacquet, E Joffrin, A Kallenbach, M Lehnen, E Lerche, E de la Luna, S Marsen, G Matthews, M-L Mayoral, R M McDermott, A Meigs, J Mlynar, M Sertoli, G van Rooij, and and. Observations on the w-transport in the core plasma of JET and ASDEX upgrade. *Plasma Physics and Controlled Fusion*, 55(12):124036, 2013. doi: 10.1088/0741-3335/55/12/124036. URL <https://doi.org/10.1088/0741-3335/55/12/124036>.
- [39] M. Sertoli, T. Odstrcil, and C. Angioni and. Interplay between central ECRH and saturated $(m,n) = (1, 1)$ MHD activity in mitigating tungsten accumulation at ASDEX upgrade. *Nuclear Fusion*, 55(11):113029, sep 2015. doi: 10.1088/0029-5515/55/11/113029. URL <https://doi.org/10.1088/0029-5515/55/11/113029>.
- [40] Kenro Miyamoto. *Plasma Physics and Controlled Nuclear Fusion*. Springer, 2004.

- [41] F. J. (Francis James) Casson. Turbulent transport in rotating tokamak plasmas. March 2011. URL <http://wrap.warwick.ac.uk/36765/>.
- [42] J. Q. Dong, P. N. Guzdar, and Y. C. Lee. Finite beta effects on ion temperature gradient driven modes. *The Physics of Fluids*, 30(9):2694–2702, 1987. doi: 10.1063/1.866034.
- [43] Y. Idomura, S. Tokuda, and M. Wakatani. Gyrokinetic theory of slab ion temperature gradient mode in negative shear tokamaks. *Physics of Plasmas*, 6(12):4658–4671, 1999. doi: 10.1063/1.873752.
- [44] J. Weiland and A. Hirose. Electromagnetic and kinetic effects on the ion temperature gradient mode. *Nuclear Fusion*, 32(1):151–155, jan 1992. doi: 10.1088/0029-5515/32/1/i13. URL <https://doi.org/10.1088%2F0029-5515%2F32%2F1%2Fi13>.
- [45] J. Y. Kim, W. Horton, and J. Q. Dong. Electromagnetic effect on the toroidal ion temperature gradient mode. *Physics of Fluids B: Plasma Physics*, 5(11):4030–4039, 1993. doi: 10.1063/1.860623. URL <https://doi.org/10.1063/1.860623>.
- [46] H. Nordman, J. Weiland, and A. Jarmén. Simulation of toroidal drift mode turbulence driven by temperature gradients and electron trapping. *Nuclear Fusion*, 30(6):983–996, jun 1990. doi: 10.1088/0029-5515/30/6/001. URL <https://doi.org/10.1088%2F0029-5515%2F30%2F6%2F001>.
- [47] T. S. Hahm and W. M. Tang. Weak turbulence theory of collisionless trapped electron driven drift instability in tokamaks. *Physics of Fluids B: Plasma Physics*, 3(4):989–999, 1991. doi: 10.1063/1.859854.
- [48] Tilman Dannert and Frank Jenko. Gyrokinetic simulation of collisionless trapped-electron mode turbulence. *Physics of Plasmas*, 12(7):072309, 2005. doi: 10.1063/1.1947447. URL <https://doi.org/10.1063/1.1947447>.
- [49] Y. Idomura, M. Wakatani, and S. Tokuda. Gyrokinetic theory of slab electron temperature gradient mode in negative shear tokamaks. *Physics of Plasmas*, 7(6):2456–2468, 2000. doi: 10.1063/1.874085.
- [50] F. Jenko, W. Dorland, M. Kotschenreuther, and B. N. Rogers. Electron temperature gradient driven turbulence. *Physics of Plasmas*, 7(5):1904–1910, 2000. doi: 10.1063/1.874014. URL <https://doi.org/10.1063/1.874014>.
- [51] J. Q. Dong, H. Sanuki, and K. Itoh. Gyrokinetic study of the electron temperature gradient instability in plasmas with slightly hollow density profiles. *Physics of Plasmas*, 8(8):3635–3644, 2001. doi: 10.1063/1.1381564.
- [52] W.M. Tang, J.W. Connor, and R.J. Hastie. Kinetic-ballooning-mode theory in general geometry. *Nuclear Fusion*, 20(11):1439–1453, nov 1980. doi: 10.1088/0029-5515/20/11/011. URL <https://doi.org/10.1088%2F0029-5515%2F20%2F11%2F011>.

- [53] C. Z. Cheng. Kinetic theory of collisionless ballooning modes. *The Physics of Fluids*, 25(6):1020–1026, 1982. doi: 10.1063/1.863858. URL <https://aip.scitation.org/doi/abs/10.1063/1.863858>.
- [54] F. Jenko, D. Told, T. Görler, J. Citrin, A. Bañón Navarro, C. Bourdelle, S. Brunner, G. Conway, T. Dannert, H. Doerk, D.R. Hatch, J.W. Haverkort, J. Hobirk, G.M.D. Hogeweyj, P. Mantica, M.J. Pueschel, O. Sauter, L. Villard, and E. Wolfrum and. Global and local gyrokinetic simulations of high-performance discharges in view of ITER. *Nuclear Fusion*, 53(7):073003, may 2013. doi: 10.1088/0029-5515/53/7/073003. URL <https://doi.org/10.1088/0029-5515/53/7/073003>.
- [55] J. W. Connor, R. J. Hastie, and J. B. Taylor. Shear, periodicity, and plasma ballooning modes. *Phys. Rev. Lett.*, 40:396–399, Feb 1978. doi: 10.1103/PhysRevLett.40.396. URL <https://link.aps.org/doi/10.1103/PhysRevLett.40.396>.
- [56] Shih-Tung Tsai and Liu Chen. Theory of kinetic ballooning modes excited by energetic particles in tokamaks. *Physics of Fluids B: Plasma Physics*, 5(9):3284–3290, 1993. doi: 10.1063/1.860624. URL <https://doi.org/10.1063/1.860624>.
- [57] Gang Zhao and Liu Chen. Gyrokinetic particle-in-cell simulation of alfvénic ion-temperature-gradient modes in tokamak plasma. *Physics of Plasmas*, 9(3):861–868, 2002. doi: 10.1063/1.1454124. URL <https://doi.org/10.1063/1.1454124>.
- [58] G. L. Falchetto, J. Vaclavik, and L. Villard. Global-gyrokinetic study of finite β effects on linear microinstabilities. *Physics of Plasmas*, 10(5):1424–1436, 2003. doi: 10.1063/1.1566028. URL <https://doi.org/10.1063/1.1566028>.
- [59] Fulvio Zonca, Liu Chen, and Robert A Santoro. Kinetic theory of low-frequency alfvén modes in tokamaks. *Plasma Physics and Controlled Fusion*, 38(11):2011–2028, nov 1996. doi: 10.1088/0741-3335/38/11/011. URL <https://doi.org/10.1088/0741-3335/38/11/011>.
- [60] W. W. Heidbrink, E. Ruskov, E. M. Carolipio, J. Fang, M. A. van Zeeland, and R. A. James. What is the “beta-induced alfvén eigenmode?”. *Physics of Plasmas*, 6(4):1147–1161, 1999. doi: 10.1063/1.873359. URL <https://doi.org/10.1063/1.873359>.
- [61] A. Hirose, L. Zhang, and M. Elia. Erratum: “ion temperature gradient-driven ballooning mode in tokamaks” [phys. plasmas 2, 859 (1995)]. *Physics of Plasmas*, 3(1):439–439, 1996. doi: 10.1063/1.872083. URL <https://doi.org/10.1063/1.872083>.
- [62] G. Rewoldt, W. M. Tang, and R. J. Hastie. Collisional effects on kinetic electromagnetic modes and associated quasilinear transport. *The Physics of Fluids*, 30(3):807–817, 1987. doi: 10.1063/1.866332. URL <https://aip.scitation.org/doi/abs/10.1063/1.866332>.

- [63] D. R. Hatch, M. J. Pueschel, F. Jenko, W. M. Nevins, P. W. Terry, and H. Doerk. Magnetic stochasticity and transport due to nonlinearly excited subdominant microtearing modes. *Physics of Plasmas*, 20(1):012307, 2013. doi: 10.1063/1.4789448. URL <https://doi.org/10.1063/1.4789448>.
- [64] A A Vlasov. THE VIBRATIONAL PROPERTIES OF AN ELECTRON GAS. *Soviet Physics Uspekhi*, 10(6):721–733, jun 1968. doi: 10.1070/pu1968v010n06abeh003709. URL <https://doi.org/10.1070%2Fpu1968v010n06abeh003709>.
- [65] Robert G. Littlejohn. Variational principles of guiding centre motion. *Journal of Plasma Physics*, 29(1):111–125, 1983. doi: 10.1017/S002237780000060X.
- [66] T. S. Hahm. Nonlinear gyrokinetic equations for tokamak microturbulence. *The Physics of Fluids*, 31(9):2670–2673, 1988. doi: 10.1063/1.866544. URL <https://aip.scitation.org/doi/abs/10.1063/1.866544>.
- [67] A. Brizard. Nonlinear gyrokinetic maxwell-vlasov equations using magnetic co-ordinates. *Journal of Plasma Physics*, 41(3):541–559, 1989. doi: 10.1017/S0022377800014070.
- [68] A. J. Brizard and T. S. Hahm. Foundations of nonlinear gyrokinetic theory. *Rev. Mod. Phys.*, 79:421–468, Apr 2007. doi: 10.1103/RevModPhys.79.421. URL <https://link.aps.org/doi/10.1103/RevModPhys.79.421>.
- [69] A.G. Peeters, Y. Camenen, F.J. Casson, W.A. Hornsby, A.P. Snodin, D. Strintzi, and G. Szepesi. The nonlinear gyro-kinetic flux tube code gkw. *Computer Physics Communications*, 180(12):2650 – 2672, 2009. doi: <https://doi.org/10.1016/j.cpc.2009.07.001>. URL <http://www.sciencedirect.com/science/article/pii/S0010465509002112>.
- [70] A. G. Peeters et al. GWK How and Why, <https://bitbucket.org/gkw/gkw/overview>.
- [71] A. G. Peeters, C. Angioni, and D. Strintzi. Toroidal momentum pinch velocity due to the coriolis drift effect on small scale instabilities in a toroidal plasma. *Phys. Rev. Lett.*, 98:265003, Jun 2007. doi: 10.1103/PhysRevLett.98.265003. URL <https://link.aps.org/doi/10.1103/PhysRevLett.98.265003>.
- [72] A. G. Peeters, D. Strintzi, Y. Camenen, C. Angioni, F. J. Casson, W. A. Hornsby, and A. P. Snodin. Erratum: “influence of the centrifugal force and parallel dynamics on the toroidal momentum transport due to small scale turbulence in a tokamak” [phys. plasmas 16, 042310 (2009)]. *Physics of Plasmas*, 19(9):099901, 2012. doi: 10.1063/1.4751549. URL <https://doi.org/10.1063/1.4751549>.
- [73] X. Lapillonne, S. Brunner, T. Dannert, S. Jolliet, A. Marinoni, L. Villard, T. Görler, F. Jenko, and F. Merz. Clarifications to the limitations of the $s - \alpha$ equilibrium model for gyrokinetic computations of turbulence. *Physics of Plasmas*, 16(3):032308, 2009. URL <https://doi.org/10.1063/1.3096710>.

- [74] R. L. Miller, M. S. Chu, J. M. Greene, Y. R. Lin-Liu, and R. E. Waltz. Noncircular, finite aspect ratio, local equilibrium model. *Physics of Plasmas*, 5(4):973–978, 1998. doi: 10.1063/1.872666. URL <https://doi.org/10.1063/1.872666>.
- [75] H. Lütjens, A. Bondeson, and O. Sauter. The chease code for toroidal mhd equilibria. *Computer Physics Communications*, 97(3):219 – 260, 1996. ISSN 0010-4655. doi: [https://doi.org/10.1016/0010-4655\(96\)00046-X](https://doi.org/10.1016/0010-4655(96)00046-X). URL <http://www.sciencedirect.com/science/article/pii/001046559600046X>.
- [76] John William Connor, R. J. Hastie, and John Bryan Taylor. High mode number stability of an axisymmetric toroidal plasma. *Proceedings of the Royal Society of London. A. Mathematical and Physical Sciences*, 365(1720):1–17, 1979. doi: 10.1098/rspa.1979.0001. URL <https://royalsocietypublishing.org/doi/abs/10.1098/rspa.1979.0001>.
- [77] J. Garcia, C. Challis, J. Citrin, H. Doerk, G. Giruzzi, T. Görler, F. Jenko, and P. Maget and. Key impact of finite-beta and fast ions in core and edge tokamak regions for the transition to advanced scenarios. *Nuclear Fusion*, 55(5):053007, apr 2015. doi: 10.1088/0029-5515/55/5/053007. URL <https://doi.org/10.1088%2F0029-5515%2F55%2F5%2F053007>.
- [78] M Shimada, D.J Campbell, V Mukhovatov, M Fujiwara, N Kirneva, K Lackner, M Nagami, V.D Pustovitov, N Uckan, J Wesley, N Asakura, A.E Costley, A.J.H Donn e, E.J Doyle, A Fasoli, C Gormezano, Y Gribov, O Gruber, T.C Hender, W Houlberg, S Ide, Y Kamada, A Leonard, B Lipschultz, A Loarte, K Miyamoto, V Mukhovatov, T.H Osborne, A Polevoi, and A.C.C Sips. Chapter 1: Overview and summary. *Nuclear Fusion*, 47(6):S1–S17, jun 2007. doi: 10.1088/0029-5515/47/6/s01. URL <https://doi.org/10.1088%2F0029-5515%2F47%2F6%2Fs01>.
- [79] D C McDonald, L Laborde, J C DeBoo, F Ryter, M Brix, C D Challis, P de Vries, C Giroud, J Hobirk, D Howell, E Joffrin, T C Luce, J Mailloux, V Pericoli-Ridolfini, A C C Sips, and K Thomsen and. JET confinement studies and their scaling to high β_n , ITER scenarios. *Plasma Physics and Controlled Fusion*, 50(12):124013, nov 2008. doi: 10.1088/0741-3335/50/12/124013. URL <https://doi.org/10.1088%2F0741-3335%2F50%2F12%2F124013>.
- [80] C Gormezano, A.C.C Sips, T.C Luce, S Ide, A Becoulet, X Litaudon, A Isayama, J Hobirk, M.R Wade, T Oikawa, R Prater, A Zvonkov, B Lloyd, T Suzuki, E Barbato, P Bonoli, C.K Phillips, V Vdovin, E Joffrin, T Casper, J Ferron, D Mazon, D Moreau, R Bundy, C Kessel, A Fukuyama, N Hayashi, F Imbeaux, M Murakami, A.R Polevoi, and H.E. St John. Chapter 6: Steady state operation. *Nuclear Fusion*, 47(6):S285–S336, jun 2007. doi: 10.1088/0029-5515/47/6/s06. URL <https://doi.org/10.1088%2F0029-5515%2F47%2F6%2Fs06>.
- [81] J Hobirk, F Imbeaux, F Crisanti, P Buratti, C D Challis, E Joffrin, B Alper, Y Andrew, P Beaumont, M Beurskens, A Boboc, A Botrugno, M Brix, G Calabro, I Coffey, S Conroy, O Ford, D Frigione, J Garcia, C Giroud, N C

- Hawkes, D Howell, I Jenkins, D Keeling, M Kempenaars, H Leggate, P Lotte, E de la Luna, G P Maddison, P Mantica, C Mazzotta, D C McDonald, A Meigs, I Nunes, E Rachlew, F Rimini, M Schneider, A C C Sips, J K Stober, W Studholme, T Tala, M Tsalas, I Voitsekhovitch, and P C de Vries. Improved confinement in JET hybrid discharges. *Plasma Physics and Controlled Fusion*, 54(9):095001, 2012. doi: 10.1088/0741-3335/54/9/095001. URL <https://doi.org/10.1088%2F0741-3335%2F54%2F9%2F095001>.
- [82] J. Garcia and G. Giruzzi and. On the different physical mechanisms for accessing hybrid scenarios on JET. *Nuclear Fusion*, 53(4):043023, 2013. doi: 10.1088/0029-5515/53/4/043023. URL <https://doi.org/10.1088%2F0029-5515%2F53%2F4%2F043023>.
- [83] A. Ho, J. Citrin, F. Auriemma, C. Bourdelle, F.J. Casson, Hyun-Tae Kim, P. Manas, G. Szepesi, and H. Weisen and. Application of gaussian process regression to plasma turbulent transport model validation via integrated modelling. *Nuclear Fusion*, 59(5):056007, 2019. doi: 10.1088/1741-4326/ab065a. URL <https://doi.org/10.1088%2F1741-4326%2Fab065a>.
- [84] L. L. Lao, H. St. John, R. D. Stambaugh, A. G. Kellman, and W. Pfeiffer. Reconstruction of current profile parameters and plasma shapes in tokamaks. *Nucl. Fusion*, 25(11):1611–1622, November 1985.
- [85] A. Di Siena, T. Görler, H. Doerk, R. Bilato, J. Citrin, T. Johnson, M. Schneider, and E. Poli. Non-maxwellian fast particle effects in gyrokinetic gene simulations. *Physics of Plasmas*, 25(4):042304, 2018. doi: 10.1063/1.5020122. URL <https://doi.org/10.1063/1.5020122>.
- [86] C.D. Challis, J.G. Cordey, H. Hamnén, P.M. Stubberfield, J.P. Christiansen, E. Lazzaro, D.G. Muir, D. Stork, and E. Thompson. Non-inductively driven currents in JET. *Nuclear Fusion*, 29(4):563–570, apr 1989. doi: 10.1088/0029-5515/29/4/002. URL <https://doi.org/10.1088%2F0029-5515%2F29%2F4%2F002>.
- [87] M. Schneider, L.-G. Eriksson, I. Jenkins, J.F. Artaud, V. Basiuk, F. Imbeaux, T. Oikawa, and and. Simulation of the neutral beam deposition within integrated tokamak modelling frameworks. *Nuclear Fusion*, 51(6):063019, may 2011. doi: 10.1088/0029-5515/51/6/063019. URL <https://doi.org/10.1088%2F0029-5515%2F51%2F6%2F063019>.
- [88] J.F. Artaud, V. Basiuk, F. Imbeaux, M. Schneider, J. Garcia, G. Giruzzi, P. Huynh, T. Aniel, F. Albajar, J.M. Ané, A. Bécoulet, C. Bourdelle, A. Casati, L. Colas, J. Decker, R. Dumont, L.G. Eriksson, X. Garbet, R. Guirlet, P. Hertout, G.T. Hoang, W. Houlberg, G. Huysmans, E. Joffrin, S.H. Kim, F. Köchl, J. Lister, X. Litaudon, P. Maget, R. Masset, B. Pégourié, Y. Peysson, P. Thomas, E. Tsitrone, and F. Turco. The CRONOS suite of codes for integrated tokamak modelling. *Nuclear Fusion*, 50(4):043001, mar 2010. doi: 10.1088/0029-5515/50/4/043001. URL <https://doi.org/10.1088%2F0029-5515%2F50%2F4%2F043001>.

- [89] C. Bourdelle, W. Dorland, X. Garbet, G. W. Hammett, M. Kotschenreuther, G. Rewoldt, and E. J. Synakowski. Stabilizing impact of high gradient of β on microturbulence. *Physics of Plasmas*, 10(7):2881–2887, 2003. doi: 10.1063/1.1585032. URL <https://doi.org/10.1063/1.1585032>.
- [90] M Romanelli, A Zocco, and F Crisanti and. Fast ion stabilization of the ion temperature gradient driven modes in the joint european torus hybrid-scenario plasmas: a trigger mechanism for internal transport barrier formation. *Plasma Physics and Controlled Fusion*, 52(4):045007, mar 2010. doi: 10.1088/0741-3335/52/4/045007. URL <https://doi.org/10.1088%2F0741-3335%2F52%2F4%2F045007>.
- [91] G Tardini, J Hobirk, V.G Igochine, C.F Maggi, P Martin, D McCune, A.G Peeters, A.C.C Sips, A Stabler, J Stober, and the ASDEX Upgrade Team. Thermal ions dilution and ITG suppression in ASDEX upgrade ion ITBs. *Nuclear Fusion*, 47(4):280–287, mar 2007. doi: 10.1088/0029-5515/47/4/006. URL <https://doi.org/10.1088%2F0029-5515%2F47%2F4%2F006>.
- [92] M. J. Pueschel, M. Kammerer, and F. Jenko. Gyrokinetic turbulence simulations at high plasma beta. *Physics of Plasmas*, 15(10):102310, 2008. doi: 10.1063/1.3005380. URL <https://doi.org/10.1063/1.3005380>.
- [93] M. S. Chu, C. Chu, G. Guest, J. Y. Hsu, and T. Ohkawa. Kinetic analysis of the localized magnetohydrodynamic ballooning mode. *Phys. Rev. Lett.*, 41:247–250, Jul 1978. doi: 10.1103/PhysRevLett.41.247. URL <https://link.aps.org/doi/10.1103/PhysRevLett.41.247>.
- [94] Fulvio Zonca, Liu Chen, J. Q. Dong, and Robert A. Santoro. Existence of ion temperature gradient driven shear alfvén instabilities in tokamaks. *Physics of Plasmas*, 6(5):1917–1924, 1999. doi: 10.1063/1.873449. URL <https://doi.org/10.1063/1.873449>.
- [95] S. Maeyama, A. Ishizawa, T.-H. Watanabe, M. Nakata, N. Miyato, M. Yagi, and Y. Idomura. Comparison between kinetic-ballooning-mode-driven turbulence and ion-temperature-gradient-driven turbulence. *Physics of Plasmas*, 21(5):052301, 2014. doi: 10.1063/1.4873379. URL <https://doi.org/10.1063/1.4873379>.
- [96] F. Jenko, W. Dorland, and G. W. Hammett. Critical gradient formula for toroidal electron temperature gradient modes. *Physics of Plasmas*, 8(9):4096–4104, 2001. doi: 10.1063/1.1391261. URL <https://doi.org/10.1063/1.1391261>.
- [97] Y. Camenen, F. J. Casson, P. Manas, and A. G. Peeters. Interplay between toroidal rotation and flow shear in turbulence stabilisation. *Physics of Plasmas*, 23(2):022507, 2016. doi: 10.1063/1.4942422. URL <https://doi.org/10.1063/1.4942422>.
- [98] P H Diamond, S-I Itoh, K Itoh, and T S Hahm. Zonal flows in plasma—a review. *Plasma Physics and Controlled Fusion*, 47(5):R35–R161, apr 2005. doi: 10.1088/0741-3335/47/5/r01. URL <https://doi.org/10.1088/0741-3335/47/5/r01>.

- [99] J. Citrin, F. Jenko, P. Mantica, D. Told, C. Bourdelle, J. Garcia, J. W. Haverkort, G. M. D. Hogeweyj, T. Johnson, and M. J. Pueschel. Nonlinear stabilization of tokamak microturbulence by fast ions. *Phys. Rev. Lett.*, 111: 155001, Oct 2013. doi: 10.1103/PhysRevLett.111.155001.
- [100] A. Casati, C. Bourdelle, X. Garbet, F. Imbeaux, J. Candy, F. Clairet, G. Dif-Pradalier, G. Falchetto, T. Gerbaud, V. Grandgirard, Ö.D. Gürçan, P. Hennequin, J. Kinsey, M. Ottaviani, R. Sabot, Y. Sarazin, L. Vermare, and R.E. Waltz. Validating a quasi-linear transport model versus nonlinear simulations. *Nuclear Fusion*, 49(8):085012, jul 2009. doi: 10.1088/0029-5515/49/8/085012. URL <https://doi.org/10.1088%2F0029-5515%2F49%2F8%2F085012>.
- [101] J. E. Kinsey, G. M. Staebler, and R. E. Waltz. The first transport code simulations using the trapped gyro-landau-fluid model. *Physics of Plasmas*, 15(5):055908, 2008. doi: 10.1063/1.2889008. URL <https://doi.org/10.1063/1.2889008>.
- [102] C Angioni, A.G Peeters, X Garbet, A Manini, F Ryter, and ASDEX Upgrade Team. Density response to central electron heating: theoretical investigations and experimental observations in ASDEX upgrade. *Nuclear Fusion*, 44(8): 827–845, jun 2004. doi: 10.1088/0029-5515/44/8/003. URL <https://doi.org/10.1088%2F0029-5515%2F44%2F8%2F003>.
- [103] Donald Knuth. Qualikiz saturation rule. URL https://gitlab.com/qualikiz-group/QualiKiz-documents/-/blob/master/reports/saturation_rule.pdf.
- [104] J. Candy. Beta scaling of transport in microturbulence simulations. *Physics of Plasmas*, 12(7):072307, 2005. doi: 10.1063/1.1954123.
- [105] D. R. Hatch, M. J. Pueschel, F. Jenko, W. M. Nevins, P. W. Terry, and H. Doerk. Origin of magnetic stochasticity and transport in plasma microturbulence. *Phys. Rev. Lett.*, 108:235002, Jun 2012. doi: 10.1103/PhysRevLett.108.235002. URL <https://link.aps.org/doi/10.1103/PhysRevLett.108.235002>.
- [106] X. Jian, C. Holland, J. Candy, E. Belli, V. Chan, A. M. Garofalo, and S. Ding. Role of microtearing turbulence in diii-d high bootstrap current fraction plasmas. *Phys. Rev. Lett.*, 123:225002, Nov 2019. doi: 10.1103/PhysRevLett.123.225002. URL <https://link.aps.org/doi/10.1103/PhysRevLett.123.225002>.
- [107] A.R. Polevoi, A. Loarte, R. Dux, T. Eich, E. Fable, D. Coster, S. Maruyama, S.Yu. Medvedev, F. Köchl, and V.E. Zhogolev. Integrated simulations of h-mode operation in ITER including core fuelling, divertor detachment and ELM control. *Nuclear Fusion*, 58(5):056020, mar 2018. doi: 10.1088/1741-4326/aab4ad. URL <https://doi.org/10.1088%2F1741-4326%2Faab4ad>.
- [108] Thomas Putterich. Control and diagnostic of high-z impurities in fusion plasmas. 2015.

- [109] R Bravenec, J Citrin, J Candy, P Mantica, and T Görler and. Benchmarking the GENE and GYRO codes through the relative roles of electromagnetic and $E \times B$ stabilization in JET high-performance discharges. *Plasma Physics and Controlled Fusion*, 58(12):125018, nov 2016. doi: 10.1088/0741-3335/58/12/125018. URL <https://doi.org/10.1088%2F0741-3335%2F58%2F12%2F125018>.
- [110] A. White. *What will ITER do?*, 2015.
- [111] R Dux, R Neu, A G Peeters, G Pereverzev, A Mck, F Ryter, J Stober, and ASDEX Upgrade Team. Influence of the heating profile on impurity transport in ASDEX upgrade. *Plasma Physics and Controlled Fusion*, 45(9):1815–1825, aug 2003. doi: 10.1088/0741-3335/45/9/317. URL <https://doi.org/10.1088%2F0741-3335%2F45%2F9%2F317>.
- [112] F J Casson, C Angioni, E A Belli, R Bilato, P Mantica, T Odstreil, T Pütterich, M Valisa, L Garzotti, C Giroud, J Hobirk, C F Maggi, J Mlynar, and M L Reinke. Theoretical description of heavy impurity transport and its application to the modelling of tungsten in JET and ASDEX upgrade. *Plasma Physics and Controlled Fusion*, 57(1):014031, nov 2014. doi: 10.1088/0741-3335/57/1/014031.
- [113] Loarte et al 2016. Evaluation of tungsten transport and concentration control in iter scenarios *26th iaea fusion energy conf. (kyoto, japan, 17–22 october 2016) ppc/2-1*.
- [114] F Köchl, A Loarte, E de la Luna, V Parail, G Corrigan, D Harting, I Nunes, C Reux, F G Rimini, A Polevoi, and M Romanelli and. W transport and accumulation control in the termination phase of JET h-mode discharges and implications for ITER. *Plasma Physics and Controlled Fusion*, 60(7):074008, jun 2018. doi: 10.1088/1361-6587/aabf52. URL <https://doi.org/10.1088%2F1361-6587%2Faabf52>.
- [115] N Kumar, Y Camenen, C Bourdelle, S Benkadda, A Loarte, AR Polevoi, and JET Contributors. Linear stability of the inner core of jet plasmas using gyrokinetic simulations. *46th eps conference on plasma physics, (eps 2019), milan, italy*.
- [116] Jiaqi Dong, L Chen, and F Zonca. Study of kinetic shear alfvén modes driven by ion temperature gradient in tokamak plasmas. *Nuclear Fusion*, 39(8):1041–1050, aug 1999. doi: 10.1088/0029-5515/39/8/308.
- [117] W. Chen, R. R. Ma, Y. Y. Li, Z. B. Shi, H. R. Du, M. Jiang, L. M. Yu, B. S. Yuan, Y. G. Li, Z. C. Yang, P. W. Shi, X. T. Ding, J. Q. Dong, Z. X. Wang, Yi. Liu, M. Xu, Y. H. Xu, Q. W. Yang, and X. R. Duan. Alfvénic ion temperature gradient activities in a weak magnetic shear plasma. *EPL (Europhysics Letters)*, 116(4):45003, nov 2016. doi: 10.1209/0295-5075/116/45003. URL <https://doi.org/10.1209%2F0295-5075%2F116%2F45003>.

- [118] S. Moradi, I. Pusztai, W. Guttenfelder, T. Fülöp, and A. Mollén. Microtearing modes in spherical and conventional tokamaks. *Nuclear Fusion*, 53(6):063025, may 2013. doi: 10.1088/0029-5515/53/6/063025. URL <https://doi.org/10.1088%2F0029-5515%2F53%2F6%2F063025>.
- [119] Yanqiang Hu, Yemin Hu, Nong Xiang, Yanqing Huang, and Zhen Zheng. The effects of toroidal equilibrium flow on the stabilization of ballooning modes in tokamaks. *AIP Advances*, 10(7):075009, 2020. doi: 10.1063/5.0005647. URL <https://doi.org/10.1063/5.0005647>.
- [120] D. Estève, Y. Sarazin, X. Garbet, V. Grandgirard, S. Breton, P. Donnel, Y. Asahi, C. Bourdelle, G. Dif-Pradalier, C. Ehrlacher, C. Emeriau, Ph. Ghendrih, C. Gillot, G. Latu, and C. Passeron. Self-consistent gyrokinetic modeling of neoclassical and turbulent impurity transport. *Nuclear Fusion*, 58(3):036013, jan 2018. doi: 10.1088/1741-4326/aa6ebb. URL <https://doi.org/10.1088%2F1741-4326%2Faa6ebb>.
- [121] Breton Sara. *Tungsten transport in a tokamak : a first-principle based integrated modeling approach*. PhD thesis, Aix-Marseille University, 2017.
- [122] Shigeo Hamada. Notes on Megneto-Hydrodynamic Equilibrium. *Progress of Theoretical Physics*, 22(1):145–146, 07 1959. ISSN 0033-068X. doi: 10.1143/PTP.22.145. URL <https://doi.org/10.1143/PTP.22.145>.
- [123] M. J. Pueschel and F. Jenko. Transport properties of finite- β microturbulence. *Physics of Plasmas*, 17(6):062307, 2010. doi: 10.1063/1.3435280. URL <https://doi.org/10.1063/1.3435280>.
- [124] Tihiro Ohkawa. A transport model for alcator scaling in tokamaks. *Physics Letters A*, 67(1):35 – 38, 1978. ISSN 0375-9601. doi: [https://doi.org/10.1016/0375-9601\(78\)90560-1](https://doi.org/10.1016/0375-9601(78)90560-1). URL <http://www.sciencedirect.com/science/article/pii/0375960178905601>.
- [125] C Angioni and P Helander. Neoclassical transport of heavy impurities with poloidally asymmetric density distribution in tokamaks. *Plasma Physics and Controlled Fusion*, 56(12):124001, nov 2014. doi: 10.1088/0741-3335/56/12/124001. URL <https://doi.org/10.1088%2F0741-3335%2F56%2F12%2F124001>.
- [126] K.W. Wenzel and D.J. Sigmar. Neoclassical analysis of impurity transport following transition to improved particle confinement. *Nuclear Fusion*, 30(6): 1117–1127, jun 1990. doi: 10.1088/0029-5515/30/6/013. URL <https://doi.org/10.1088%2F0029-5515%2F30%2F6%2F013>.
- [127] E A Belli and J Candy. Full linearized fokker–planck collisions in neoclassical transport simulations. *Plasma Physics and Controlled Fusion*, 54(1):015015, dec 2011. doi: 10.1088/0741-3335/54/1/015015. URL <https://doi.org/10.1088%2F0741-3335%2F54%2F1%2F015015>.

- [128] E A Belli, J Candy, and C Angioni. Pfirsch–schlüter neoclassical heavy impurity transport in a rotating plasma. *Plasma Physics and Controlled Fusion*, 56(12):124002, nov 2014. doi: 10.1088/0741-3335/56/12/124002. URL <https://doi.org/10.1088%2F0741-3335%2F56%2F12%2F124002>.
- [129] ITER Physics Basis Editors, ITER Physics Expert Group Chairs and Co-Chairs, ITER Joint Central Team, and Physics Unit. Chapter 1: Overview and summary. *Nuclear Fusion*, 39(12):2137–2174, dec 1999. doi: 10.1088/0029-5515/39/12/301. URL <https://doi.org/10.1088%2F0029-5515%2F39%2F12%2F301>.
- [130] K. Ikeda. Progress in the ITER physics basis. *Nuclear Fusion*, 47(6), jun 2007. doi: 10.1088/0029-5515/47/6/e01. URL <https://doi.org/10.1088%2F0029-5515%2F47%2F6%2Fe01>.
- [131] A. Loarte, M. L. Reinke, A. R. Polevoi, M. Hosokawa, M. Chilenski, N. Howard, A. Hubbard, J. W. Hughes, J. E. Rice, J. Walk, F. Köchl, T. Pütterich, R. Dux, and V. E. Zhogolev. Tungsten impurity transport experiments in alcator c-mod to address high priority research and development for iter. *Physics of Plasmas*, 22(5):056117, 2015. doi: 10.1063/1.4921253. URL <https://aip.scitation.org/doi/abs/10.1063/1.4921253>.
- [132] F.J. Casson, R.M. McDermott, C. Angioni, Y. Camenen, R. Dux, E. Fable, R. Fischer, B. Geiger, P. Manas, L. Menchero, and G. Tardini and. Validation of gyrokinetic modelling of light impurity transport including rotation in ASDEX upgrade. *Nuclear Fusion*, 53(6):063026, may 2013. doi: 10.1088/0029-5515/53/6/063026. URL <https://doi.org/10.1088%2F0029-5515%2F53%2F6%2F063026>.
- [133] C. Angioni, R.M. McDermott, E. Fable, R. Fischer, T. Pütterich, F. Ryter, and G. Tardini and. Gyrokinetic modelling of electron and boron density profiles of h-mode plasmas in ASDEX upgrade. *Nuclear Fusion*, 51(2):023006, feb 2011. doi: 10.1088/0029-5515/51/2/023006. URL <https://doi.org/10.1088%2F0029-5515%2F51%2F2%2F023006>.